Post-Synthesis Growth of Lanthanide-doped Nanoparticles by Surface Modification

Gaurav Srivastava

A Thesis

in

The Department

of

Chemistry and Biochemistry

Presented in Partial Fulfillment of the Requirements

for the Degree of Master of Science (Chemistry) at

Concordia University

Montréal, Québec, Canada

December 2021

© Gaurav Srivastava, 2021

CONCORDIA UNIVERSITY

School of Graduate Studies

This is to certify that the thesis prepared

By: Gaurav Srivastava

Entitled: Post-synthesis Growth of Lanthanide-doped Nanoparticles by Surface Modification

And submitted in partial fulfilment of the requirements for the degree of

Master of Science (Chemistry)

Complies with the regulations of the University and meets the accepted standards with respect to originality and quality.

Signed by the final examining committee:

Dr. Marek Majewski_____ Chair

Dr. Christine DeWolf_____ Examiner

Dr. Rafik Naccache_____ Examiner

Dr. John A. Capobianco_____ Supervisor

Approved by

_____

Dr. Yves Gelinas, Graduate Program Director

_____

Dr. Pascale Sicotte, Dean of Arts and Science

Date: 13th December, 2021

ABSTRACT

Post-Synthesis Growth of Lanthanide-doped Nanoparticles by Surface Modification

Gaurav Srivastava

The growth mechanisms occurring during the synthesis of nanoparticles has been previously investigated by varying reaction conditions, such as reaction time, temperature, ligand and pH. The growth mechanisms of nanoparticles are reported only for high-temperature synthesis methods, by mechanisms such as Ostwald ripening and oriented attachment. Ostwald ripening involves the dissolution of small nanoparticles into monomers, with successive growth by ripening of the surface of bigger particles with these monomers. Oriented attachment occurs by the alignment of more particles following a preferential crystal orientation, and their successive attachment at the interface between particles by so-called *necking*. Among the previous studies, the mechanisms behind the growth of lanthanide-doped nanoparticles have been often reported, considering the interesting properties of these nanomaterials. Despite the thorough investigations reported in the literature, investigations into the potential for post-synthesis growth mechanisms in lanthanide-doped nanoparticles at room temperature has never been explored.

The presented research project aims to verify the possibility for tailoring the size and shape of lanthanide-doped nanoparticles at room temperature after their initial bottom-up synthesis at high temperature, in response to the present lack of knowledge in this field. The study of post-synthesis surface modification and growth at room temperature has to be carried out taking into consideration the same parameters that are usually varied in the reported investigations for synthesis at high temperatures, such as reaction time, ligand, pH, and temperature. For this project,

the temperature is fixed at room temperature, and all the other parameters were varied. Oleate-capped nanoparticles were obtained by a co-precipitation reaction method. The potential for post-synthesis growth of two nanoparticle compositions were investigated ($NaREF_4$ with RE = Y and Gd) to unveil the mechanism of the occurring surface phenomena. As a general protocol, the synthesized particles were subjected to ligand exchange from the as-synthesized oleate capping ligand to phosphonate ligands by first protonating the oleate ion by acidic treatment, followed by deprotonation of the phosphonate ligand and substitution on the nanoparticle surface in basic conditions. The pH was controlled by using two different bases (NaOH and KOH), and the occurrence of the ligand exchange was assessed by FT-IR spectroscopy. Modifications of nanoparticle size and shape during the post-synthesis growth were assessed by collecting aliquots at established time intervals and characterizing them *via* transmission electron microscopy and inductively coupled plasma mass spectrometry.

The results demonstrated that the ligand can facilitate changes in morphology and growth at room temperature in presence of different bases. $NaREY_4$ nanoparticles do not show significant growth, but a necking behaviour was observed when NaOH was used as a base in the presence of the ligand, in which the nanoparticles orient themselves and connect within each other by forming "necks" between particles (growth by oriented attachment). On the other hand, $NaREF_4$ nanoparticles showed a significant change in size distribution when KOH was used as a base in the presence of the ligand, by forming smaller particles compared to their initial size, which then condense onto the surface of bigger nanoparticles, proving that growth occurs by Ostwald ripening. These results show that it is quite possible to induce room-temperature growth of lanthanide-doped nanoparticles post synthesis by varying the cation of the base. The use of the ligand is crucial for

preventing aggregation and inducing the coalescence of smaller nanoparticles into larger ones. To our knowledge, these observations in post-synthesis growth have been reported for the first time.

ACKNOWLEDGEMENTS

Throughout the journey of my masters degree at Concordia University, I have received a great amount of love and support from everyone, for which I consider myself lucky.

First and foremost, I would like to thank my supervisor, Dr. John A. Capobianco, for providing me with the opportunity of working in the Lanthanide Research Group, and providing me with all the support and guidance in this new city.

I would like to thank Professor Christine DeWolf and Professor Rafik Naccache for all the great insights, support. The discussions during the committee meeting were crucial, and have given me a clear vision of what needed to be done.

I want to extend my heartful appreciation towards my colleagues (inside and outside the lab), especially Gabi Mandl, Gabriella Tessitore, and Cynthia Messina; I would have not completed my degree without the support of these three wonderful women. There were times when I was about to quit, but the support and love that I got from people around me kept me going. I would also like to acknowledge Keegan Mckibbon for answering my stupid organic questions, and pulling all-nighters with me in the lab. Also, thank you for directing me towards good music in the lab.

I would also like to thank Jennifer Sachs for helping me with the administrative grind, because of her I was able to graduate on time.

Above all, I would like to impart great gratitude to my parents, my family members, Akhil and Alicia for having faith in me and always supporting me through the thicks and thins of my life. Life has been a roller coaster for me in the past few years, and thought me quite valuable lessons. I consider myself lucky to have witnessed and experienced these phases of my life with the people I love.

Table of Contents

List of Figures

List of Schemes

List of Tables

List of Abbreviations

Argon	Ar
ESA	Excited state absorption
ESI	Electrospray ionization
ETU	Energy transfer upconversion
FT-IR	Fourier transform Infrared
GC-MS	Gas chromatography mass spectrometry
ICPMS	Inductively coupled plasma mass spectrometry
Ln	Lanthanide
LC-MS	Liquid chromatography mass spectrometry
NIR	Near Infrared
NMR	Nuclear magnetic resonance
OA^-	Oleate ion
OAH	Oleic aid
RE	Rare earth
TEM	Transmission electron microscopy
TMSBr	Trimethylbromosilane
UCNPs	Upconverting nanoparticles
UV	Ultraviolet
PXRD	X-ray powder diffraction

Chapter 1– Introduction

1.1 From bulk to “nanoscale”

The idea of nanotechnology was first discussed by Richard P. Feynman during a speech, entitled “There's plenty of room at the bottom”, at the annual meeting of the American Physical Society in 1959 at the California Institute of Technology.[1] Feynman was a visionary who addressed, for the first time, the possibility of manipulating the properties of bulk material by controlling the arrangement of atoms and molecules on a smaller scale.[1] In 1974, the term “nanotechnology” was first used in a publication by the Japanese scientist Norio Taniguchi.[2] The possibilities offered by this novel field have led to the development and invention of instruments that can facilitate the visualization of materials at an atomic level, such as the scanning tunnelling microscope, invented in 1981, followed by the development of the atomic force microscope.[2] These advancements ignited sparks in the scientific community and paved the way for scientists to dig deeper into the possibility to manipulate and visualizing individual atoms and molecules. The heightened interest led to countless contributions from the scientific community on the theme of nanotechnology. Among them, “Engines of Creation: The Coming Era of Nanotechnology” by K. Eric Drexler published in 1986 was particularly interesting with respect to the evidenced significance of developing devices at the nano-scale. In his book, Drexler discusses the possibilities that could be achieved by nanotechnology in the future by addressing topics like AI (Artificial Intelligence), nanorobotics, aerospace development, nanomedicines and many more.[3] Following the contributions of these pioneering scientists, several others followed the path to the development of nanotechnology and, more in general, nanoscience.

The prefix “nano” is derived from a Greek word meaning “dwarf” and it consequently signifies something extremely small.[4] According to the International Organisation for Standardisation, the

term nanoscale refers to size ranging from approximately 1 to 100 nm.[5] As a comparison, the width of a single human hair strand is approximately 60,000 nm, and the length of a folded DNA strand is around 2 nm.[6] The example of DNA can further be of help in understanding the differences between bulk material and nanoparticles. DNA is composed of billions of nucleotides, which together form the whole DNA strand, whose length is about 2 nm.[6] Similarly, nanoparticles can be visualized by separating a bulk material into its constituent small building blocks, as shown in Fig 1.1. This difference in the size of bulk materials and nanoparticles results in significant changes in the properties of the material. As the particle size decreases and enters the nano regime, the surface area-to-volume ratio increases (Fig 1.1).[6,7] As a consequence, the majority of the atoms reside at the surface of a nanoparticle, making it more reactive compared to its bulk counterpart. The presence of the so-called "dangling bonds" at the nanoparticle surface gives rise to the enhanced reactivity of these nanomaterials.[6,7] Further investigations are unravelling more and more differences between bulk and nanomaterials, proving once more what Feynman and the other pioneers in the field of nanotechnology theorized and supporting the necessity for further studies to expand our knowledge.

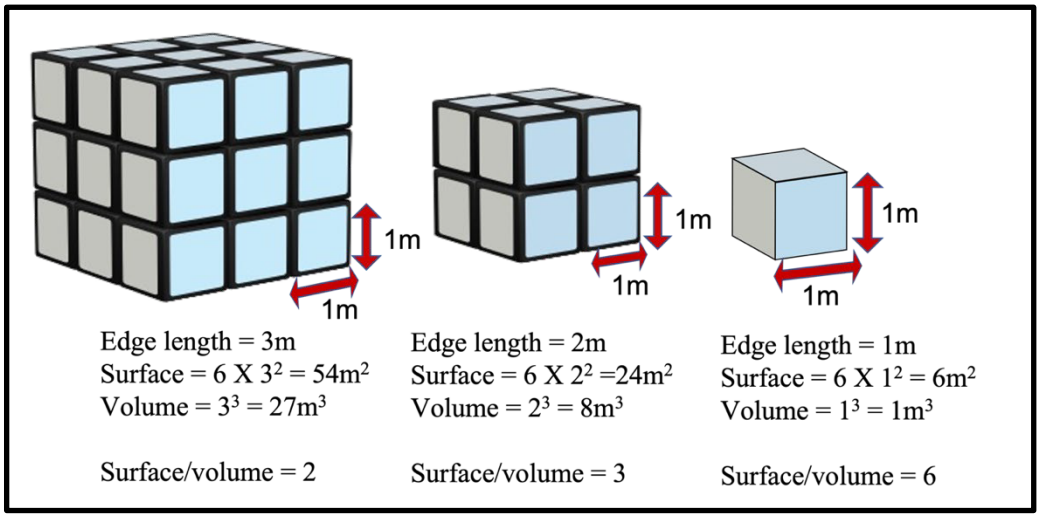

Figure 1.1. The increase in surface area-to-volume ratio as a result of reduction in particle size. Here the surface-to-volume ratio was calculated using individual cubes to form larger cubes.

1.2 Nanofabrication

Nanoparticles can be synthesized by two main approaches: the *top-down* approach and the *bottom-up* approach.[8] Both strategies have their advantages and are used accordingly depending on the application. The top-down approach implies that the nanoparticles are synthesized by breaking up larger particles by the use of physical processes like lithographic imprinting and nanomechanical machining (such as crushing, milling, or grinding).[9] Considering that the formed nanoparticles originate from the bulk material, characterized by a more homogeneous and ordered structure, a top-down approach results in structures characterized by a long-range order, for example, bulk-/film-machining of silicon wafer on which the channels are created by etching the trenches.[10] In contrast, the bottom-up approaches rely on the self-assembly phenomenon at the molecular level due to physical and chemical interactions. which assemble primary building blocks, such as molecules or ions, into nanoscopic structures, enabling researchers to obtain structures with short-range order, for example, the formation of quantum dots and carbon nanotubes.[8,10]

Examples of the top-down approach are widely present in industrial manufacturing, which require the production of synthetic nanomaterials. Amongst them, the semiconductor industries developed silicon wafers by using lithography-based procedures.[11] Despite its success in industrial manufacturing, this approach has its shortcomings, as the obtained nanomaterials are affected by the introduction of defects.[10,12] Other top-down techniques to produce nanoparticles include selective dealloying, laser ablation synthesis, arc discharge synthesis and several others.[13,14,15]

The bottom-up approaches are directly inspired by biological reactions occurring in nature. The human body itself consists of many nanostructures that are essential for its proper functioning. As an example, glucose, DNA, and hemoglobin are all in the size range between 1 to 10 nm, and the self-assembly of these molecules constitutes the basis for many biological processes.[6] These naturally-occurring self-assembling and self-organising biological components have pushed the scientific community to try mimicking the same behaviour by bottom-up synthetic methods. The bottom-up approaches also rely on the same idea of self-assembly and self-organisation of primary building blocks (such as atoms or molecules) through non-covalent interactions (i.e. Van der Waals, electrostatic, hydrogen bonding, $\pi - \pi$ interaction, hydrophilic, and hydrophobic interactions) to produce dynamic and functional structures.[8] Their self-assembly can produce two dimensional and three dimensional structures with uniform shape and size. These interactions have enabled the production of self-assembled two dimensional ultra-thin films such as self-assembled monolayers and Langmuir Blodgett films, and three dimensional assemblies such as metallic, polymeric, hybrid nanoparticles, nanorods, and carbon nanotubes.[16,17] Many of the reported nanomaterials are synthesized in solution, by taking advantage of the interactions between solvents, ligands and reactants to assemble the final nanoparticle with different sizes and morphologies depending on the reaction parameters. Among these approaches, the thermal decomposition and co-precipitation syntheses reported for the lanthanide-doped nanoparticles object of this study will be further described in detail in the next sections.

1.3 Lanthanide-doped Upconverting Nanoparticles

1.3.1 The lanthanides

The lanthanide series contains 15 elements, with atomic numbers ranging from 57 (lanthanum, La) to 71 (lutetium, Lu). The lanthanides can be further divided into two groups: the light rare earth elements containing elements from lanthanum to europium (Z from 57 to 63) and the heavy rare earth elements containing elements from gadolinium to lutetium (Z from 64 to 71).[18] The lanthanides (Ln) occur in nature in three different types of mineral sources: Monazite (contains mainly the lighter lanthanides), Xenotime (predominately contains heavier lanthanides), and Bastnaesite (contains even distribution of the lanthanides).[18] In 1787, the first lanthanide-containing mineral was found in a small Swedish village called Ytterby by Carl Axel Arrhenius and was named Ytterite.[19] After seven years, in 1794, Johann Gadolin successfully extracted an oxide "earth" from the mineral Ytterite, which was later named Gadolinite.[19] Subsequently, within 100 years, the detection of Gadolinite marked the discovery and isolation of all the other lanthanides such as lanthanum, neodymium and yttrium.[19]

The general electronic configuration of the lanthanides series extends from [Xe] $5d^1 6s^2$ for lanthanum to [Xe] $4f^{14} 5d^1 6s^2$ for lutetium. The most stable and common oxidation state in which the lanthanide ions exist is +3. However, some of the lanthanides may exist in the +2 and +4 states.[18] This arises from the fact that the 4f orbital requires a large amount of energy for the ionization to occur as compared to the 5d and 6s orbitals. The 4f electrons are closest and therefore held strongly by the nucleus and with successive ionization, the 4f electrons exert a greater pull by the nucleus than 5d and 6s electrons.[20] The shielding effect of the 5d and 6s electrons on the 4f electrons are of great importance for the optical properties of the lanthanides, as the 4f electrons do not experience major effects from different environments. [20]

All the lanthanide ions except for La^{3+} and Lu^{3+} are luminescent, and their emissions span the entire electromagnetic spectrum from ultraviolet (UV) to visible and near infrared (NIR).[21] The f-f transitions show sharper emission bands owing to the fact that 4f electrons are well shielded, and are unaffected by the external forces, i.e. the crystal field of the other coordinating ions or molecules.[18] This results in a very minimal change in the internuclear distance in the excited state, which in turn produces narrow emission bands (very small Stokes shifts), independently of the host material.[21] In contrast, this situation is different for organic molecules, the excitation frequently leads to the strongly coupled vibration of bonds, and hence larger Stokes' shifts, producing broad emissions.[21]

1.3.2 Upconverting mechanism

Lanthanide-doped nanoparticles are a class of inorganic nanoparticles exhibiting unique optical properties. Some lanthanide-doped nanoparticles can exhibit upconversion luminescence, which is an anti-Stokes luminescence phenomenon of absorption of longer wavelength radiation, for instance, infrared or NIR light, to produce shorter wavelength radiation, usually in the UV-visible range. It is a multiphoton process that involves the sequential absorption of photons rather than a simultaneous absorption.[7] The upconversion is achieved when a lanthanide ion undergoes sequential absorption of photons, leading to excitation from the ground state to the higher emitting states. The excited ions can then continue to populate higher energy states, or non-radiatively transfer the energy to neighbouring ions in the same excited state, promoting the population of the higher energy states, which decays back to the ground state *via* emission of wavelengths in the UV-visible, or NIR regions.[7] Lanthanide-doped nanoparticles exhibit versatile optical properties

which can be modulated depending upon the concentration, type of lanthanide ions and the type of host materials that form the nanocrystal.

The upconversion process can be explained by extensively studied mechanisms, and occurs through four mechanisms: Ground/excited state absorption (GSA/ESA), energy transfer upconversion (ETU), cooperative upconversion and photon avalanche upconversion.[22] These mechanisms require the described sequential absorption of two or more photons from a metastable excited state to higher energy states, which results in the increasing population of the excited states from which upconversion emission occurs. Here we will discuss the two most efficient upconversion mechanisms; i.e. excited state absorption (ESA), energy transfer upconversion (ETU).

1.3.2.1 Ground state and excited state absorption (GSA/ESA)

Ground state/excited state absorption involves a single lanthanide ion (ion X) which consecutively absorbs the incoming photons from the excitation source. A typical excited state absorption process is depicted in figure 1.2, where the ion X absorbs one photon resonant with the energy gap between the ground and the excited state to promote an electron from a low lying ground state (G)

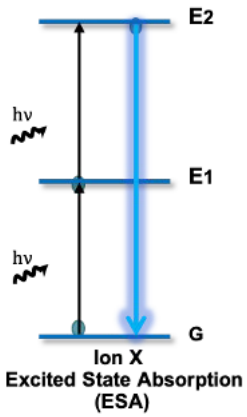

Figure 1.2. General mechanism for Ground/Excited state absorption upconversion.

to an intermediate excited state (E1). The long decay time of the intermediate metastable excited state (E1) facilitates the absorption of a second incoming photon and promotes the electron from the intermediate excited state (E1) to the higher excited state (E2). As a result, upconversion can be observed by sequential absorption to the higher excited state (E2) followed by radiative decay to the ground state (G). In order to observe ESA, the lanthanide ion should have a ladder-like energy level structure, along with an energy of the incident photon resonant with the energy gap between its energy levels. Only a few lanthanide ions, such as Er^{3+}, Tm^{3+}, Ho^{3+}, and Nd^{3+} are characterized by the energy state structure necessary to allow this process.[23]

1.3.2.2 Energy Transfer Upconversion (ETU)

Energy transfer upconversion, earlier known as *l'addition de photons par transferts d'energie* (APTE), was first mentioned by François Auzel in 1966.[22] Auzel proposed the possibility to achieve the sensitization of the upconversion luminescence by energy transfer between two different ions, the activator and the sensitizer ions. A sensitizer ion is defined as an ion that upon excitation will absorb energy, while an activator will accept the energy emitted by the sensitizer ion.[7] Until then, all the energy transfer mechanisms were believed to be taking place from the excited state of the sensitizer ions to the ground state of the activator ion.[22] In the same year, Ovsyankin and Feofilov were able to elucidate the IR to blue upconversion in Yb^{3+}/Tm^{3+} co-doped systems, as an energy transfer upconversion to Tm^{3+} (initially in its ground state) by two Yb^{3+} ions (present in the excited state).[24]

Energy transfer upconversion occurs in a system that has separate centres for absorption and emission. This process relies on the mutual interaction between two neighbouring ions, where one acts as a donor of energy (sensitizer) and the other act as an acceptor of energy (activator).[22] The energy transfer upconversion process is explained in figure 1.3 with two different rare earth ions, ion X and ion Y,

activator and sensitizer ion respectively. The first step involved in this process is the excitation of a sensitizer ion from its ground state (G) to its intermediate excited state (E0) by the incoming pump photon which corresponds to the energy gap between the G and E1 states. This is followed by a non-radiative energy transfer from the excited state of the sensitizer ion to the activator ion, which results in the promotion of the acceptor ion from the ground state (G) to its metastable excited state (E_1). Afterwards, another non-radiative energy transfer takes place from the second sensitizer ion, which leads to the promotion of the activator ion to the E2 state. From this excited

state, the ion decays back radiatively to its ground state (G), while the sensitizer ion relaxes back to its ground states due to the energy transfer. To have efficient upconversion, the chosen sensitizer should

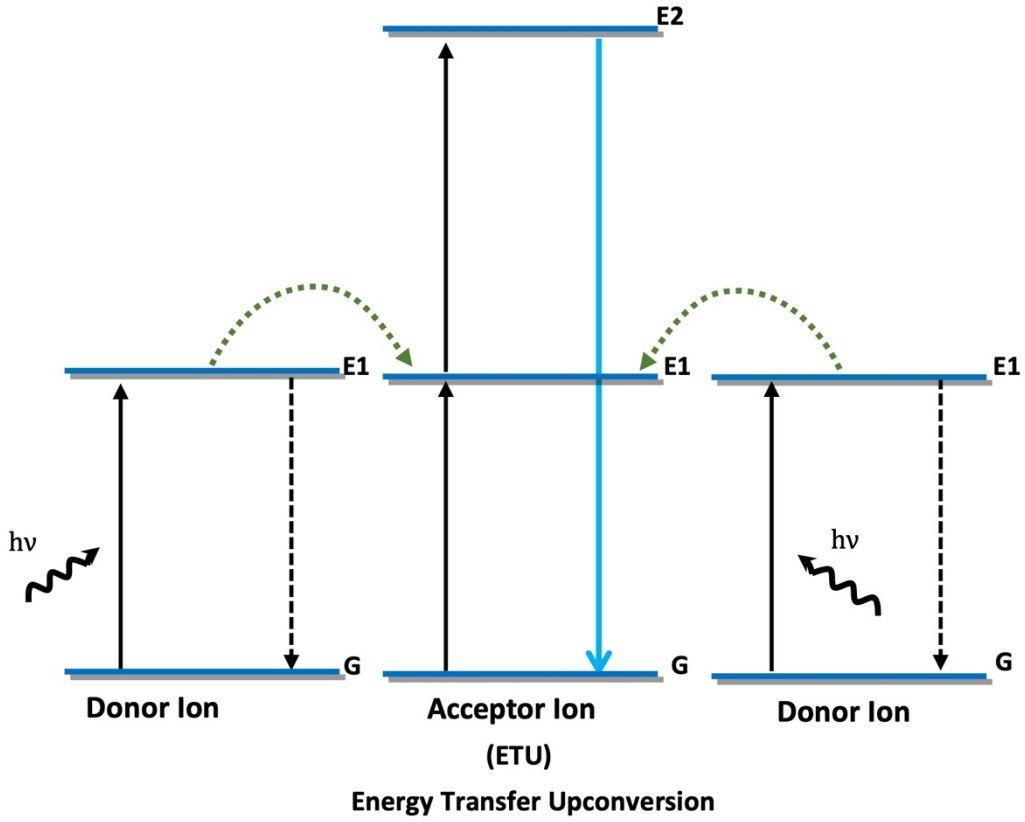

Figure 1.3. General mechanism for Energy transfer upconversion.

have a relatively high absorption cross-section of the incoming excitation wavelength, and with energy states matching with those of the activator ion. Also, the activator ion should have an intermediate

excited state with a longer lifetime, to promote the electron to the second excited state before it radiatively relaxes back to its ground state. Among all the lanthanides, Yb^{3+} is considered as an ideal sensitizer for ETU because of its large absorption cross section (9.11×10^{-21} cm^{-2} for $^2F_{7/2} \rightarrow {}^2F_{5/2}$ transition with a maximum at 976 nm).[25]

This process is dependent upon the dopant ion concentration, as this will vary the distance between the neighbouring ions (the sensitizer concentration typically varies from 10-50 times that of activator ion)[7], and the choice of lanthanides ions incorporated. The ETU mechanism is much more efficient compared to GSA/ESA mechanism, due to the large absorption cross section of Yb^{3+}.[22]

1.3.3 The $NaREF_4$ crystal phases

$NaYF_4$ and $NaGdF_4$ are the most efficient hosts among the upconverting fluoride host nanoparticles. $NaYF_4$ was introduced by Menyuk *et al*. in 1972.[26,27] The $NaYF_4$ and $NaGdF_4$ hosts are known to crystallise in one of two phases: cubic or hexagonal, with the hexagonal phase being more thermodynamically stable.[28] In cubic sodium rare earth (RE) fluoride systems, ($NaREF_4$) there is only one type of high-symmetry cation site available, which is randomly occupied by Na^+ and RE^{3+} ions. Contrarily, the crystal structure of hexagonal phase $NaREF_4$ consists of an ordered array of F^- ions with two comparatively low-symmetry sites occupied by Na^+ and RE^{3+} ions. The transformation from cubic to the hexagonal phase of the lanthanide doped nanoparticles can be achieved by careful administration of reaction parameters such as the precursor ratios, capping ligand, reaction temperature and reaction time.

The cubic and hexagonal phase $NaREF_4$ nanoparticles exhibit different luminescent properties. Hexagonal phase nanoparticles provide at least an order-of-magnitude enhancement of

upconversion efficiency when compared to their cubic phase equivalent.[29] Cubic $NaREF_4$ nanoparticles doped with Er^{3+} exhibit a more intense red emission upon excitation with NIR light, whereas the hexagonal phase exhibits a more intense green emission. The reason for the improved luminescence in the hexagonal host can be attributed to the difference in the site symmetry of the lanthanide ions in the crystal lattice, the different coordination of the lanthanide ions and micro-disordered structure, which could lead to relaxation in the selection rules and broadening of the excitation and absorption spectra, resulting in improved ETU.

1.4 Nucleation, growth, and post-synthesis stability of nanoparticles

Out of various techniques, the chemical synthesis of nanoparticles in the solution phase is the most thoroughly studied, because of its underlying benefits such as straightforward protocol, easy manipulation, and narrow size distribution. In general, the process of nanoparticle growth involves two stages: nucleation and growth. Nucleation refers to the growth of the crystalline nuclei (seeds) which act as a template for crystal growth. The shape and morphology of the nanoparticles is highly dependent on the nucleation stage and is very well described by the LaMer curve.[30]

1.4.1 Growth of nanoparticles during synthesis

A well-controlled synthesis of nanoparticles is imperative to achieve uniform nanoparticles, which is crucial for understanding their properties. The growth of metal nanocrystals is predominantly achieved by adopting atom-mediated nucleation and growth, in which the atoms are considered to be the building blocks of the nucleation and growth processes.

1.4.1.1 LaMer Curve Nucleation and Growth

The growth mechanism of nanocrystals was elucidated by LaMer and Dinegar[31]. The nucleation and growth process of metal nanocrystals is described by the LaMer curve (figure 1.4) which is divided into three phases. In the first phase, there is the generation of metallic ions produced by reduction of metal salts, or by thermal decomposition of organometallic compounds. This causes a rapid increase in the monomer concentration (metallic atoms) which in turn leads to a concentration maximum, known as the *critical limiting supersaturation*. It is crucial to design the synthesis in such a way that the critical limiting supersaturation point is reached, otherwise monodispersed nanoparticles will not be formed.[30,32] In the second phase, a burst of nucleation occurs because of the supersaturation achieved in the solution, leading to the formation of small, stable clusters (nuclei). Finally, there is a gradual decrease in the monomer concentration (nuclei) owing to the increase in the consumption of monomers for the growth of generated clusters, which,

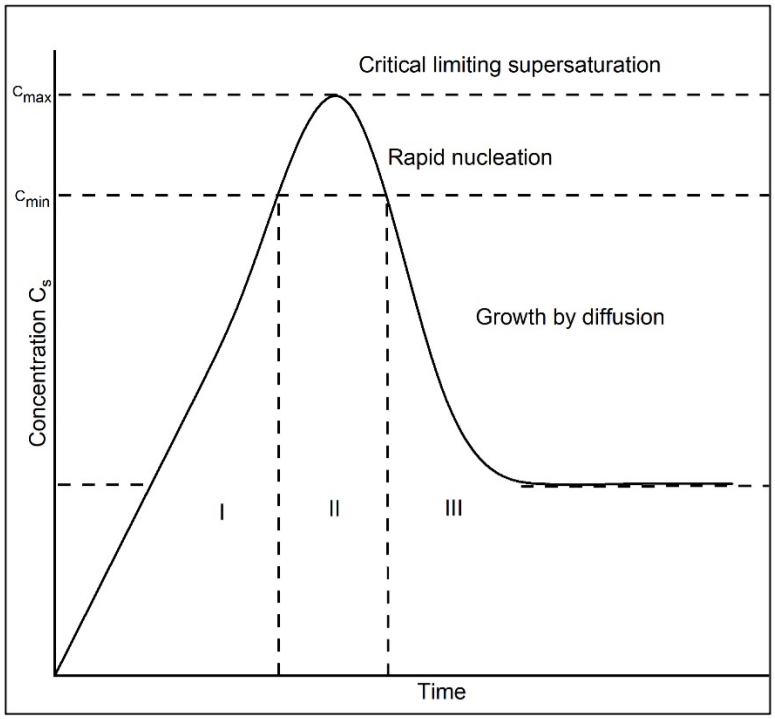

Figure 1.4. The LaMer curve representing three stages of growth process for nanocrystal growth. (image adapted from [30]).

after reaching a certain critical size, gets interlocked into a distinct shape (seed). These seeds grow into final nanocrystals by consuming metal atoms until the concentration decreases.[33]

1.4.1.2. Ostwald ripening and Oriented attachment

Ostwald ripening

Ostwald ripening was first described in 1896 by Wilhelm Ostwald.[34] It refers to the dissolution of smaller nanoparticles into the solution and reprecipitation to form larger nanoparticles (figure 1.5). The driving force for this process is the stability difference between larger and smaller nanoparticles.[35] In small nanoparticles, the majority of atoms/ions are present on the surface of the nanoparticles and possess higher surface energy making it less thermodynamically stable, which triggers the dissolution of smaller nanoparticles into the solution, and reprecipitation onto the larger nanoparticles.[30] Consequently, the nanoparticles continue to grow larger.

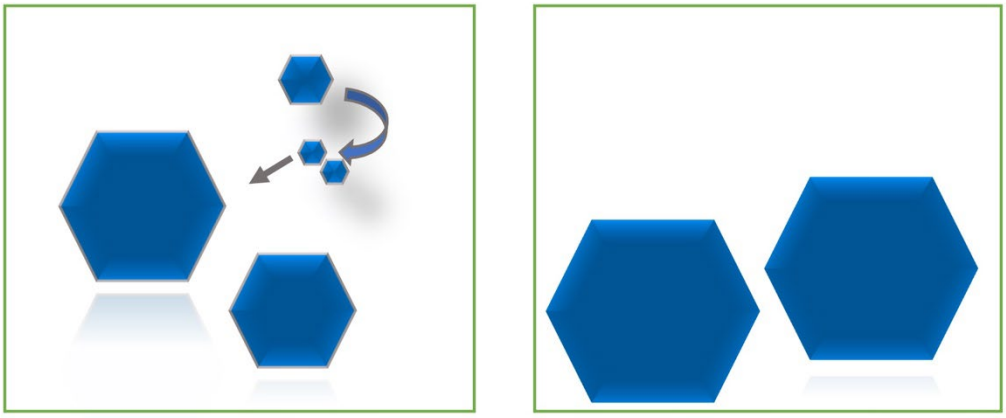

Figure 1.5. Schematic illustration of Ostwald ripening for the growth process of nanoparticles.

Oriented attachment

The LaMer model successfully explains the atom-mediated growth process, however; it is not applicable for particle-mediated growth.[33] Particle-mediated growth includes processes like oriented attachment, which refers to the growth of nanoparticles where the nanoparticles physically rotate to minimise the misalignment of their lattices when touching, which leads to the formation of a grain-grain interface.[33] This further leads to coalescence *via* the elimination of common grain boundaries (figure 1.6). This whole process reduces the enthalpy of the system in a thermodynamically favorable process.[33,36]

The driving force for obtaining oriented attachment in inorganic nanoparticles is the well-defined crystal structure and shape of the nanoparticles which can be synthesized by the hot-injection methods in organic media leading to the formation of particles that have facets with specific surface energy.[36] As a result, the binding energy and the amount of ligand per unit volume on the individual crystal planes will differ substantially, and if the surface of the nanoparticle planes is not sufficiently stabilized, then the particles can undergo oriented attachment in order to minimize energy, since the particles already exhibit aligned crystallographic plane, crystal fusion will be a favored process.[33]

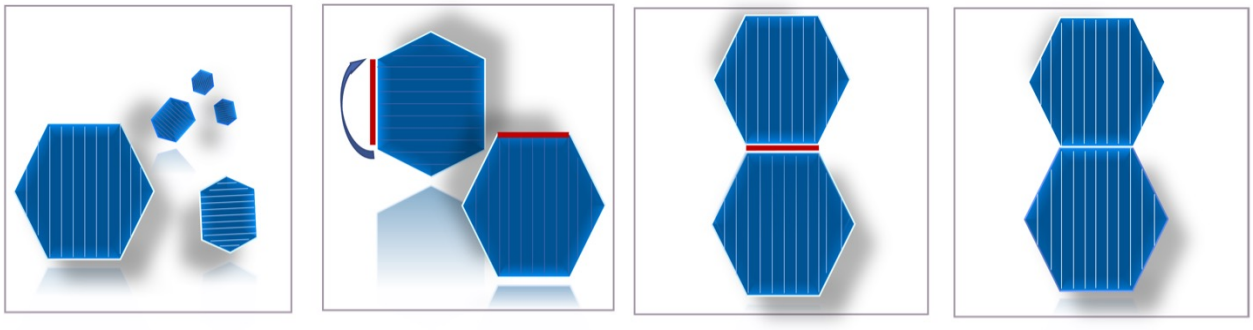

Figure 1.6. Schematic representation of Oriented attachment. Nanoparticles undergoes rotation, followed by alignment of crystallographic planes, and finally coalescence of nanoparticles.

1.4.1.3 Effect of ligand on the controlled growth of the UCNP during synthesis

A systematic study on the controlled growth of lanthanide doped upconverting nanoparticles was carried out in 2015 by Liu *et al*.[37] The study was based upon the epitaxial growth of core-shell architectures in the presence of oleic acid. During the synthesis of UCNPs, oleic acid is observed as oleate anions (OA^-) and in its molecular form as oleic acid itself (OAH), both of which influence the direction of growth along different crystallographic planes of the nanoparticles. In their investigation, they highlight the importance of the ratio of OA^-/OAH and studied the influence of those ratios as a change of interaction of the ligand with the crystallographic faces of the UCNPs, which leads to the morphological changes of the nanoparticles. Liu *et al.* also used DFT calculations to fully justify their work by quantifying the surface coordination between the (001) and (100) planes of the hexagonal phase $NaYF_4$ with the OA^- and OAH. The outcome of these calculations concluded that the OA^- prefers to bind to RE^{3+} ions present on the (100) planes with higher binding energy (-35.4 eV) compared to the RE^{3+} ions exposed on the (001) planes with lower binding energy (-21.8 eV). On the other hand, OAH molecules bind with higher energy to the (001) facets (-9.4 eV) than (100) facets (-4.6 eV). The difference in the binding affinity of OA^- and OAH arises from the atomic arrangements of the two planes. These findings have led to strategies for modulating the morphology of the nanoparticles during the synthesis by varying the ligand ratios and have shown that how crucial the effect of the ligand is on the morphology of the particles (figure 1.7).

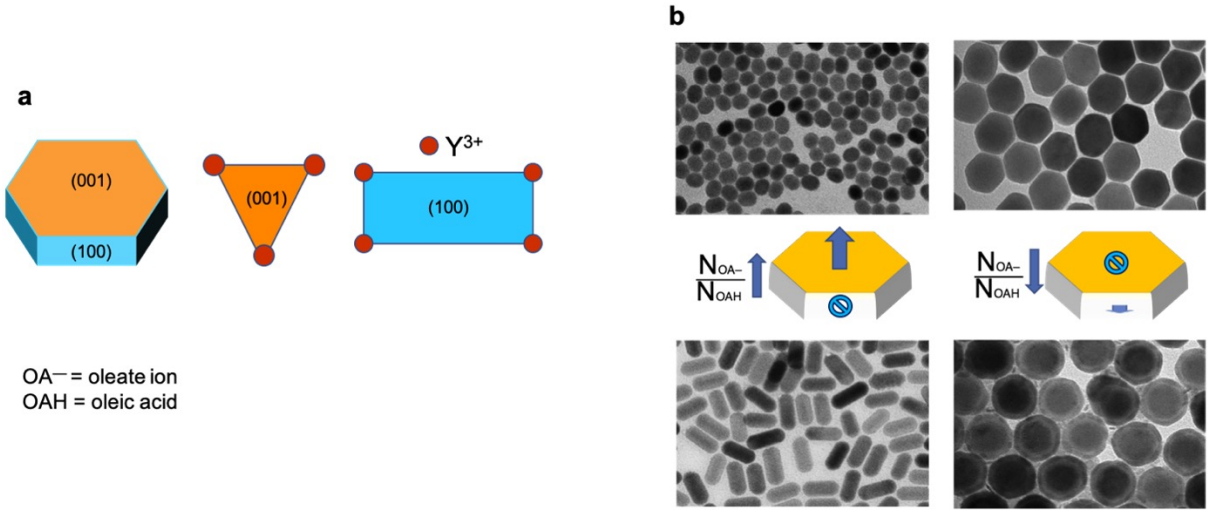

Figure 1.7. (a) Schematic representation of hexagonal phase $NaYF_4$ nanoparticles, and the constituting facets. (b) The effect of OA-/OAH ratio on the epitaxial growth of UCNPs during synthesis.

1.4.2 Surface chemistry behind the stability of lanthanide doped nanoparticles

As a material size shrinks down in size from bulk to the nano-scale, the surface area-to-volume ratio increases sharply. The decrease in size results in a substantial amount of atoms residing on the surface of the nanoparticles. The vast majority of atoms on the surface of the nanoparticles have dangling bonds which give rise to a high local energy produced due to the under-coordination of atoms present on the surface.[38]

The surface of the lanthanide doped nanoparticles are covered with OA^- (the most commonly used capping ligand for the synthesis of Ln-UCNP) engrained electrostatically to the positively charged surface of the Ln-UCNP. The electrostatic interactions between the oleate capping ligand and nanoparticle surface occur due to the positively charged surface arising due to the presence of Ln^{3+} ions and the negatively charged carboxylate head group from the oleate ion.[39]

The potential to engineer the surface properties of nanocrystals is an important aspect to modulate the physical and chemical properties for different applications. Based upon the application the nanoparticles are used for, the nanoparticles can be dispersed either in organic or aqueous media by using hydrophobic or hydrophilic capping ligands.[40] In the literature, there are several examples of removing the oleate capping ligand using acid treatment. Our group pioneered the method for the removal of oleate ions from the surface of the nanoparticles with an acidic pH 2 solution of HCl to protonate the oleate ions and disturb the electrostatic interaction with the nanoparticle surface.[39] Another efficient way to facilitate removal of the oleate ions using acid-base chemistry was reported by Dong *et al*.[40] where nitrosonium tetrafluoroborate ($NOBF_4$) was used to replace the hydrophobic organic ligand with the BF_4^- anions, providing electrostatic stabilization of the nanoparticles in polar media.[40] After the removal of the ligand, the surface can be functionalized using ligands or polymers, preferably containing negatively charged groups that can bind to the surface of the nanoparticles *via* electrostatic interactions. These interactions between the nanoparticles surface and ligand have been used in the past for modulating nanoparticles growth and stability.[41]

1.4.2.1 Effect of ligand on the colloidal stability of upconverting nanoparticles

Experiments on the colloidal stability of the upconverting nanoparticles with different ligands were performed in 2018 by Duong *et al*.[42] Their work provided a foundational interpretation on the stability of the nanoparticles with ligands containing three widely utilized head groups for surface modifications, namely phosphates, carboxylates and sulphonates. UCNPs grafted with polymers containing each of these functional groups were monitored at different pH values for

a week using dynamic light scattering. It was determined that UCNPs coated with phosphate-containing ligands exhibited increased stability compared to the UCNPs coated with the carboxylate and sulphonate-containing ligands. The investigation for determining the colloidal stability of nanoparticles with different head groups were performed by first synthesizing the amphiphilic di-block copolymers ($POEGA_{20}$-*b*-$PMAEP_5$, $POEGA_{20}$-*b*-PAA_5, $POEGA_{20}$-*b*-$PAMPS_5$). The poly(oligoethylene glycol) methyl ether acrylate (POEGA) provides the hydrophilicity, and the shorter hydrophobic block contains phosphate, carboxylate and sulphonate functional groups (PMAEP, PAA, and PAMPS, respectively). Density functional theory (DFT) calculations were performed by the same research group to investigate the adsorption energies of these groups with the $NaYF_4$ nanoparticle surface. The result showed the same trend as was seen with the dynamic light scattering studies (figure 1.8) with the phosphate group having the lowest adsorption energy (-90.4 Kcal mol^{-1}) followed by carboxylate (-77.9 Kcal mol^{-1}) and sulphonate (-80 Kcal mol^{-1}). These findings pointed out that the phosphonate type ligands have a higher affinity towards the surface of UCNP and are excellent for the long term stability of nanoparticles in various media. The binding affinity of the ligand towards the surface of the nanoparticles plays a crucial role in the stabilization of nanoparticles,[42] along with modulating the growth in a precise manner.[37]

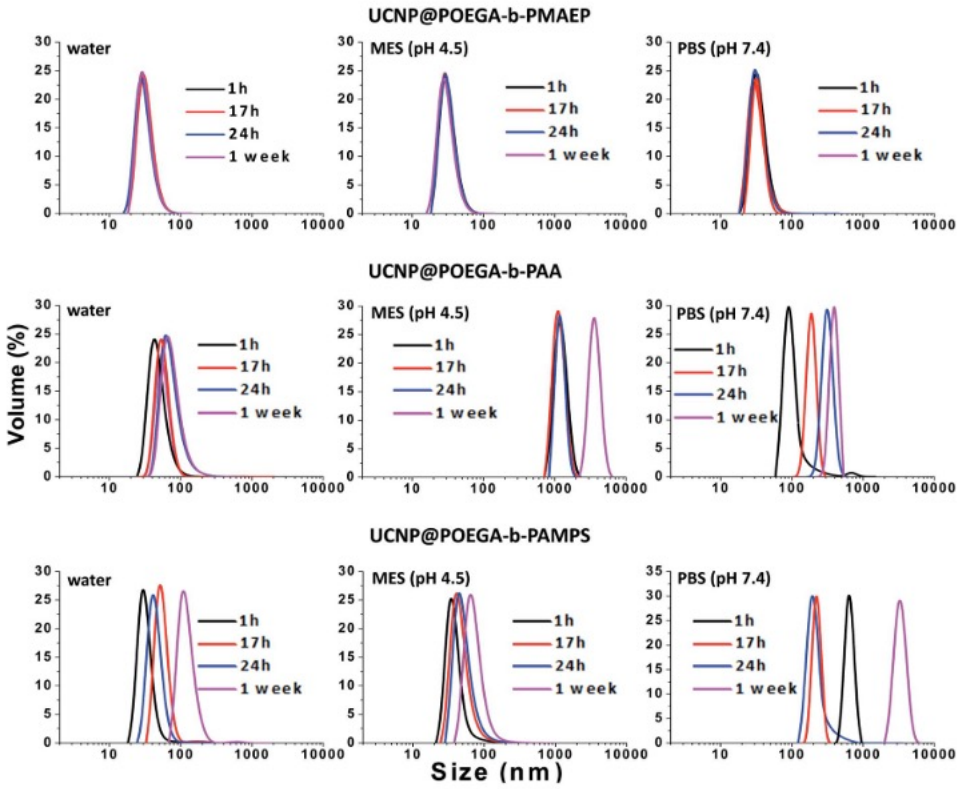

Figure 1.8. Shows the colloidal stability of UCNPs coated with phosphate, carboxylate and sulphonate head groups amphiphilic di-block copolymers over one week of storage in different media determined by dynamic light scattering measurements.

1.4.2.2 Disintegration of upconverting nanoparticles in aqueous media

Nanoparticles oftentimes display high dissolution rates compared to their bulk counterparts, because the solubility rate is highly dependent on the surface area-to-volume ratio, the surface coarseness and the curvature.[43,44] Smaller, spherical particles have a smaller radius of curvature, resulting in greater thermodynamic instability and a higher dissolution rate. For instance, the binary Ln-fluorides (LnF_3) have a higher dissolution rate when compared to their bulk counterparts.[45] The solubility of the nanoparticles is also seen to be dependent on the pH, and the nature of ligands which can form complexes with Ln^{3+} or F^-.[46]

In their seminal paper of 2015, Lisjak *et al*. discussed the partial dissolution of Ln-based lanthanide doped upconverting nanoparticles consisting of binary (LnF_3, Ln = La, Gd) and ternary fluoride matrices ($MLnF_4$, M = Na; Ln = Y) synthesized *via* hydrothermal, solvothermal or thermal decomposition methods and having different crystal phases.[47] Their work has demonstrated that for ternary Ln-based fluoride nanoparticles, the solubility rate is dependent on the thermodynamic stability of their crystal lattice. In the case of $NaYF_4$ nanoparticles, the hexagonal phase is more thermodynamically stable as compared to the metastable cubic phase, which makes the cubic phase more chemically unstable and prone to dissolution. Another contributing factor for the dissolution of the lanthanide doped nanoparticles was determined to be the result of the formation of soluble complexes between the capping ligands and the lanthanides. Many inorganic and organic anions such as CO_3^{2-} and citrate are known to form stable complexes with lanthanide ions, which further increase the dissolution rate of the nanoparticles.[46] The disintegration of the nanoparticles will further affect the crystal lattice, and a decrease in the size of the nanoparticles will be seen, due to which the surface-to-volume ratio will increase, creating an increased number of quenching centers because of the surface defects, and hence a decrease in the upconversion emission is observed.[48]

1.4.2.3 Effect of size/surface quenching on the luminescence intensity of UCNP

The luminescence intensity of upconverting nanoparticles is highly dependent on the size of the nanoparticles, any size change will have a direct effect on the emission intensity.[49] In a major advance in 2010, Wang *et al*. performed a comparative spectroscopic study on lanthanide doped nanoparticles with varying sizes, in order to understand the surface-quenching effects on the luminescence.[49] In their analysis, they compared the emission intensity of $NaGdF_4$:Yb^{3+}/Tm^{3+} with three different sizes of 10, 15 and 25 nm, excited at 980 nm. They concluded that the small lanthanide doped nanoparticles were more susceptible to having weaker emission intensities

because of the surface-quenching effects, which arise from enhancement in the local concentration of crystal defects that dissipate the excitation energy in the form of energy transfer to surface defects, impurities, ligands, and solvents.[49]

Water molecules are known to significantly affect the emission intensity of lanthanide doped nanoparticles because of their high stretching vibration (3500 cm^{-1}) energy which quenches the luminescence *via* surface oscillations/vibrations. More recent evidence in 2021 by Feng *et al.* showed the internal quenching of upconversion occurs due to the presence of OH^- in the crystal lattice, introduced during synthesis.[50] They reported that replacement of fluoride ions by hydroxyl ions in $NaYF_4:Yb^{3+}/Er^{3+}$ occurs because of their similar electronic structure, charge and chemical nature. The de-excitation rate of Yb^{3+} excited state was found to be two times faster in the presence of OH^- defects. The presence of OH^- either on the surface or in the crystal lattice has been proven to have a detrimental effect on the upconversion emission intensity.[50]

1.4.2.4 Nanoparticles attachment without ligand detachment

As discussed above, the role of ligands is not only limited to providing stability, or controlling growth and regulating solubility in the desired media. Organic ligands can also facilitate coalescence between nanoparticles.[51] Recent developments in the studies of growth behaviour of thiol coated gold nanoparticles under ambient conditions at room temperature, both experimentally and computationally, have led to new findings, *i.e.*, the nanoparticles could exhibit coalescence even in the presence of ligands.[52,53] Coalescence refers to the fusion of nanoparticles, where the nanoparticles merge to form bigger nanoparticles.[54] Computational studies on the coalescence of gold nanoparticles without ligand detachment were conducted in 2020 by a group of researchers from China.[55] They deduced a new mechanism for the coalescence of thiol coated gold

nanoparticles under ambient conditions in water. They have shown that the hydrophobic interaction between the chains of ligands favors aggregation, and the presence of exposed surface atoms leads to attachment *via* coalescence and undergoes atomic rearrangement (figure 1.9). These findings are important because they provided evidence of particles undergoing coalescence without ligand detachment.

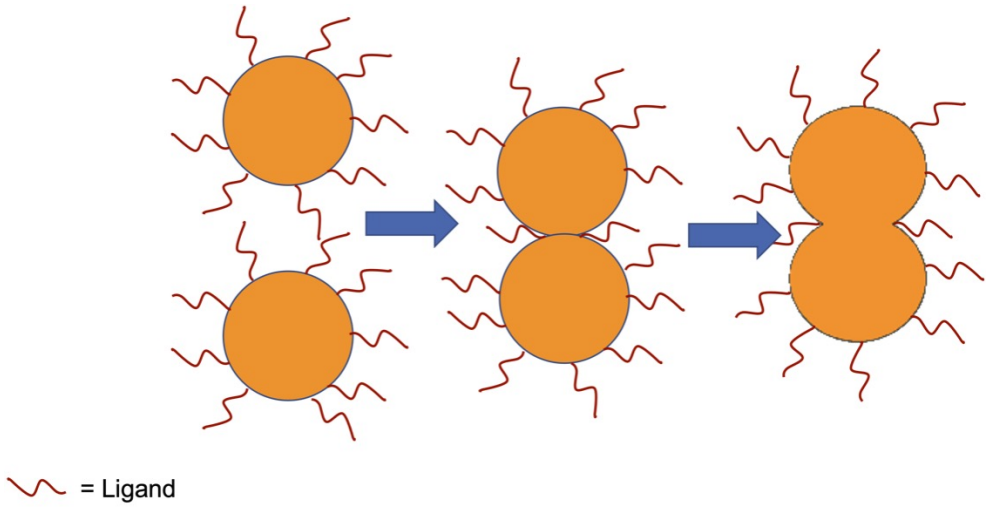

Figure 1.9. Schematic for coalescence of gold nanoparticles by atomic rearrangement at room temperature without ligand detachment in water.

Chapter 2 - Experimental and characterization techniques

2.1 Synthesis procedure of lanthanide doped nanoparticles

2.1.1 Coprecipitation synthesis method

The co-precipitation method is one of the facile ways of producing lanthanide doped nanoparticles due to a gradual growth period and provides a more ecological environment from an industrial perspective by eliminating the production of toxic by-products.[56]

2.1.1.1 Procedure for the synthesis of oleate-capped nanoparticles ($NaYF_4$: Yb^{3+}/Er^{3+}) by coprecipitation

$NaYF_4$: Yb^{3+}/Er^{3+} nanoparticles were synthesized *via* the co-precipitation method, as a one-pot reaction. In the procedure, YCl_3 (0.2366 g, 0.78 mmol), $YbCl_3$ (0.0774 g, 0.2 mmol) and $ErCl_3$ (0.0076 g, 0.02 mmol) were added to a 3-neck round bottom flask, followed by the addition of oleic acid and 1-octadecene (6 mL and 15 mL respectively), the mixture was first degassed at room temperature for 10 minutes and then at 120 °C for 30 minutes to form a clear solution. After which, the reaction mixture was cooled down to 50 °C and the vacuum was released to introduce the sodium and fluoride sources *via* injection of a methanolic solution of NaOH (0.1 g, 2.5 mmol) and NH_4F (0.148 g, 4 mmol) at a rate of 1 mL/min. The reaction mixture was stirred at 50 °C for 30 minutes. The methanol was removed by heating the reaction at ~70 ºC in the presence of a high vacuum and the reaction temperature was further raised to 100 ºC and then to 120 ºC for 10 minutes. After the flask was purged with Argon (Ar) gas for 5 minutes and the vacuum adapter was quickly replaced with a gas outlet tubing acting as a bubbler to monitor a constant flow of Ar through the flask. The temperature was then increased to 310 ºC at a rate of 13.5 ± 2.5 ºC min^{-1}. The reaction was held for 120 minutes at 310 ºC with a constant flow of Argon before cooling it

to room temperature naturally. The as-synthesized, oleate capped nanoparticles were first washed with ethanol to precipitate them, and they were further isolated *via* centrifugation (3000 rpm, 15 minutes). The pellet was saved, and the supernatant was discarded. The pellet was washed by dispersing it in a 1:4 hexane/ethanol mixture twice to remove any impurities.

2.1.2 Thermal decomposition Synthesis method

The thermal decomposition synthesis consists of two steps where in the first step the lanthanide oxides are transformed into lanthanide trifluoroacetate precursors. This is followed by the decomposition of the lanthanide trifluoroacetate precursors and subsequent formation of the oleate-capped nanoparticles ($NaYF_4$: Yb^{3+}/Er^{3+} or $NaGdF_4$: Yb^{3+}/Er^{3+}).

2.1.2.1 Procedure for the synthesis of lanthanide trifluoroacetate precursors

The precursors for $NaYF_4$ co-doped with Yb^{3+} and Er^{3+} were prepared by taking Y_2O_3 (0.2201 g, 0.975 mmol), Yb_2O_3 (0.0985 g, 0.25 mmol) and Er_2O_3 (0.00956 g, 0.025 mmol), whereas the precursors for $NaGdF_4$ co-doped with Yb^{3+} and Er^{3+} were prepared by taking Gd_2O_3 (0.3534 g, 0.975 mmol), Yb_2O_3 (0.0985 g, 0.25 mmol) and Er_2O_3 (0.00956 g, 0.025 mmol) in a 3-neck round-bottom flask taken up by a mixture of trifluoracetic acid/water (10 mL, 1:1). The cloudy solution was refluxed at 80 °C under stirring conditions until it turns clear. After which the solution was dried at 60 °C to yield trifluoroacetate lanthanide precursors.

2.1.2.2 Procedure of synthesis of lanthanide doped $NaYF_4$: 20% Yb, 2%Er and $NaGdF_4$: 20% Yb, 2% Er upconverting nanoparticles

Both nanoparticle compositions are prepared in an identical manner as follows. 2.5 x 10^{-3} mol of CF_3COONa (0.3400 g) was added to the dried precursor solids (section 3.1.2.1) along with 7.5 mL of oleic acid and 7.5 mL of 1-octadecene (flask A). In another 3-neck round bottom flask 12.5 mL of oleic acid and 12.5 1-octadecene was added (flask B). Both the flasks were degassed at 150 °C for 30 min under a vacuum to remove any water. The solution in flask B was then heated to 310 °C at a rate of 13.5 ± 2.5 ºC min^{-1} under argon and maintained at this temperature. The rare-earth trifluoroacetate solution at 150 ºC in flask A was injected into the solution in flask B with a syringe at a rate of 1 mL/min using a pump injector (Harvard Apparatus Ecnoflow). The injection was completed in 15 min after which the flask was maintained at 310 °C for 120 min under an argon atmosphere. The system was left to cool to room temperature. The first precipitation of nanoparticles was done with absolute ethanol and were collected via centrifugation at 4000 rpm for 15 minutes. The collected nanoparticles were purified with multiple washes to remove any impurities with a 1:3 hexane/ethanol mixture.

2.2 Synthesis of Capping ligand AL238B

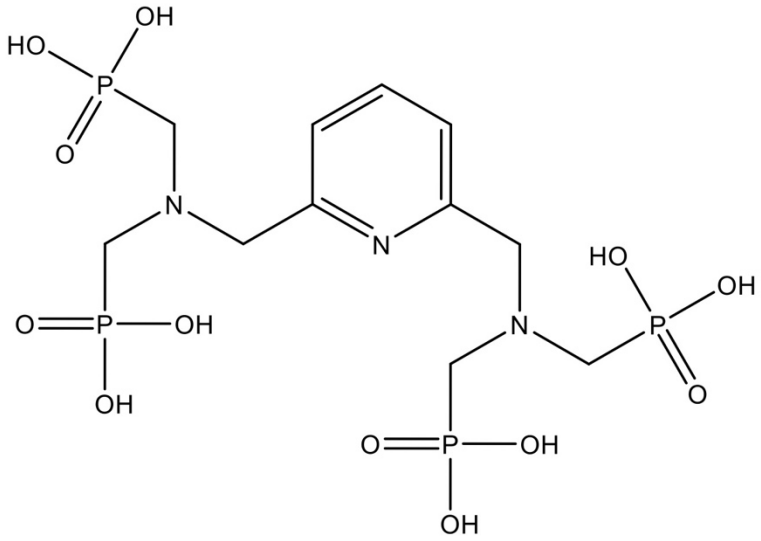

Figure 2.1. Structure of ligand **AL338B**.

2.2.1 Synthesis of precursors

The synthesis of ligand AL238B was attempted several times according to previous literature reports.[57,58] However, a novel synthetic route was designed and proved more efficient in attaining

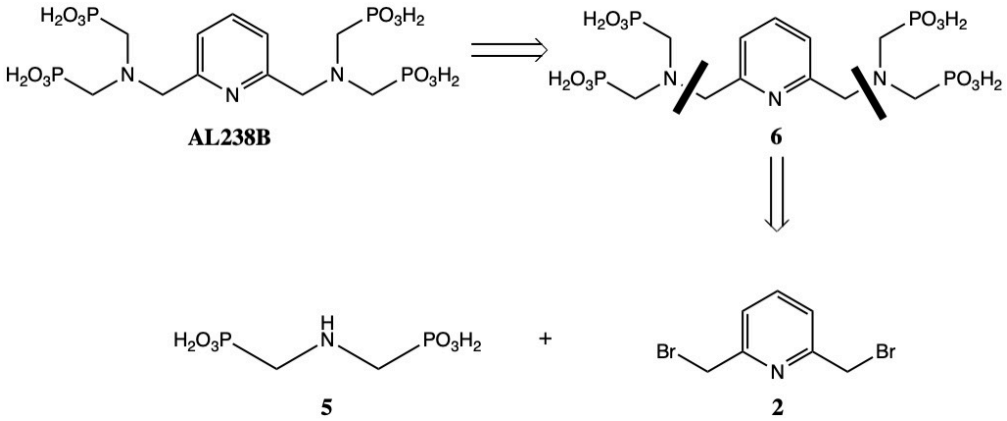

Scheme 2.1. Retrosynthetic analysis of ligand **AL238B**.

the compound, as summarized below (scheme 2.1). Ligand AL238B was synthesized from the necessary precursors 2,6-bis(bromomethyl) pyridine **2** and amine bisphosphonate **5** (figure 2.2).

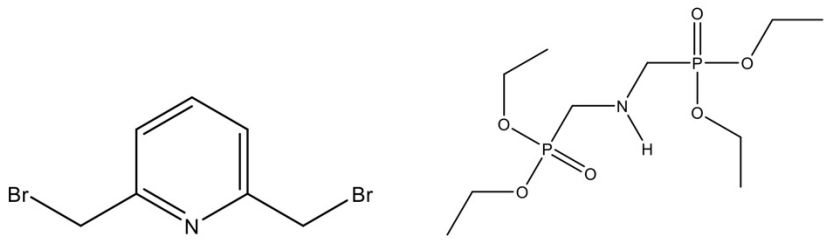

2 **5**

Figure 2.2. Structure of precursor **2 and 5**.

2.2.1.1 Synthesis of 2,6-dibromomethylpyridine

The first step for the synthesis of ligand AL238B requires the formation of the 2,6-dibromomethylpyridine **2**. The dibromomethylpyridine was obtained by suspending 2,6-pyridinedimethanol (2 g, 14.4 mmol) in DMF (25 mL) with dropwise addition of PBr_3 (3 mL, 31.9 mmol) at 0 °C. The mixture was stirred for 4 hours at room temperature, followed by the addition of water (15 mL). The aqueous layer was extracted with diethyl ether (3 × 50 mL), the organic layer was dried with Na_2SO_4 and. The solvent was removed under pressure. The crude product was purified by column chromatography (Ethyl acetate: hexanes 1:1) to give 1.66 g (43%) of 2,6-dibromomethylpyridine as a white solid (scheme 2.2).[59] **^{1}H NMR** (300 MHz, Chloroform-*d*) δ 7.70 (t, *J* = 7.7 Hz, 1H), 7.38 (s, 2H), 4.54 (s, 4H). **MS** (GC-MS) *m/z* calculated for $C_7H_7Br_2N$: 264.9; found 264.9 [M], 266.9 [M+2], and 268.9 [M+4].

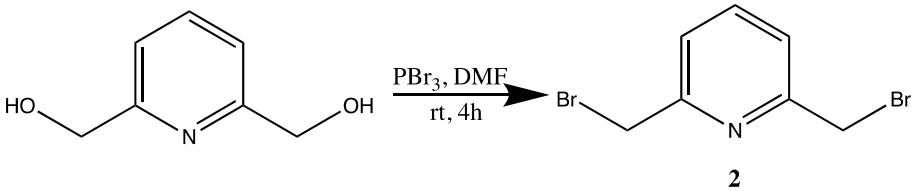

2

Scheme 2.2. Synthesis of 2,6 dibromomethylpyridine **2**.

2.2.1.2 Synthesis of tetraethyl iminobis(methylphosphonate)

The synthesis of amine bis(methylphosphonate) **5** is performed by using primary amines of benzylamine (0.98 g, 9.33 mmol) which undergoes a double Kababchnik-Fields reaction with three equivalents of 37 % formaldehyde and two equivalents of diethyl phosphite (2.57 g, 18.7 mmol).[60] The reaction was carried out in a Biotage Initiator under microwave irradiation at 100 °C for 1h. Water and formaldehyde were removed *in vacuo* to give crude tetraethyl N-benzyl amine bis(methylphosphonate) **4**. The crude was purified by column chromatography using a gradient of MeOH/DCM (0 % to 10 % increased by increments of 2 %, v/v) to afford **4** (2 g, 52 %). Benzylated amine 4 (0.4245 g, 1 mmol) was then taken up in a reaction flask with 0.050 g of 10 % Pd/C with 30 mL of ethanol, refluxed for 24 h with a constant bubbling of hydrogen gas in the reaction mixture to afford amine bis(methylphosphonate) **5** (quantitative yield) as an oil. (Scheme 2.3)

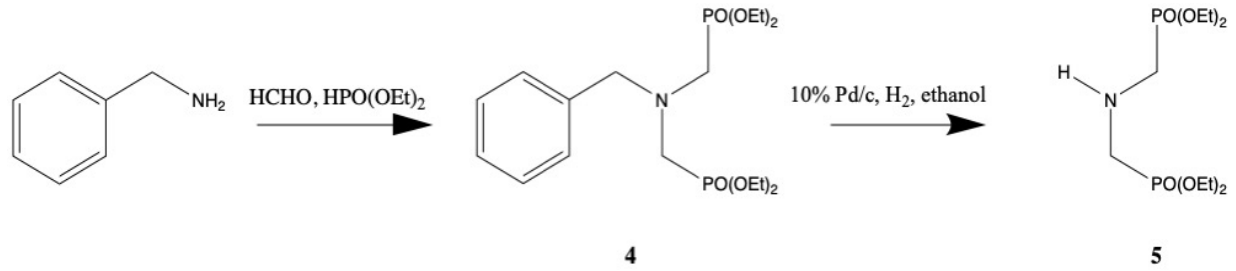

4 **5**

Scheme 2.3. Synthetic route for synthesis of tetraethyl iminobis(methylphosphonate) **5**.

^{1}HNMR (300 MHz, Chloroform-*d*) δ 4.23 – 4.08 (m, 8H), 3.16 – 3.07 (m, 4H), 1.34 (t, *J*= 7.1 Hz, 12H). **MS** (GC-MS) *m/z* calculated for $C_{10}H_{25}NO_6P_2$: 317.12; found 317.1 [M].

2.2.3 Synthesis of di-aminated pyridine

In a 50 mL reaction flask 2,6-dibromomethylpyridine **2** (2 mmol, 0.529 g) was mixed with tetraethyl amine bis(methyl phosphonate) **5** (4 mmol, 1.27 g) in the presence of K_2CO_3 (8 mmol, 1.105 g). The reaction flask was closed with a septum and was flushed with argon to provide an anhydrous environment. After which, 40 ml of anhydrous acetonitrile was added through injection into the flask. The suspension was heated at 60 °C for 14 h under argon. The solvent was evaporated *in vacuo*. The crude product was diluted with DCM (50 mL) and washed with 3% (aq., w/v) Na_2CO_3 (3 x 50 mL). The organic layer was dried over anhydrous Na_2SO_4, decanted and the solvent evaporated *in vacuo*. The crude material was purified by column chromatography using DCM to extract the unreacted 2,6-dibromomethylpyridine **2**, followed by EtOAc/methanol (9:1, v/v), and later on with $CHCl_3$/methanol (9:1, v/v) to afford 0.74 g (50%) of compound **6** as a yellow oil. (Scheme 2.4).

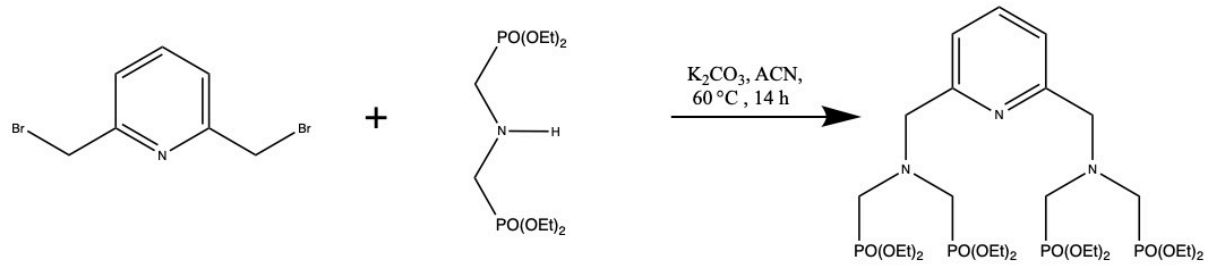

2 **5** **6**

Scheme 2.4. Synthesis of precursor **6**.

^{1}H NMR (300 MHz, Chloroform-*d*) δ 7.66 (t, *J* = 7.7 Hz, 1H), 7.48 (d, *J* = 7.7 Hz, 2H), 4.19 – 4.09 (q, 16H), 4.08 (s, 4H), 3.22 (d, *J* = 10.2 Hz, 8H), 1.31 (t, *J* = 7.1 Hz, 24H). ^{13}C NMR (126 MHz, Chloroform-*d*) δ 157.65, 137.07, 122.05, 61.97 (d, *J* = 7.2 Hz), 50.89 (d, *J* = 8.1 Hz), 49.62

(d, *J* = 8.2 Hz), 16.50 – 16.37 (m). **^{31}P NMR** (202 MHz, Chloroform-*d*) δ 24.37. ESI^{+}/MS (MeOH): m/z calculated for $C_{27}H_{55}N_3O_{12}P_4$: 737.27; found 738.3 ([M+1], 100%).

2.2.3 Synthesis of Ligand AL238B

To the solution of precursor **6** (1 mmol, 740 mg) in dichloromethane (DCM), trimethylbromosilane (TMSBr) (40 mmol) was added at room temperature. The solution was stirred at room temperature for 24 h. A subsequent addition of TMSBr (40 mmol) was made at room temperature for another 24 h. The solvent was removed *in vacuo* to give a yellow oil. The crude oil was taken up with methanol (12 mL) and stirred for 2 hours at room temperature. The process of evaporation and dissolution was repeated again with MeOH. After the addition of methanol, the reaction was left for stirring at room temperature for 24 h. The solvent was removed under vacuum to produce a brown oily residue which was taken up with a minimum amount of MeOH. In a beaker containing diethyl ether (50 mL) with continuous stirring, the methanolic solution of brown oily residue was added dropwise and centrifuged to collect white precipitate and dried under vacuum to afford ligand AL238B (50%). The centrifugation, dissolution and precipitation process was repeated until a clear white precipitate is obtained (scheme 2.5.) **^{1}H NMR** (500 MHz, Deuterium Oxide) δ 7.86 (t, *J* = 7.8 Hz, 1H), 7.39 (d, *J* = 7.8 Hz, 2H), 4.85 (s, 4H), 3.53 (d, *J* = 12.5 Hz, 8H). **^{13}C** NMR (126 MHz, Deuterium Oxide) δ 149.45, 139.83, 123.83, 59.19, 52.27 (d, *J* = 137.1 Hz). **^{31}P** NMR (202 MHz, Deuterium Oxide) δ 7.77. ESI^{+}/MS (MeOH): m/z calculated for $C_{11}H_{23}N_3O_{12}P_4$: 513.02; found 514.03 ([M+1], 100%)

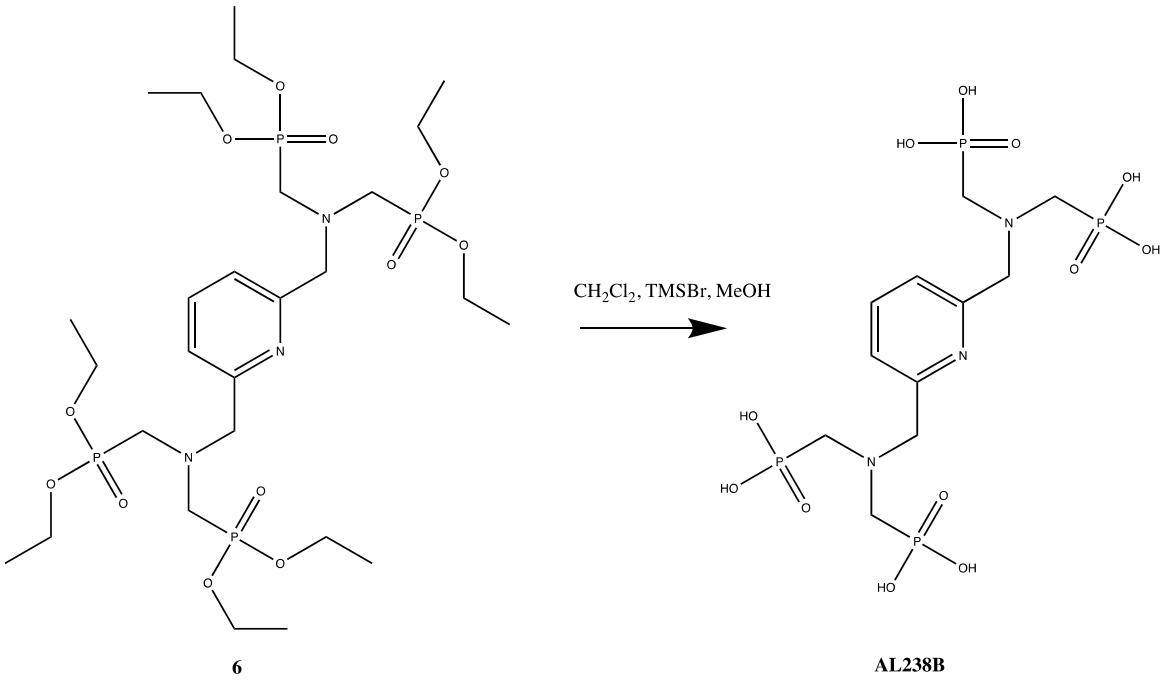

6 AL238B

Scheme 2.5. Synthesis of Ligand **AL238B**.

2.3 Surface modification *via* post-synthesis ligand exchange

The ligand exchange of upconverting nanoparticles capped with oleate ions was carried out by dispersing 50 mg of oleic acid-coated $NaYF_4$ Er^{3+}:Yb^{3+} synthesized by co-precipitation/thermal decomposition in 10 mL of an aqueous solution of EDTMP/AL238B (5 mg/mL) maintained at a pH of 2.5 while stirring for 24 hours. During the exchange, the carboxylate group of oleic acid was protonated in an acidic solution (pH 2.5 using HCl). After which hexanes was mixed with the aqueous solution to recuperate oleic acid. This process was repeated three times to completely remove the oleic acid. The organic solvent was discarded, and to the aqueous solution of nanoparticles 10 mg of ligand was further added and the pH was adjusted to 11 (by using different bases). The reaction was stirred for 3 days at room temperature. The nanoparticles were washed 3 times to remove the excess ligand. The nanoparticles were precipitated down and centrifuged for 20 minutes at 12000 rpm to obtain the final particles which were investigated for growth.

2.4 Characterization techniques

2.4.1 Transmission electron microscopy (TEM) and size distribution

Transmission electron microscopy was employed to determine the morphological, compositional and crystallographic information on the prepared nanoparticles. The sample was prepared by dispersing the nanoparticles in a 1 mg/mL solution of hexanes, which was further dropped (~ 10 µL) onto a 300-mesh formvar/carbon-coated copper grid (1.5mm in radius) followed by the evaporation of the solvent. The electron micrography was performed using a Jeol JEM-2100 F microscope operating at 120 kV.

2.4.2 X-ray Powder Diffraction (XRPD)

The XRD pattern of doped $NaYF_4$ nanoparticles were collected at room temperature using a Bruker D2 Phaser XRD System fitted with a LYNXEYE one-dimensional X-ray diffraction detector with a scan range was set from 20 - 90º 2θ with a step size of 0.5º and a count of 1 s. The sample was dried and measured on a quartz "zero background" disk.

2.4.3 Attenuated Total Reflection (ATR-FTIR)

The surface characterization of the synthesized $NaYF_4$**:** Yb^{3+}/Er^{3+} nanoparticles were performed using ATR-FTIR. The measurements were performed on a Nicolet iS5 FT-IR spectrometer containing a Thermo Scientific iD5 diamond ATR mount. The analysis was carried out on a powdered sample of the synthesized $NaYF_4$**:** Yb^{3+}/Er^{3+} nanoparticles.

2.4.4 Upconversion luminescence spectroscopy

The upconversion emission spectra of the oleate capped $NaREF_4$: Er^{3+}/Yb^{3+} (RE = Y^{3+}/Gd^{3+}) and the ligand capped $NaREF_4$: Er^{3+}/Yb^{3+} (RE = Y^{3+}/Gd^{3+}) were obtained upon excitation with a

handheld 976 nm laser (SKY-LASER). Nanoparticle emissions were collected through a 600 micron optical fiber from Ocean Optics directed into a Teledyne Princeton Instruments FERGIE-BRX UV-NIR spectrograph. The FERGIE spectrometer was equipped with a 50 micron slit and a 295 grooves/mm grating blazed at 575 nm.

2.4.5 Inductively coupled plasma mass spectrometry (ICP-MS)

ICP-MS measurements were performed to analyze the ion concentrations of the nanoparticles before and after surface modification. The samples were examined using an Agilent 7500ce inductively coupled plasma mass spectrometer at the Centre for Biological Applications of Mass Spectrometry (CBAMS) in Concordia University. A solution of Claritas PPT multi-element standards were diluted with 5 % HNO_3. The calibration curves were established using the standard solutions at concentrations of 0, 0.05, 0.1, 1, and 5 ppm.

2.4.6 $^{1}H/^{31}P/^{13}C$-NMR

The NMR spectra were recorded at room temperature in a 5 mm air-tight tube under N_2 atmosphere on a Varian VNMRS 500 MHz or Bruker Inova 300 MHz NMR spectrometer and referenced to internal tetramethylsilane.

2.4.7 Liquid Chromatography-Mass Spectroscopy (LC-MS)

The LC mass spectra for the ligand was acquired using a Thermo LTQ Orbitrap Velos mass spectrometer (MS) equipped with a heated electrospray ion source at the Centre for Biological Applications of Mass Spectrometry (CBAMS) at Concordia University. A full MS spectrum (*m/z* 150-2000) was acquired in the orbitrap at positive mode at a resolution of 100000.

Chapter 3 - Characterization of $NaYF_4$/ $NaGdF_4$:Yb^{3+} /Er^{3+}

The work proposed in this thesis focuses on understanding and uncovering the potential for growth of lanthanide doped upconverting nanoparticles after their initial synthesis by using phosphonate-type ligands. $NaYF_4$:Yb^{3+}/Er^{3+} and $NaGdF_4$:Yb^{3+}/Er^{3+} nanoparticles were synthesized through either thermal decomposition or co-precipitation techniques and used throughout to analyse the possibility of inducing growth at room temperature, and have been characterized in this section.

3.1 Hexagonal phase Na<u>Y</u>F_4:Yb^{3+}/Er^{3+}nanoparticles synthesized *via* coprecipitation

Oleate capped hexagonal phase $NaYF_4$:Yb^{3+}/Er^{3+} nanoparticles were synthesized *via* the coprecipitation technique (section 2.1.1). In the upcoming section, the oleate capped nanoparticles used in this particular study were characterized using various techniques as described below.

3.1.1 Morphology and size

The synthesis of $NaYF_4$: Yb^{3+}/Er^{3+} nanoparticles was done using the co-precipitation method. The oleate capped $NaYF_4$:Yb^{3+}/Er^{3+} hexagonal phase nanoparticles have a spherical morphology with an average size of 39 ± 5 nm (~500 particles were calculated to obtain the average size and size distribution). Figure 3.1 shows the TEM image and size distribution of the oleate capped hexagonal phase $NaYF_4$:Yb^{3+}/Er^{3+} nanoparticles used in further studies.

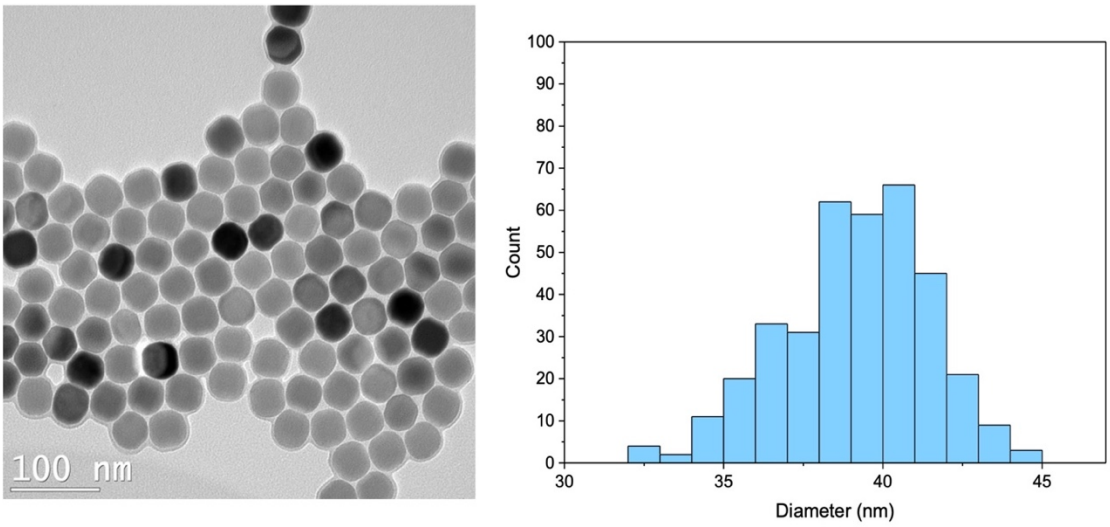

Figure 3. 1. Transmission electron micrograph (left) of oleate-capped $NaYF_4:Yb^{3+}/Er^{3+}$ hexagonal phase nanoparticles synthesized via coprecipitation. Histogram (right) of the particle size distribution (39 ± 5 nm) from the TEM images (based on approximately 500 nanoparticles measured).

3.1.2 Crystal phase

The crystal phase of the nanoparticles was determined by using powder X-ray diffraction (XRD). Figure 3.2 shows the powder XRD diffractogram of the oleate capped $NaYF_4:Yb^{3+}/Er^{3+}$ and the calculated standard JCPDS pattern. The peak positions correspond closely to the reported pattern of hexagonal phase $NaYF_4$ confirming the crystal phase of the synthesized nanoparticles (JCPDS no. 00-064-0156).

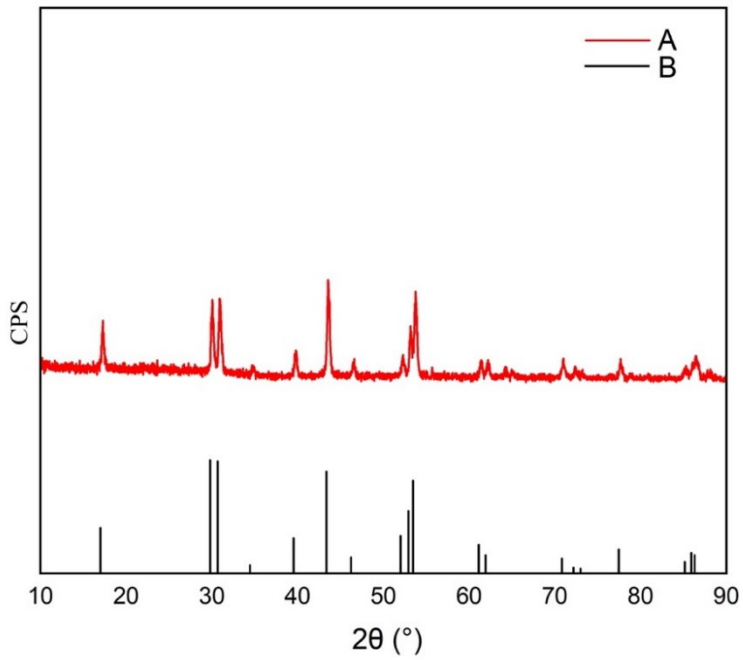

Figure 3. 2. Calculated standard (A) and experimental (B) XRPD Patters of $NaYF_4$ hexagonal phase (A) Reference pattern JCPDS File No. 00-064-0156, and (B) Oleate-capped hexagonal phase $NaYF_4$: Yb^{3+}/ Er^{3+} UCNPs.

3.1.3 Surface characterization

The surface characterization of the synthesized $NaYF_4$: Yb^{3+}/ Er^{3+}nanoparticles were performed using FTIR. Figure 3.3 shows the FTIR spectrum of the oleate capped $NaYF_4$:Er^{3+}/Yb^{3+} nanoparticles. The presence of oleate ions coordinated to the UCNP surface is confirmed by the peaks at 2923 cm^{-1} and 2852 cm^{-1} originating from the asymmetric and symmetric stretches of -CH_2 groups, and the asymmetric and symmetric stretching bands of the carboxylate at 1565 and 1469 cm^{-1} respectively. For comparison purposes, we have included the spectrum of oleic acid.

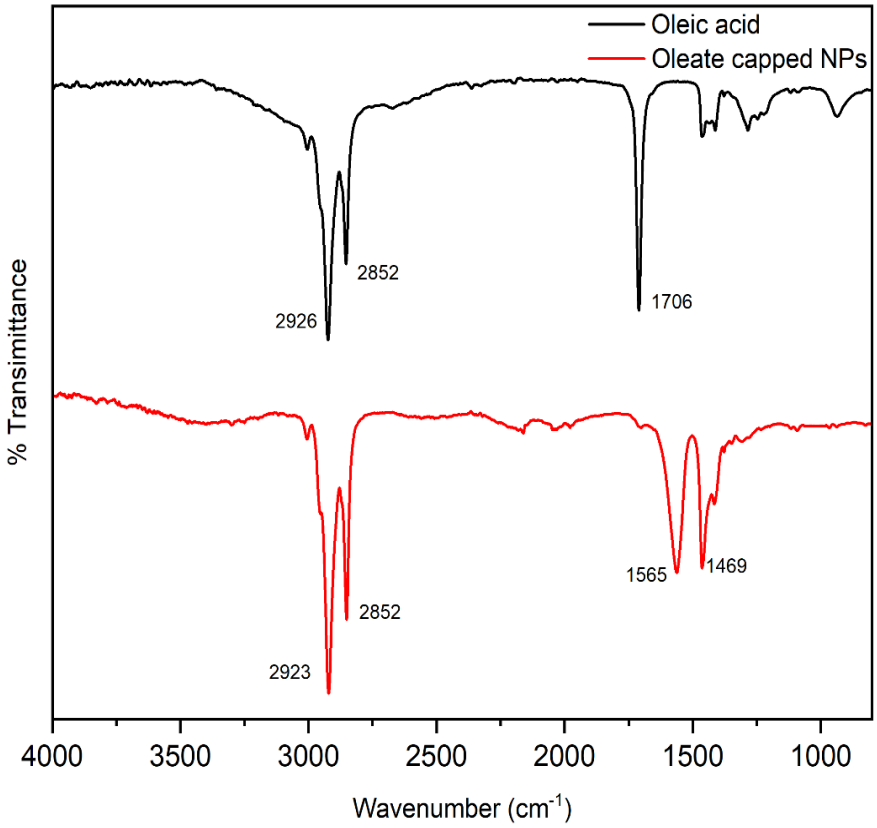

Figure 3. 3. Fourier transform infrared spectra of (—) oleic acid, and (—) oleate-capped $NaYF_4$: Yb^{3+}/ Er^{3+}.

3.2 Hexagonal phase $NaYF_4$:Yb^{3+}/Er^{3+} nanoparticles synthesized *via* thermal decomposition

Oleate capped hexagonal phase $NaYF_4$:Yb^{3+}/Er^{3+} nanoparticles were also synthesized *via* the thermal decomposition technique (section 2.1.2). In the upcoming section, the oleate capped nanoparticles used in this particular study were characterized using various techniques as described below.

3.2.1 Morphology and size

The nanoparticles synthesized by the thermal decomposition method exhibited a spherical morphology and an average size of 27 ± 3 nm based on the measurement of approximately 500 nanoparticles. Figure 3.4 shows the TEM image and size distribution of the nanoparticles.

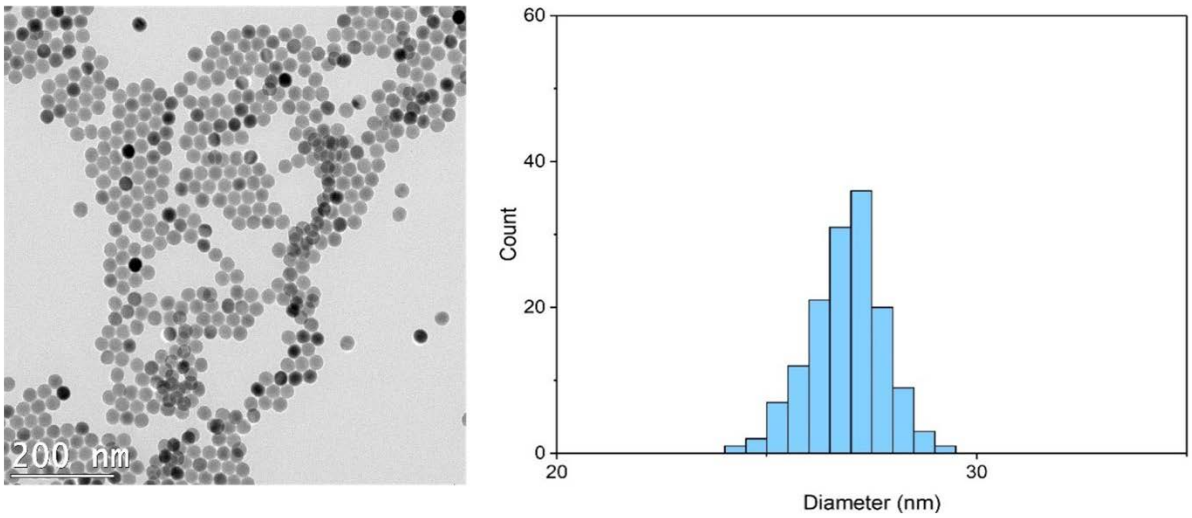

Figure 3. 4. Transmission electron micrograph (left) of oleate-capped $NaYF_4:Yb_{3+}/Er_{3+}$ hexagonal phase nanoparticles synthesized via thermal decomposition. Histogram (right) of the particle size distribution (27 ± 3 nm) from the TEM images (based on approximately 500 nanoparticles measured).

3.2.2 Crystal phase

The crystal phase was determined by using powder X-ray diffraction (XRD). Figure 3.5 shows the powder XRD diffraction of the hexagonal phase oleate capped $NaYF_4:Yb^{3+}/Er^{3+}$ and the calculated standard JCPDS pattern. The peak positions correspond closely to the reported pattern of hexagonal phase $NaYF_4$ (JCPDS no. 00-064-0156)

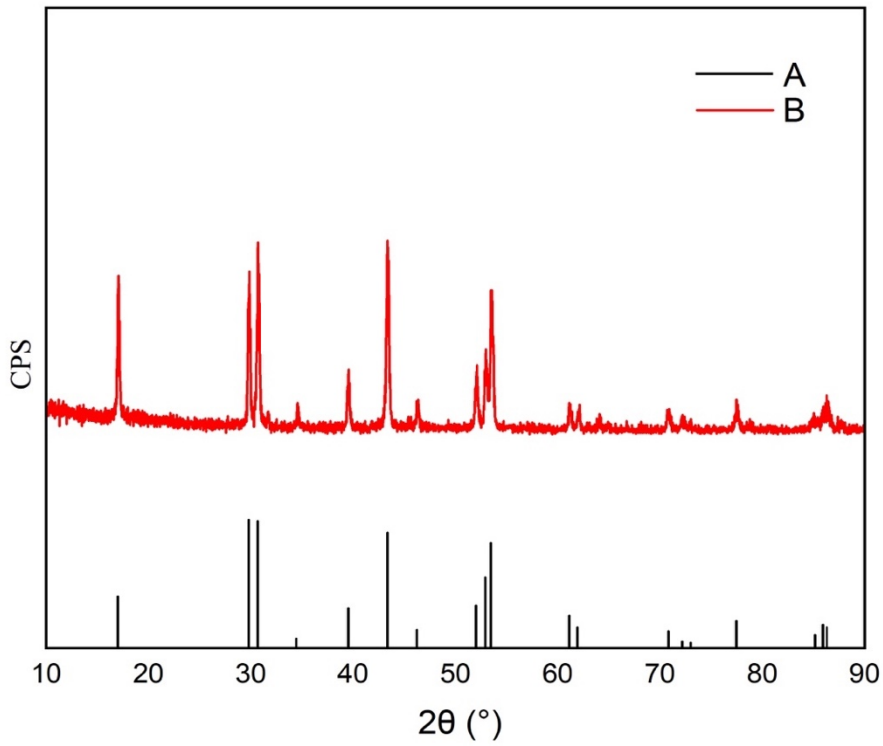

Figure 3. 5. Calculated standard (A) and experimental (B) XRPD Patters of $NaYF_4$ hexagonal phase (A) Reference pattern JCPDS File No. 00-064-0156, and (B) Oleate-capped hexagonal phase $NaYF_4$: Er^{3+}/Yb^{3+} UCNPs.

3.2.3 Surface characterization

The surface characterization of the synthesized $NaYF_4$:Er^{3+}/Yb^{3+} nanoparticles were performed using FTIR. The presence of oleate ions is confirmed by the peaks at 2927 cm^{-1} and 2850 cm^{-1}, in agreement with the analysis of the nanoparticle surface characterization described in section 3.1.3.

3.3 Cubic phase $NaYF_4:Yb^{3+}/Er^{3+}$ nanoparticles synthesized *via* thermal decomposition

Oleate capped cubic phase $NaYF_4:Yb^{3+}/Er^{3+}$ nanoparticles were synthesized *via* the thermal decomposition technique (section 2.1.2). The nanoparticles used in these studies were characterized using various techniques as described below.

3.3.1 Morphology and size

The nanoparticles synthesized by the thermal decomposition method exhibited a spherical morphology and an average size of 24 ± 3 nm based on the measurement of approximately 500 nanoparticles. Figure 3.6 shows the TEM image and size distribution of the nanoparticles.

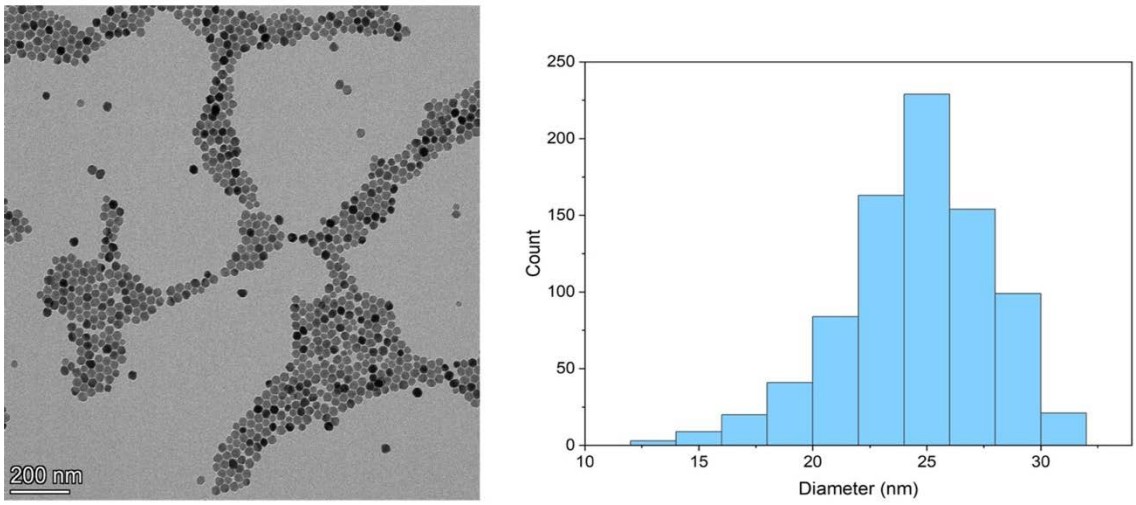

Figure 3. 6. Transmission electron micrograph (left) of oleate-capped $NaYF_4:Yb^{3+}/Er^{3+}$ cubic phase nanoparticles synthesized via thermal decomposition. Histogram (right) of the particle size distribution (24 ± 3 nm) from the TEM images (based on approximately 500 nanoparticles measured).

3.3.2 Crystal phase

The crystal phase was determined by using powder X-ray diffraction (XRD). Figure 3.7 shows the powder XRD diffraction of the cubic phase oleate capped $NaYF_4:Er^{3+}/Yb^{3+}$ and the calculated

standard JCPDS pattern. The peak positions correspond closely to the reported pattern of cubic phase $NaYF_4$ (JCPDS no. 00-006-0342)

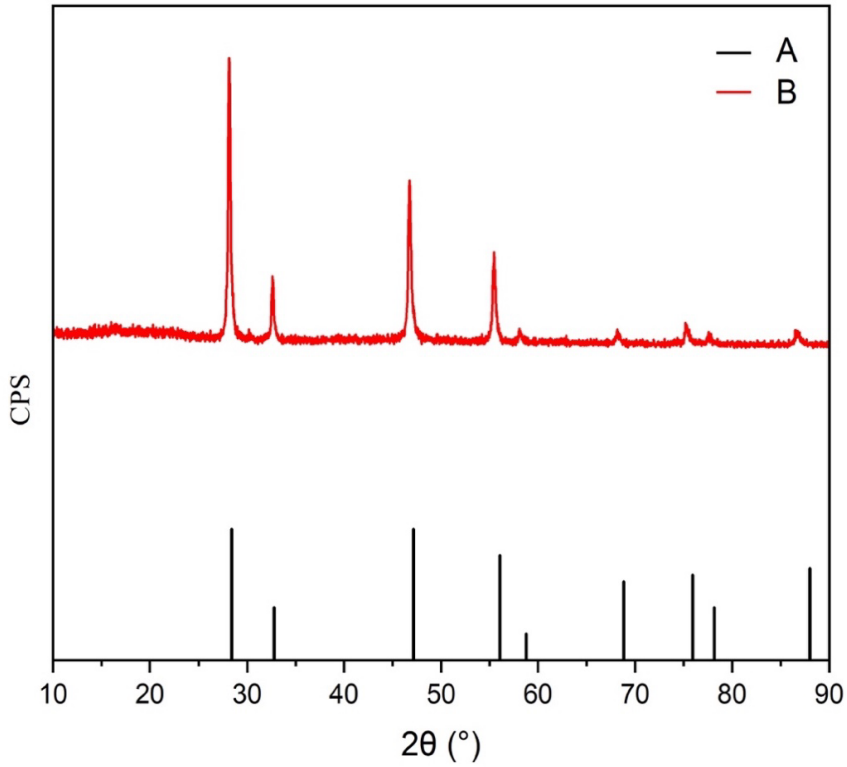

Figure 3. 7. Calculated standard (A) and experimental (B) XRPD Patters of $NaYF_4$ cubic phase (A) Reference pattern JCPDS File No. 00-006-0342, and (B) Oleate-capped cubic phase $NaYF_4:Yb^{3+}/Er^{3+}$ UCNPs.

3.3.3 Surface characterization

The surface characterization of the synthesized $NaYF_4:Er^{3+}/Yb^{3+}$ nanoparticles were performed using FTIR. The presence of oleate ions is confirmed by the peaks at 2933cm^{-1} and 2857 cm^{-1}, in agreement with the analysis performed for the nanoparticles in section 3.1.3.

3.4 Hexagonal phase NaGdF$_4$:Yb^{3+}/Er^{3+} nanoparticles synthesized *via* thermal decomposition

Oleate capped hexagonal phase NaGdF$_4$:Er^{3+}/Yb^{3+} nanoparticles were synthesized *via* the thermal decomposition technique (section 2.1.2). In the upcoming section, the oleate capped nanoparticles used in this particular study were characterized using various techniques as described below.

3.4.1 Morphology and size

Two different batches of NaGdF$_4$:Er^{3+}/Yb^{3+} nanoparticles were synthesized using the thermal decomposition method. The first batch of oleate capped NaGdF$_4$:Er^{3+}/Yb^{3+} hexagonal phase nanoparticles have a spherical morphology with an average size of 29 ± 4 nm, and the second batch exhibited spherical morphology with an average size of 11 ± 3. (~500 particles were calculated to obtain the average size and size distribution). Figure (3.8 and 3.9) shows the TEM image and size distribution of the oleate capped hexagonal phase NaGdF$_4$:Er^{3+}/Yb^{3+} nanoparticles.

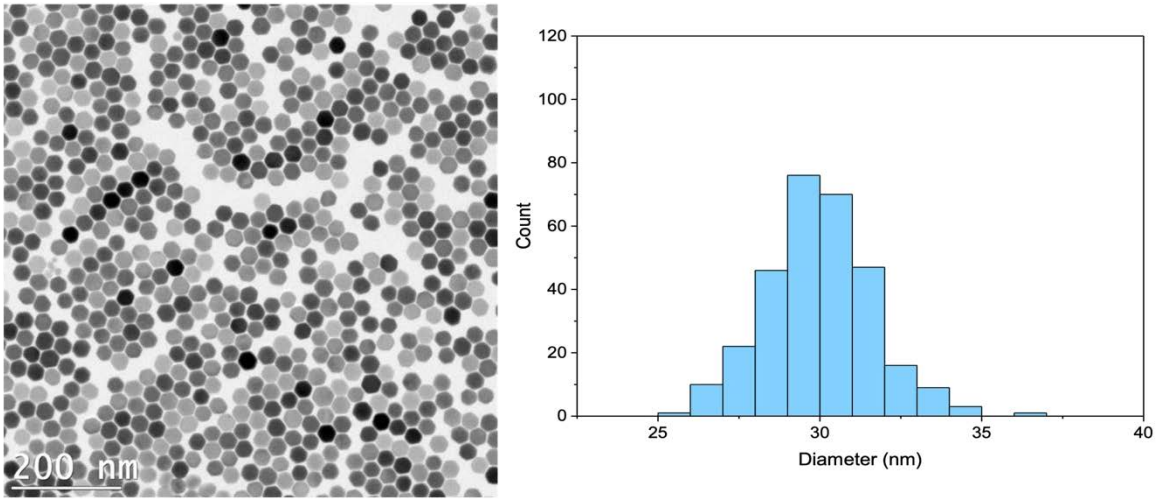

Figure 3. 8. Transmission electron micrograph (left) of oleate-capped NaGdF$_4$:Yb^{3+}/Er^{3+} hexagonal phase nanoparticles synthesized via thermal decomposition. Histogram (right) of the particle size distribution (29 ± 4 nm) from the TEM images (based on approximately 500 nanoparticles measured).

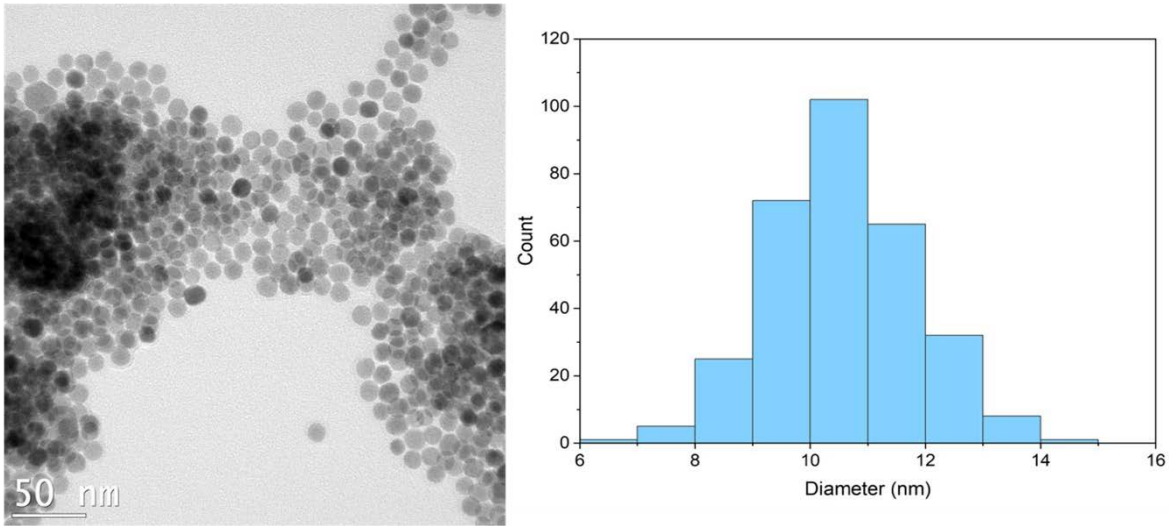

Figure 3. 9. Transmission electron micrograph (left) of oleate-capped $NaGdF_4:Yb^{3+}/Er^{3+}$ hexagonal phase nanoparticles synthesized via thermal decomposition. Histogram (right) of the particle size distribution (11 ± 3 nm) from the TEM images (based on approximately 500 nanoparticles measured).

3.4.2 Crystal phase

The crystal phase was determined by using powder X-ray diffraction (XRD). Figure 3.9 shows the powder XRD diffraction of the hexagonal phase oleate capped $NaGdF_4:Yb^{3+}/Er^{3+}$ and the calculated standard JCPDS pattern. The peak positions correspond closely to the reported pattern of hexagonal phase $NaGdF_4$ and thus confirms the crystal phase of the nanoparticle sample (JCPDS no. 00-270-699)

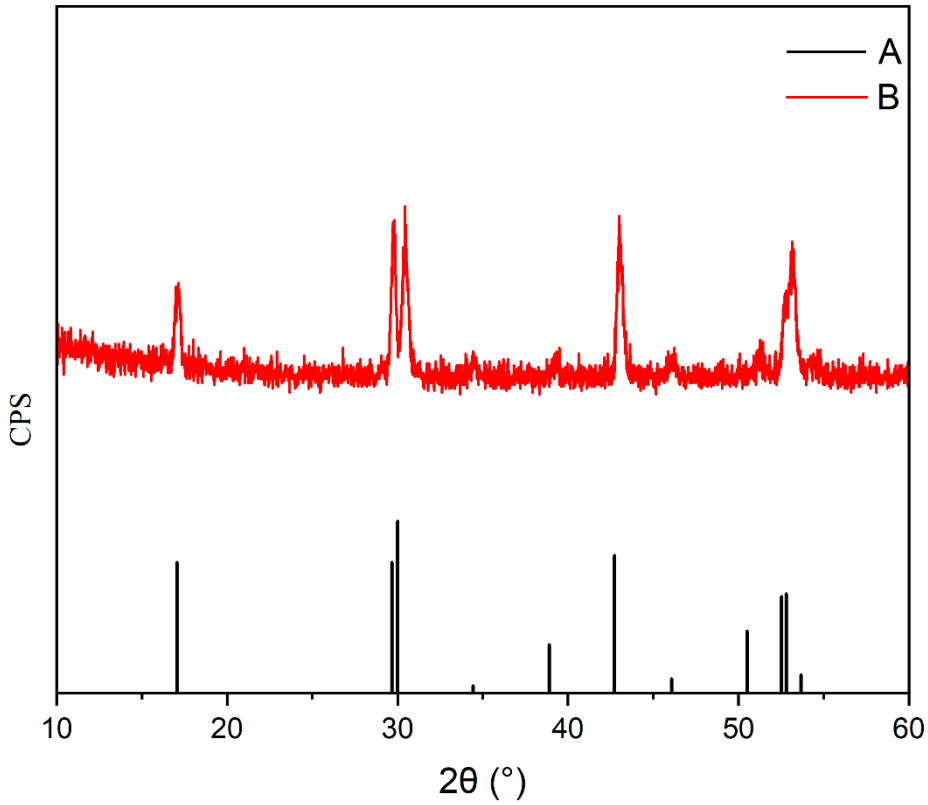

Figure 3. 10. Calculated standard (A) and experimental (B) XRPD Patters of $NaGdF_4$ hexagonal phase (A) Reference pattern JCPDS File No 00-270-699, and (B) Oleate-capped Hexagonal phase $NaGdF_4$: Yb^{3+}/ Er^{3+} UCNPs.

3.4.3 Surface characterization

The surface characterization of the synthesized $NaGdF_4$: Yb^{3+}/Er^{3+} nanoparticles were performed using FTIR. The FTIR spectrum of the oleate capped $NaGdF_4$:Yb^{3+}/Er^{3+} nanoparticles in accordance with the analysis performed for the nanoparticles in section 3.1.3. The presence of oleate ions on the surface of the nanoparticles is confirmed by the stretching vibrations at 2921 cm and 2855 originating from the asymmetric and symmetric stretches of -CH_2 groups, and the asymmetric and symmetric stretching bands of the carboxylate at 1565 and 1460 cm^{-1}.

Section number	Nanoparticle composition	Synthesis method	Crystal phase	Size (nm)
3.1	$NaYF_4$: Yb^{3+}/Er^{3+}	Coprecipitation	Hexagonal	39 ± 5
3.2	$NaYF_4$: Yb^{3+}/Er^{3+}	Thermal decomposition	Hexagonal	27 ± 3
3.3	$NaYF_4$: Yb^{3+}/Er^{3+}	Thermal decomposition	Cubic	24 ± 3
3.4	$NaGdF_4$: Yb^{3+}/Er^{3+}	Thermal decomposition	Hexagonal	29 ± 4
3.4	$NaGdF_4$: Yb^{3+}/Er^{3+}	Thermal decomposition	Hexagonal	11 ± 3

Table 3. 1. Summarizes the data on nanoparticles with their composition, synthesis method, crystal phase and the particle size used in this research work.

Chapter 4 - Results and discussion

The potential for growth of lanthanide doped upconverting nanoparticles at room temperature after initial nanoparticle synthesis *via* thermal decomposition or co-precipitation techniques was explored. This work involves the study of different parameters and their effect (such as the role of ligand, nanoparticles synthesis method, crystal phase, reaction time, and base used) on the growth of nanoparticles. Herein, the effect of each parameter on the potential for post-synthesis growth is examined.

4.1 Effect of no ligand

In order to assess whether the use of a ligand is crucial for obtaining the desired growth, control experiments were conducted in the absence of any ligand. Parameters such as synthesis method, nanoparticle composition, crystal phase, and different bases were varied in the absence of any ligands to ascertain the effect of the ligand in all cases. The particles used in the study were synthesized *via* the coprecipitation method and thermal decomposition which are characterized in chapter 3.

4.1.1 Effect of different nanoparticle composition without the presence of ligand

To evaluate if the nanoparticle composition plays a crucial role in the post synthesis growth mechanism, two different compositions were chosen. $NaYF_4$ and $NaGdF_4$ were synthesized *via* thermal decomposition, having same the dopant ions (Yb^{3+}/Er^{3+}). We opted for two different nanoparticle compositions based on work done by Wang *et al*., where they reported that the formation energy per atom of the hexagonal phase is increased by 0.07 eV when Y is replaced by Gd, proving $NaGdF_4$ is more energetically favorable.[28] The synthesis and characterization of

$NaYF_4$ and $NaGdF_4$ nanoparticles were reported in sections 3.2 and 3.4. $NaYF_4$ and $NaGdF_4$ nanoparticles were of size 27 ± 3 nm and 29 ± 4 nm, respectively, with a hexagonal crystal phase, and were synthesized with an oleate coating, which was removed *via* the protocol outlined in section 2.3. To achieve identical conditions for the ligand-free experiments as when the ligands are present, the pH of the nanoparticle-containing solution was increased to 11 using NaOH, and the samples were left to stir at room temperature for 3 days after which the nanoparticles were examined. The TEM and size of both $NaYF_4$ and $NaGdF_4$ nanoparticles on day 0 and day 3 are shown in figure 4.1 and table 4.1. Both nanoparticle compositions exhibited significant aggregation, and no change in morphology or size was observed. This indicates that it is likely the presence of a ligand is necessary for inducing the desired growth, and also to prevent undesirable aggregation effects.

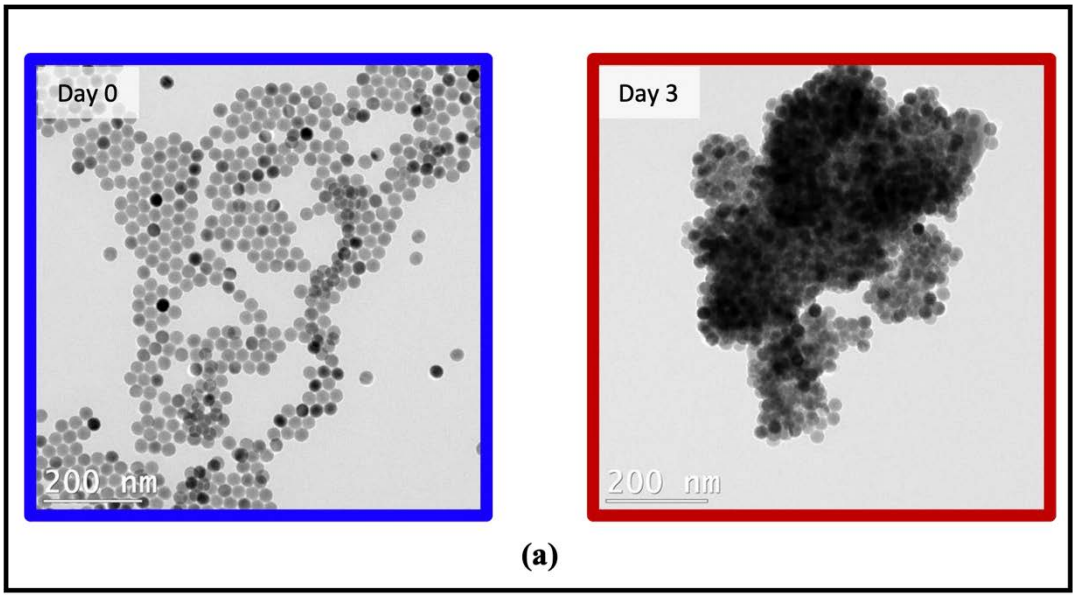

(a)

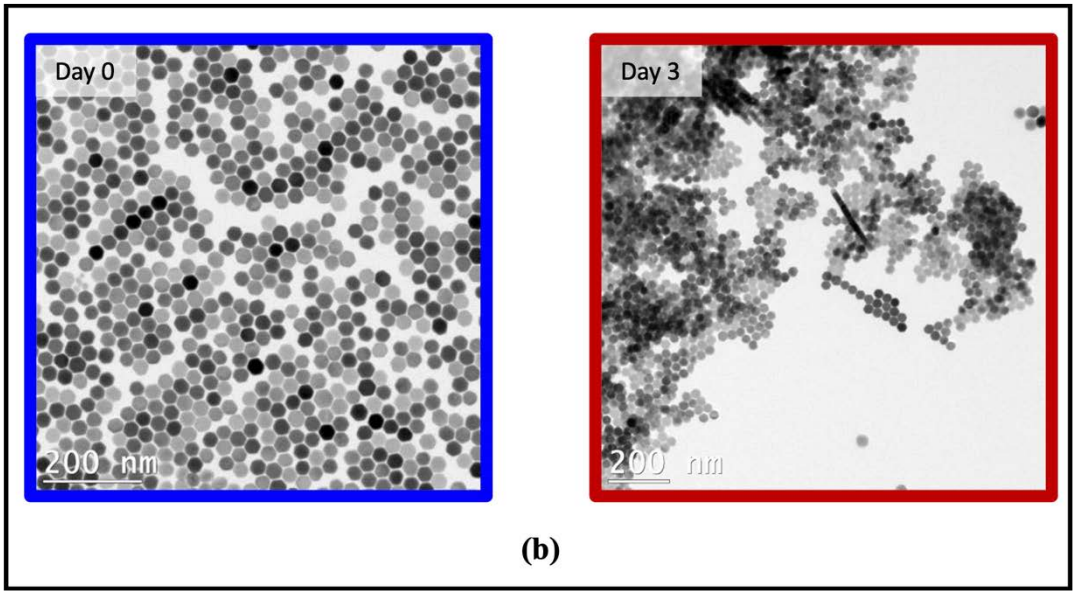

Figure 4. 1 TEM images of (a) $NaYF_4:Yb^{3+}/Er^{3+}$ nanoparticles on day 0 (left) and on day 3 (right), and (b) $NaGdF_4:Yb^{3+}/Er^{3+}$ nanoparticles on day 0 (left) and on day 3 (right) without the presence of ligand in NaOH.

Section number	Composition	Size (day 0) nm	Size (day 3) nm
3.3	$NaYF_4:Yb^{3+}/Er^{3+}$	27 ± 3	27 ± 2
3.5	$NaGdF_4:Yb^{3+}/Er^{3+}$	29 ± 4	28 ± 2

Table 4. 1. Mean particle size values for $NaYF_4:Yb^{3+}/Er^{3+}$ and $NaGdF_4:Yb^{3+}/Er^{3+}$ upconverting nanoparticles on day 0 and day 3 (without ligand).

4.2 Ligands for monitoring post-synthesis growth

After understanding and concluding the presence of a ligand is likely necessary for obtaining room temperature growth, we began investigating the effect of the use of ligands on the potential for growth. Two hydrophilic, multidentate, phosphonate-type ligands were used for the study. The selection of ligands were based upon the literature and the past work performed by Dr. Nicoleta Bogdan, a former post-doctoral fellow under the supervision of Professor Capobianco. The research published by Duong *et al.*[42] provided the evidence for the selection of phosphate type

ligands to study nanoparticle growth, as they provide enhanced stability and great affinity towards the positively charged surface of the lanthanide doped nanoparticles, whereas the previous unpublished experiments performed by Dr. Bogdan directed us towards the use of a multidentate phosphonate ligand. The two multidentate phosphonate type ligands studied were ethylene-diamine-tetra(methylene-phosphonic) acid (EDTMP) and 2,6-bis[(N,N-bis(methylene phosphonic acid)aminomethyl] pyridine (AL238B). Figure 4.2 shows the structure of the ligands used in the study. Both of these ligands have been utilized in the formation of a variety of lanthanide complexes, hence it is well-documented that these ligands interact efficiently with lanthanide ions.[61,62]

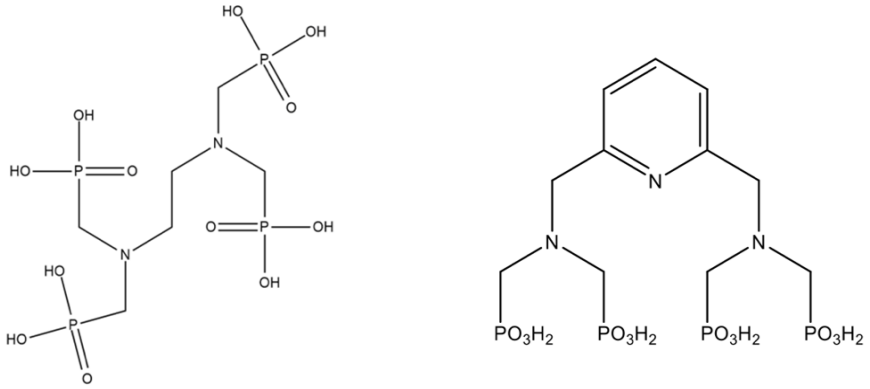

Figure 4. 2. Shows the structure of ligand (a) EDTMP, and (b) AL238B used in this study.

EDTMP

Ethylene-diamine-tetra(methylene-phosphonic) acid is commercially available, and was chosen because of its close structural resemblance with AL238B and is water soluble. In order to investigate the structural importance of the ligand to induce growth.

AL238B

2,6-bis[(N,N-bis(methylene phosphonic acid)aminomethyl] pyridine scaffold is not commercially available and was synthesized through a 5 step route (see section 2.2). This ligand was used in the experiments by Dr. Bogdan for the preliminary results which paved a path to explore the possibility of room temperature growth. Unlike EDTMP, the pyridine scaffold in AL238B provides the additional possibility for π- stacking, which could be an additional factor for witnessing the growth of the nanoparticles.

4.3 Studies with EDTMP

In this section, we have tried to study the effect of coordinating the EDTMP ligand onto the nanoparticles, with a systematic investigation of different parameters (such as nanoparticles synthesis method, nanoparticles composition) and the effect on the size and morphology of the nanoparticles.

4.3.1 Effect on post-synthesis growth of $NaYF_4:Yb^{3+}/Er^{3+}$ nanoparticles with EDTMP

The effect of nanoparticles synthesized *via* different methods (coprecipitation and thermal decomposition) in the presence of EDTMP was studied. It has been well-documented that the nanoparticles prepared *via* the thermal decomposition method exhibit high crystallinity.[63] Thus, $NaYF_4:Yb^{3+}/Er^{3+}$ nanoparticles were synthesized by both coprecipitation and thermal decomposition (section 3.1 and 3.2) to examine if the synthesis method had any additional effect on the post synthesis growth.

The nanoparticles synthesized *via* both methods were subjected to ligand exchange *via* the protocol explained in section 2.3 to replace the as-synthesized oleate capping ligand with EDTMP. A 1:1

mass ratio of oleate capped nanoparticles to ligand ratio was taken and the pH was adjusted to 11 by using NaOH, to ensure the EDTMP was fully deprotonated and able to electrostatically bind to the positively-charged surface of the nanoparticles, after which the nanoparticles were left on stirring for a period of 3 days to give time to the nanoparticles to show any morphological changes or growth. The EDTMP-coated nanoparticles were purified by repeated centrifugation to remove excess ligand, and to obtain nanoparticles. FTIR was performed to confirm the presence of EDTMP on the nanoparticles. The removal of COO^- asymmetric and symmetric stretching vibrations at 1552 cm^{-1} and 1485 cm^{-1} from the oleate and the introduction of signals between 1012 cm^{-1} and 1055 cm^{-1} due to phosphonate groups confirms the binding of EDTMP onto the surface of the nanoparticles (Figure 4.3). Transmission electron microscopy (TEM) analysis was carried out to investigate the effect of EDTMP post-synthesis on the size and morphology of the nanoparticles after 3 days of incubation. (figure 4.4 a and b)

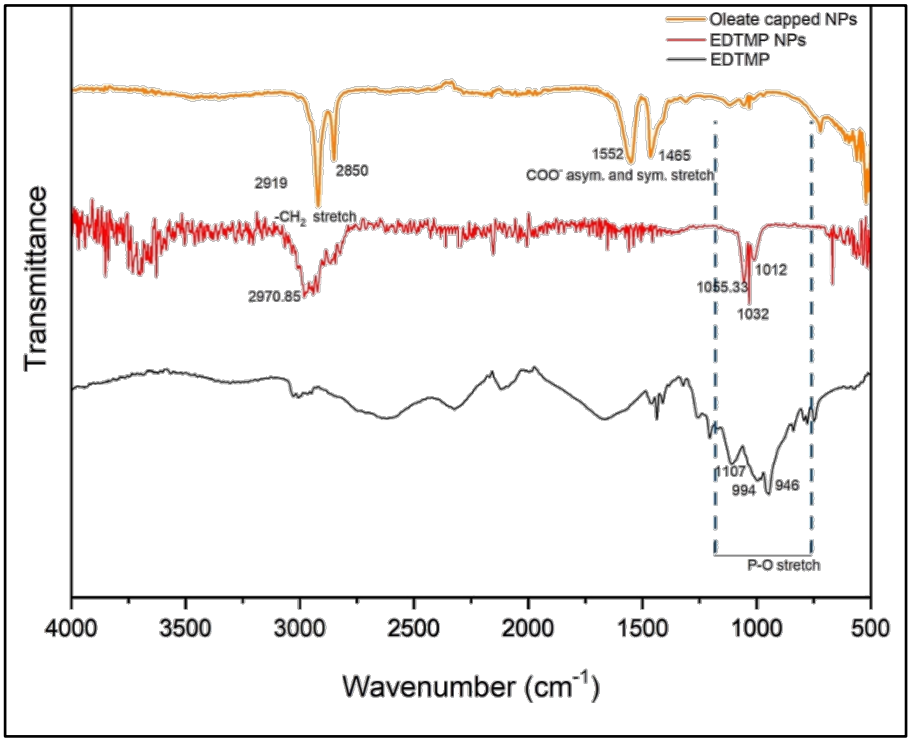

Figure 4. 3. FTIR analysis of ligand EDTMP capped $NaYF_4:Yb^{3+}/Er^{3+}$ nanoparticles on day 3.

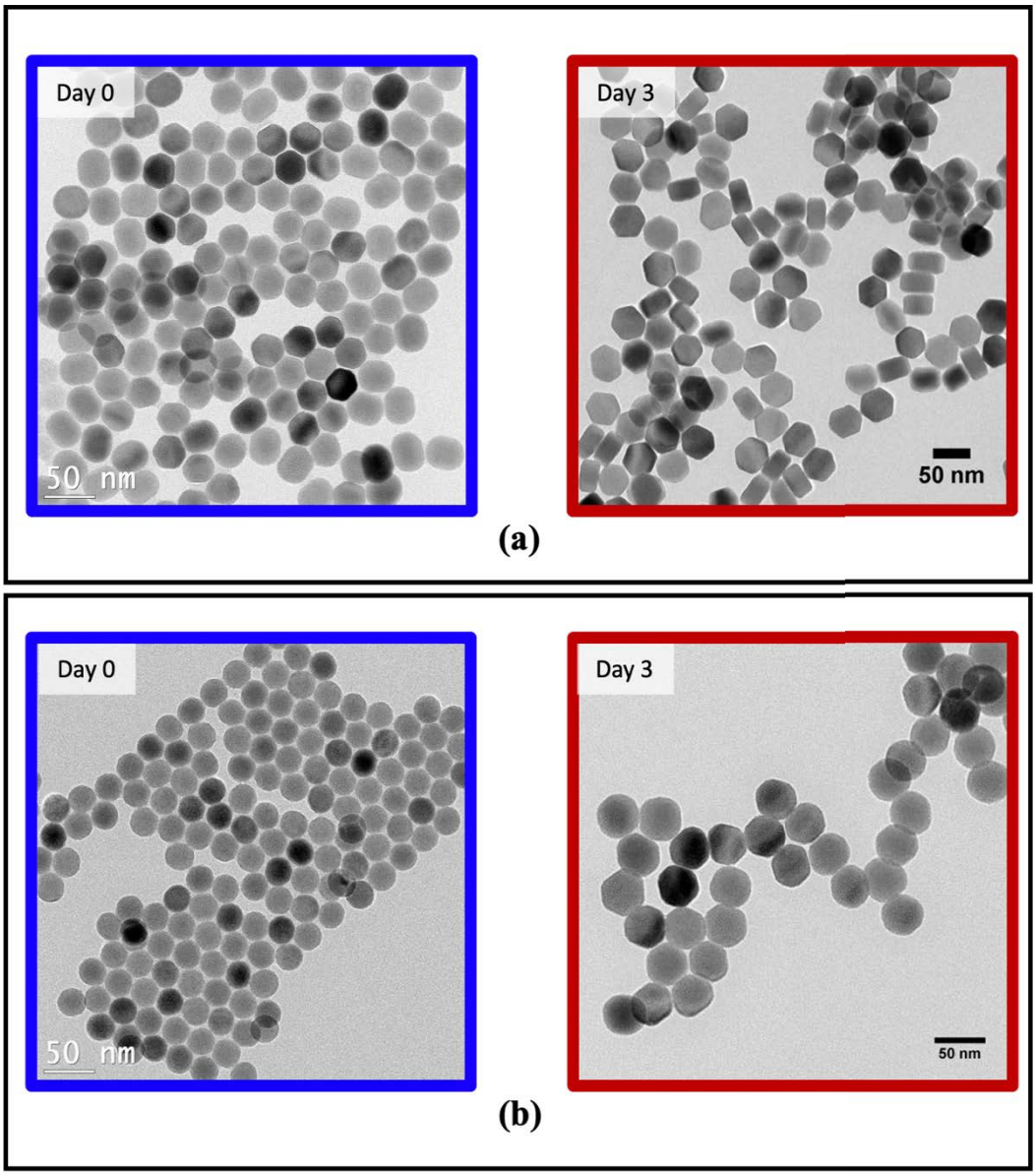

Figure 4. 4. Transmission electron microscopy images of $NaYF_4:Yb^{3+}/Er^{3+}$ synthesized via (a) coprecipitation day 0 (left) and on day 3 (right), and (b) thermal decomposition day 0 (left) and on day 3 (right) with post synthesis ligand exchange with EDTMP in NaOH.

Upon investigation of the TEM images, it was observed that the nanoparticles had undergone a minimal change in morphology of the nanoparticles in both cases, irrespective of the initial nanoparticle synthesis method. The particles synthesized by coprecipitation on day 0 (figure 4.4 a) exhibited an undefined hexagonal morphology with an average size of 39 ± 5 nm, whereas

particles synthesized *via* thermal decomposition on day 0 displayed a spherical morphology with a size of 27 ± 3 nm (figure 4.4 b). After three days of incubation with EDTMP, both $NaYF_4:Yb^{3+}/Er^{3+}$ synthesized via thermal decomposition and coprecipitation were found to exhibit a moderately hexagonal morphology, with minimal size changes that are within the margin of error of the measurements. The mean particle sizes are summarized in table 4.2. The slight change in nanoparticle morphology is attributed to the higher affinity of EDTMP towards the planes of the nanoparticles surface as suggested by Duong *et al.*[42] Thus, it was determined that the presence of EDTMP induces minor morphological changes but did not induce significant growth at room temperature.

To extend the scope of our research, we further used $NaGdF_4:Yb^{3+}/Er^{3+}$ nanoparticles, synthesized *via* thermal decomposition (Section 3.5). The particles underwent the same ligand exchange protocol as explained above to introduce EDTMP to the nanoparticle surface. The nanoparticles on day 0 exhibited a well-defined hexagonal morphology with a size of 29 ± 4 nm, and on day 3 the same size and morphology were observed, as shown in figure 4.5. The lack of change in both size and morphology was attributed to the extra energetic stability of $NaGdF_4:Yb^{3+}/Er^{3+}$over $NaYF_4:Yb^{3+}/Er^{3+}$ particles.[28] This again suggests that the presence of the EDTMP ligand is not sufficient to induce any sort of nanoparticle growth.

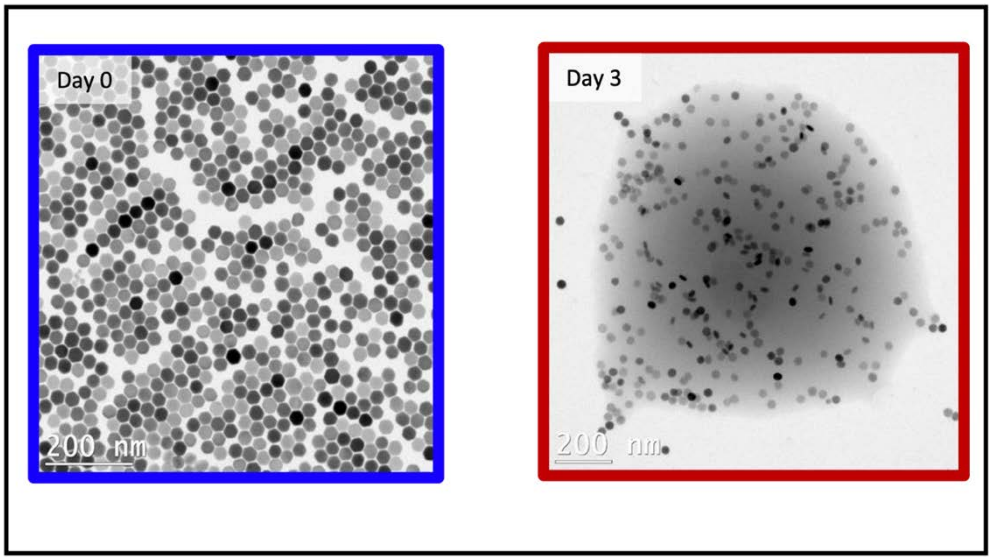

Figure 4. 5. Transmission electron microscopy images of $NaGdF_4:Yb^{3+}/Er^{3+}$ synthesized via thermal decomposition day 0 (left) and on day 3 (right) subjected to post synthesis ligand exchange with EDTMP in NaOH.

Section no	composition	Synthesis method	Crystal phase	Size (day 0) nm	Size (day 3) nm	Morphology (day 0)	Morphology (day 3)
3.1	$NaYF_4$: Yb^{3+}/ Er^{3+}	coprecipitation	hexagonal	39 ± 5	38 ± 4	undefined	sharp hexagonal
3.2	$NaYF_4$: Yb^{3+}/ Er^{3+}	Thermal decomposition	hexagonal	27 ± 3	25 ± 2	spherical	hexagonal
3.4	$NaGdF_4$: Yb^{3+}/ Er^{3+}	Thermal decomposition	hexagonal	29 ± 4	28 ± 2	hexagonal	hexagonal

Table 4. 2. Mean particle size values for $NaYF_4:Yb^{3+}/Er^{3+}$ and $NaGdF_4:Yb^{3+}/Er^{3+}$ upconverting nanoparticles on day 0 and day 3 with EDTMP ligand.

4.4 Studies with AL238B

The second ligand used in this study was AL238B which has been studied previously in our group, and has shown promising results, but in order to have a clear understanding of what parameters

are essential to observe post-synthesis growth, we performed a study of different parameters and their effect (such as nanoparticles synthesize method, crystal phase, reaction time, and base used) on the growth of nanoparticles.

4.4.1 Effect on post-synthesis growth of nanoparticles with AL238B

The studies of post synthesis growth of lanthanide doped nanoparticles were done in an identical manner to the studies performed using the EDTMP ligand. $NaYF_4:Yb^{3+}/Er^{3+}$ nanoparticles synthesized by both coprecipitation and thermal decomposition (section 3.1 and 3.2) were studied with AL238B, as nanoparticles synthesized *via* different methods differ in crystallinity as mentioned in section 4.3.1. All nanoparticles were subjected to ligand exchange as described in section 2.3. As with EDTMP, again a 1:1 mass ratio was oleate capped nanoparticles to ligand was taken and the pH was adjusted to 11 by using NaOH, so the ligand can electrostatically bind to the surface of the nanoparticles, after which the solution was left on stirring for 3 days, in order to provide time for morphological changes and the growth process to occur. The nanoparticles were then recaptured by centrifugation to remove excess of ligand. FTIR was performed on the nanoparticles to confirm the presence of AL238B on the nanoparticles, the removal of COO^- asymmetric and symmetric stretches at 1552 cm^{-1} and 1465 cm^{-1} from the oleate and the introduction of signals between 1046 cm^{-1} and 970 cm^{-1} due to phosphonate groups confirms the binding of AL238B onto the surface of the nanoparticles (Figure 4.6). Transmission electron microscopy (TEM) analysis was carried out to investigate the effect of AL238B post synthesis on the size and morphology of the nanoparticles synthesized *via* both methods on day 3. (figure 4.7)

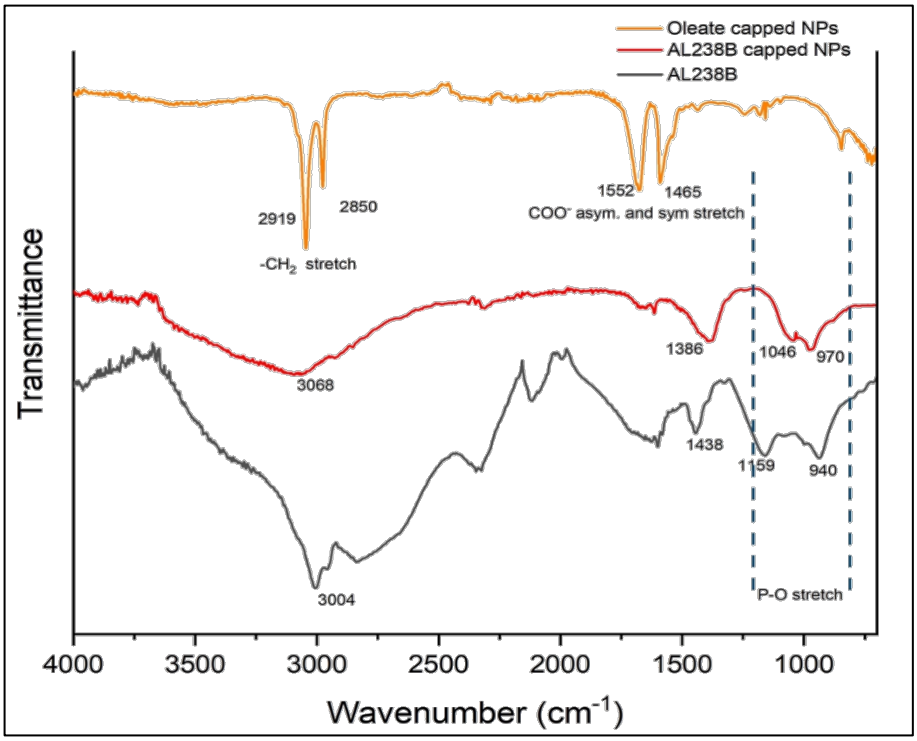

Figure 4. 6. FTIR analysis of ligand AL238B capped $NaYF_4:Yb^{3+}/Er^{3+}$ nanoparticles on day 3.

Upon TEM image examination of figure 4.7, it was observed that on day 3 for the $NaYF_4:Yb^{3+}/Er^{3+}$ nanoparticles that were synthesized by co-precipitation, a significant change in the morphology of the nanoparticles was observed. The nanoparticles showed the formation of connective necking on the interface of the nanoparticles. Similar findings were discussed by Guo et al[55] for gold nanoparticles, where gold nanoparticles showed coalescence without ligand deattachment. The driving force for seeing the necking could be attributed to the interaction between the ligands (in this case possibly due to π- stacking), since the surface energy in the nanoparticles is facet dependent, the number density of the ligands interacting with a particular crystal phase will vary. This difference in the ligand densities between the facets can facilitate directional growth along specific planes where the surface of the nanoparticles is poorly covered by the ligand, this whole process will reduce the overall surface energy of the nanoparticles. However, the individual

particle size on day 0 and day 3 remained unaltered, indicating that while necking was observed, it was not inducing significant growth.

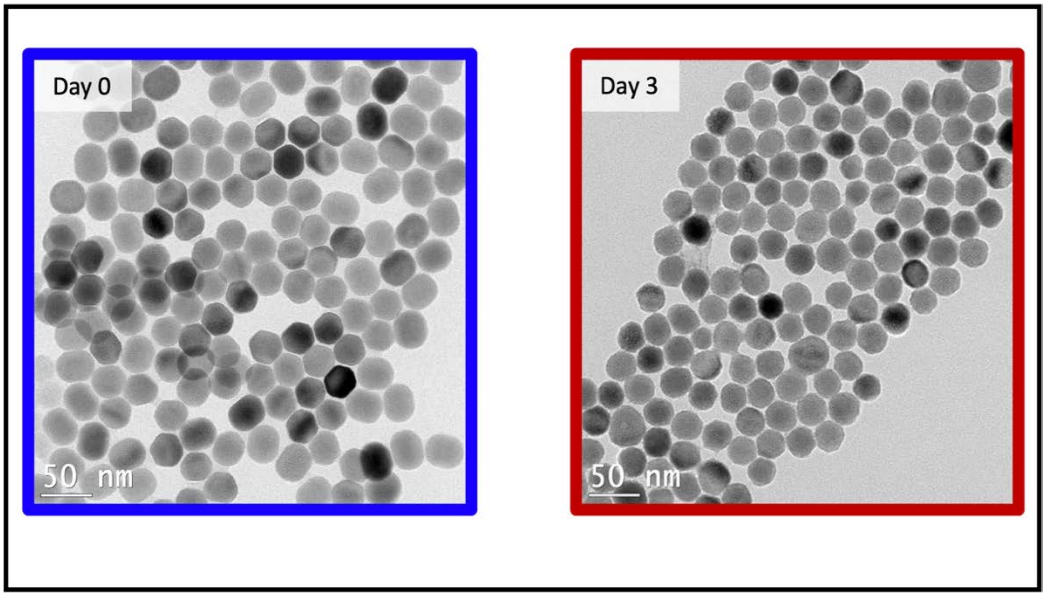

Figure 4. 7. Transmission electron microscopy images of $NaYF_4:Yb^{3+}/Er^{3+}$ synthesized via (a) coprecipitation day 0 (left) and on day 3 (right) subjected to post synthesis ligand exchange with AL238B in NaOH. On day 3 (right) necking of nanoparticles were observed.

Nanoparticles synthesized by thermal decomposition, (both $NaYF_4:Yb^{3+}/Er^{3+}$ and $NaGdF_4:Yb^{3+}/Er^{3+}$) didn't show any changes in morphology or the size of the nanoparticles, as shown in Figures 4.8 a and b. With respect $NaYF_4:Yb^{3+}/Er^{3+}$, the apparent lack of dependence on the observation of necking as a function of synthesis method is postulated to be due to the observation that lanthanide upconverting nanoparticle synthesis by thermal decomposition leads to the formation of particles with higher crystallinity, which results in reduced defects compared to co-precipitation. Therefore, there are fewer defects in particles prepared by thermal decomposition, which leads to an overall decrease in the surface energy, hindering the coalescence of nanoparticles. For the $NaGdF_4:Yb^{3+}/Er^{3+}$ particles, the extra energetic stability of $NaGdF_4$ over

$NaYF_4$ particles in addition to the high crystallinity is postulated to be the reason for the lack of coalescence.

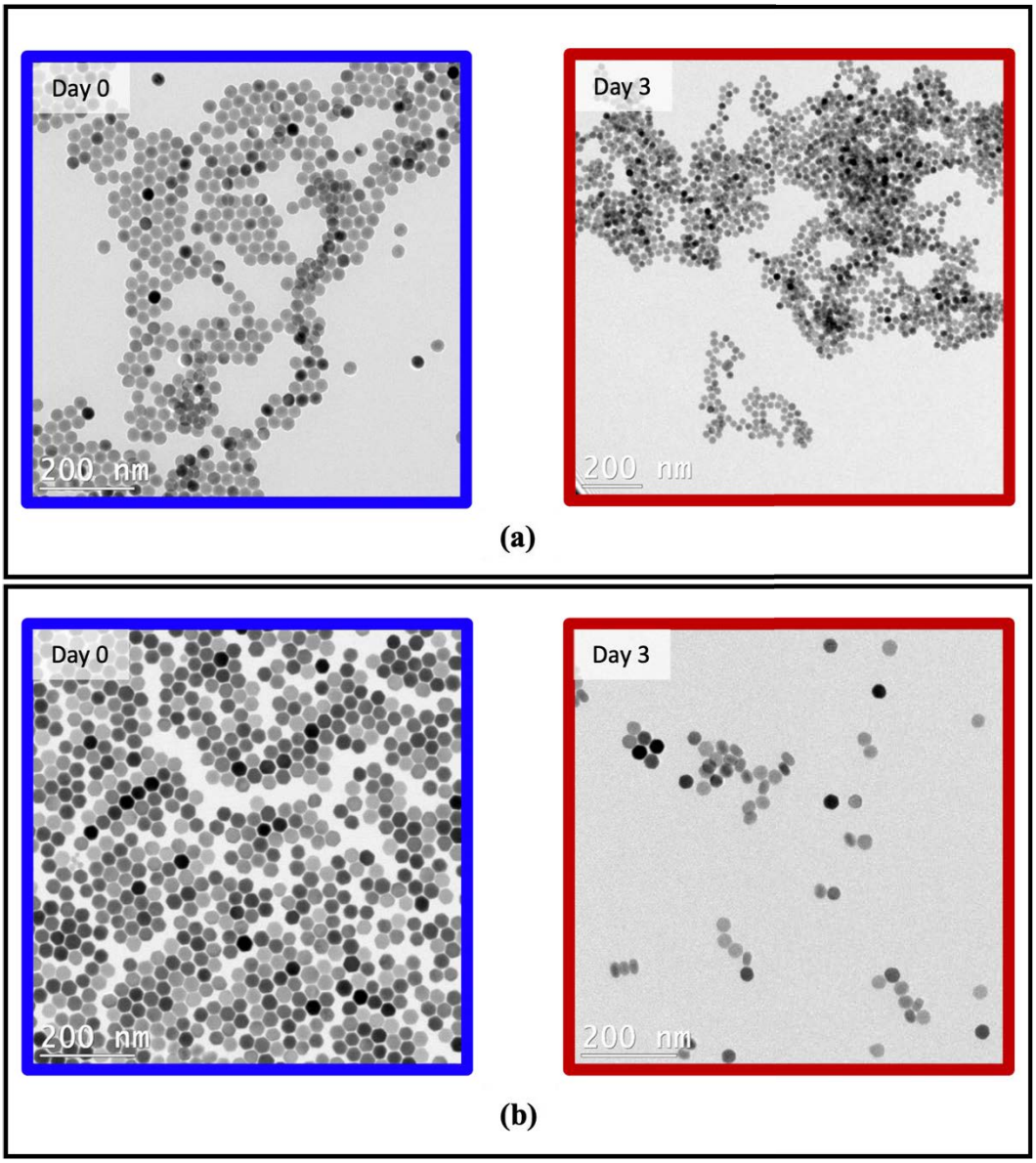

Figure 4. 8. Transmission electron microscopy images of (a)$NaYF_4$:Yb^{3+}/Er^{3+} and (b) $NaGdF_4$:Yb^{3+}/Er^{3+} synthesized via thermal decomposition day 0 (left) and on day 3 (right) with AL238B in NaOH, showing no significant change in the morphology or size of the nanoparticles.

These experiments revealed that the synthesis method opted for synthesizing our nanoparticles could affect the post-synthesis growth of the nanoparticles. Despite the lack of growth observed in the absence of ligand and the presence of EDTMP thus far, further tests were carried out with nanoparticles synthesized by thermal decomposition. In these experiments, the only parameter that was altered was the base used to modulate the pH of the solution. It is believed that the base used to modulate the pH had two roles, first to deprotonate the phosphonate group, in order to have the ligand interacting with the nanoparticle surface, and secondly, the counter cation of the base, could potentially replace Na^+ ions present on the surface of the nanoparticles ($\underline{Na}YF_4/\underline{Na}GdF_4$). This phenomenon was reported by Han *et al*.[64] where they produced multicolour lanthanide-doped nanoparticles through cation exchange of the lanthanide ions on the surface of nanoparticles in water by using substituting lanthanide of identical valence charge. In a similar manner, the replacement of Na^+ ions by the counter cation of the base can take place, and potentially disturb the crystal lattice because of the difference in the sizes of the cation, which would further increase the surface energy. The increased surface energies would potentially improve the likelihood of observing phenomena like oriented attachment, Ostwald ripening, and necking which we postulate would facilitate nanoparticle growth.

The effect of altering the base from NaOH to KOH was analyzed using $NaYF_4:Yb^{3+}/Er^{3+}$ and $NaGdF_4:Yb^{3+}/Er^{3+}$ synthesized *via* thermal decomposition (section 3.2 and 3.4) having a size of 27 ± 3 nm, and 29 ± 4 nm respectively on day 0 of the experiment. The nanoparticles were subjected to ligand exchange *via* the protocol explained in section 2.3, with KOH as a base instead of NaOH to explore the hypothesis. After 3 days of incubation, the nanoparticles were analyzed using TEM (Figure 4.9).

Upon examination of the TEM images, a significant change in size and morphology were observed. In the case of $NaYF_4$ particles, the initial nanoparticle size distribution ranged from 23 nm to 32 nm. After 3 days, no particles were observed in that size range; instead, two size distributions were observed (figure 4.9). The first distribution consisted of very small nanoparticles ranging from 4 nm to 12 nm in size, and the second distribution consisted of larger nanoparticles ranging from 30 nm to 46 nm, with a drastic change in morphology (figure 4.9). The presence of two size distributions, one smaller and one larger than the initial nanoparticles, indicates Ostwald ripening[65] was likely taking place. This is postulated to be due to the defects induced in the crystal

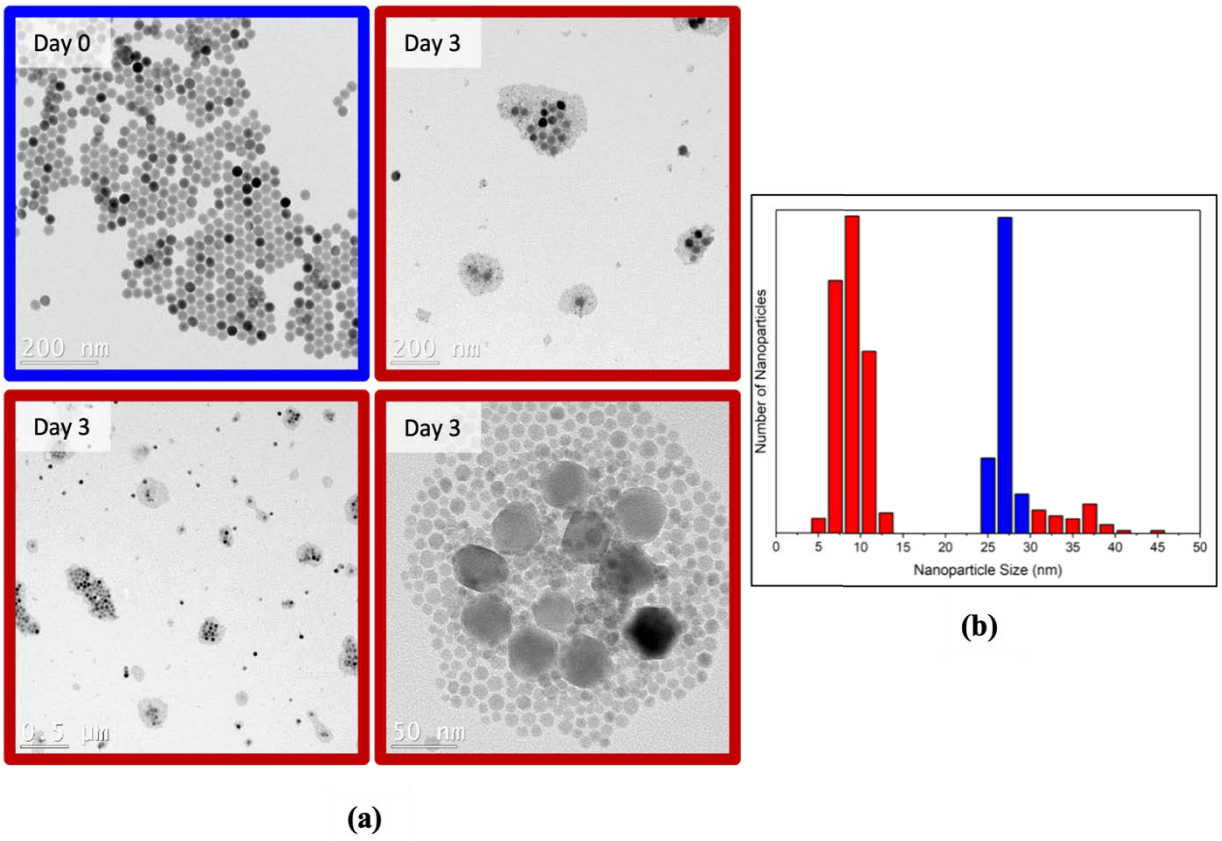

Figure 4. 9. Transmission electron microscopy images of (a) $NaYF_4:Yb^{3+}/Er^{3+}$ synthesized via thermal decomposition day 0 (blue outline) and on day 3 (red outline) with AL238B in KOH, showing significant change in the morphology and the size of the nanoparticles, (b) shows the size distribution of particles on day 0 (blue), and on day 3(red) with two size distribution.

lattice caused by the K^+ ions replacing the Na^+ ions in the lattice and causing the dissolution and reprecipitation of the nanoparticles.

Similar results were obtained with $NaGdF_4$ nanoparticles, the original size of the nanoparticles were between 28 nm to 30 nm and on day 3 no particles in this size range were observed, and again two other size distributions, smaller and larger than the original particles, were observed. One distribution of very small size ranging from 12 nm to 20 nm and one of larger nanoparticles having an irregular morphology, ranging from 42 nm to 58 nm. Additionally, nanoparticles with a defined hexagonal morphology having sizes greater than 100 nm were observed(Figure 4.10).

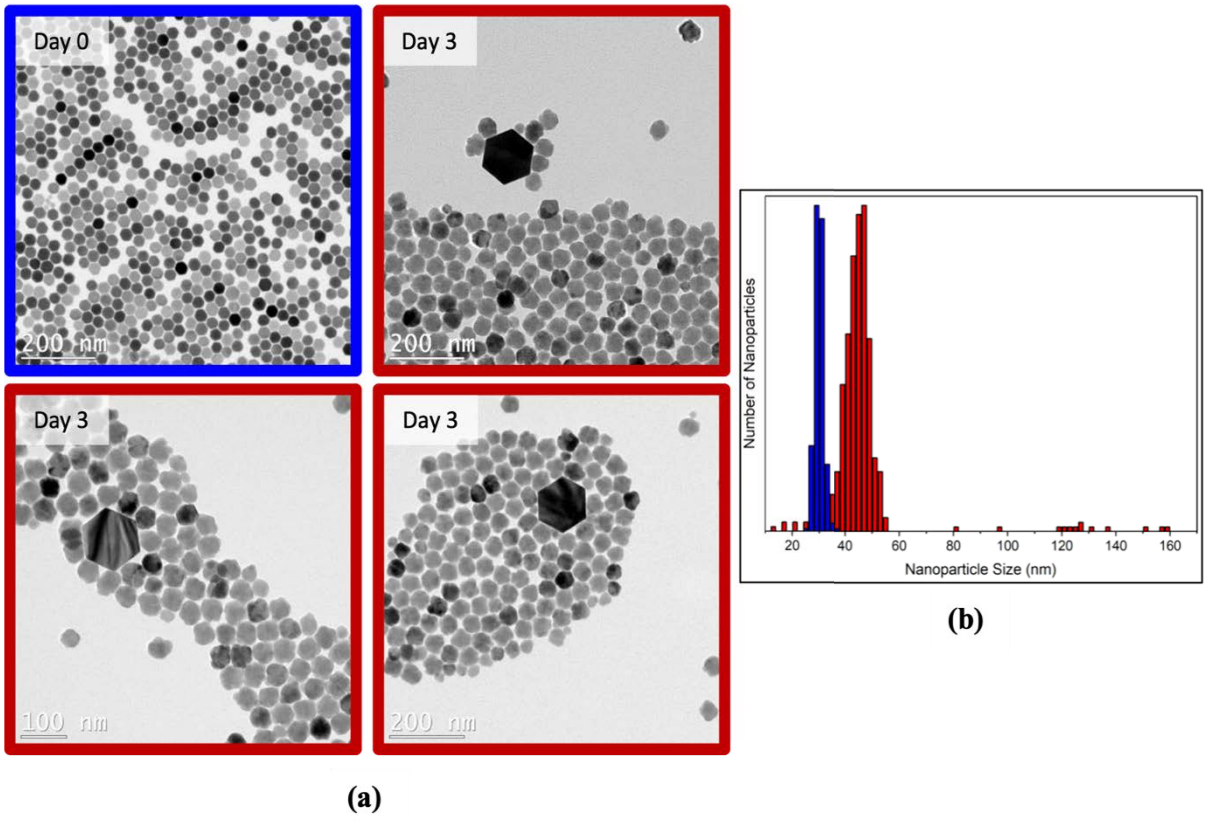

Figure 4. 10. Transmission electron microscopy images of (a) $NaGdF_4:Yb^{3+}/Er^{3+}$ synthesized via thermal decomposition day 0 (blue outline) and on day 3 (red outline) with AL238B in KOH, showing significant change in the morphology and the size of the nanoparticles, (b) the size distribution of particles on day 0 (blue), and on day 3 (red) with two size distributions.

The change in morphology of the intermediate-sized nanoparticles from a defined hexagonal shape to a non uniform shape, combined with the presence of significantly larger nanoparticles is quite possibly due to the use of KOH and the introduction of the K^+ ions which alter the equilibrium of free ions in solution and bound ions in the nanocrystal lattices. In prior studies, the use of NaOH as a base introduced significant amounts of free Na^+ ions into the solution, which reduced the ionic differential between the colloidal nanoparticles possessing high amounts of Na^+ ions and the solvent, which also contained high concentrations of Na^+ ions upon addition of NaOH. When NaOH was replaced with KOH, this equilibrium was disturbed. This disturbance facilitates the likelihood for K^+ ions to replace Na^+ ions in the nanoparticle surface, creating defects in the nanocrystal lattice. It can be inferred from the significant change in nanoparticle morphology that the etching of the surface of the nanoparticles occurred, introducing significant surface defects in the crystal lattice. The increased surface energy, then resulted in the release of Na^+ and F^- ions into the solution, which reprecipitated onto other nanoparticles, resulting in their growth, through a process similar to Ostwald ripening. As discussed in section 1.4.1.2, Ostwald ripening occurs after the initial seeding phase, after the concentration of monomers (ions) in the solution has decreased. In this case, we postulated that since NaOH was replaced with KOH, the Na^+ "monomers" were no longer present in the solution, facilitating this Ostwald ripening-type change. However, given that these findings are based on a limited number of trials, the reproducibility of the same results was tested with the same protocol and the same nanoparticles used in the previous study. Contrary to expectations, on examining the TEM images of both the $NaYF_4$ and $NaGdF_4$ samples with identical parameters on day 3, no signs of smaller or larger nanoparticles were observed (Figure 4.11 a and b). The reason for the lack of reproducibility is still not entirely clear. However, efforts to potentially determine why the results are not reproducible were carried out to

try and unravel the forces that govern the success or failure of the growth experiments. Table 4.3 summarizes the result obtained when the particles synthesized via thermal decomposition were subjected to ligand exchange with KOH as a base.

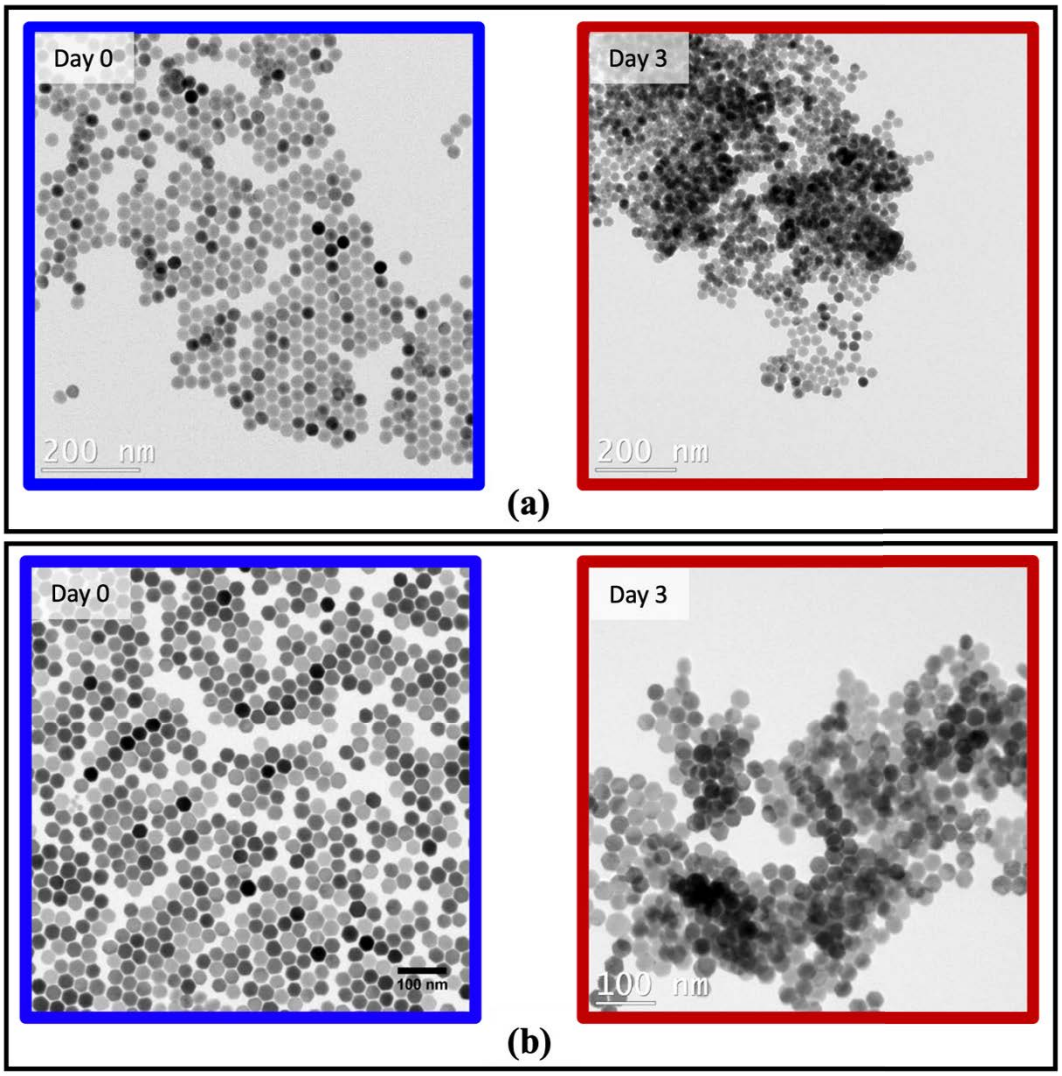

Figure 4. 11. Transmission electron microscopy images of (a) $NaYF_4:Yb^{3+}/Er^{3+}$ and (b) $NaGdF_4:Yb^{3+}/Er^{3+}$ synthesized via thermal decomposition day 0 (left) and on day 3 (right) with AL238B in KOH, showing no significant change in the morphology or size of the nanoparticles.

Section no	Composition	Synthesis method	Crystal phase	Base used	Size (day 0) nm	Size (day 3) nm	Morphology (day 0)	Morphology (day 3)
3.2	$NaYF_4:Yb^{3+}/Er^{3+}$	Thermal decomposition	Hexagonal	KOH	27 ± 3	4-12; 30-46	Spherical	Irregular
3.4	$NaGdF_4:Yb^{3+}/Er^{3+}$	Thermal decomposition	Hexagonal	KOH	29 ± 4	12-20; 42-58	Hexagonal	Irregular
3.2	$NaYF_4:Yb^{3+}/Er^{3+}$	Thermal decomposition	Hexagonal	KOH	27 ± 3	24 ± 2	spherical	spherical
3.4	$NaGdF_4:Yb^{3+}/Er^{3+}$	Thermal decomposition	Hexagonal	KOH	29 ± 4	27 ± 2	Hexagonal	Hexagonal

Table 4. 3. Summary of the mean particle size of the nanoparticles and morphological changes on day 0 and day 3 with KOH in the presence of AL238B ligand.

Previous unpublished results by our group indicated the use of a mixture of cubic and hexagonal phase nanoparticles may be used to facilitate the desired growth, owing to the difference in stability of the cubic and hexagonal phases. Thus, we extended the studies to include cubic phase $NaYF_4:Yb^{3+}/Er^{3+}$ nanoparticles synthesized *via* thermal decomposition (section 3.4). It is well documented that the hexagonal phase lanthanide-doped nanoparticles are more thermodynamically stable as compared to their cubic counterpart,[66,67] thus in order to investigate the phase dependence towards post synthesis growth, cubic phase nanoparticles were studied. In the initial stage investigation, different sizes of cubic phase $NaYF_4:Yb^{3+}/Er^{3+}$ nanoparticles were prepared (see section 3.3 for characterization). This approach was explored because it is well-documented that the surface energy of the nanoparticles increases with decreasing size, which could help to facilitate the post synthesis growth process.[7] Three different sizes of cubic phase nanoparticles were synthesized (61 ± 5 nm, 44 ± 4 nm, and 24 ± 3 nm), and subjected to ligand exchange with KOH as the base because of the changes observed previously (figure 4.12). Unfortunately, in all of the experiments with different sizes of cubic phase nanoparticles, a minimal change in size was observed, with a slight difference in the morphology of the nanoparticles (table. 4.4).

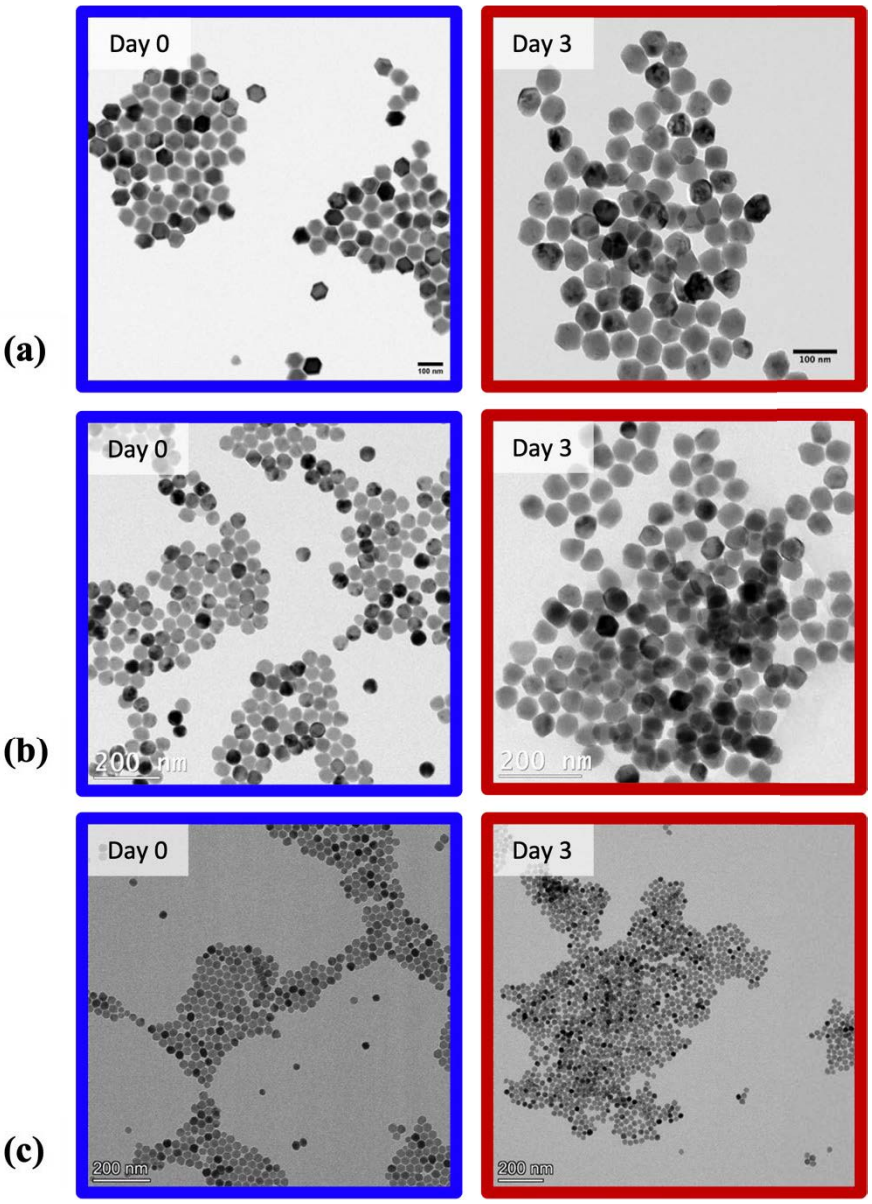

Figure 4. 12. Transmission electron microscopy images of cubic phase $NaYF_4:Yb^{3+}/Er^{3+}$ nanoparticles with different sizes subjected to ligand exchange in the presence of KOH, (a) size 61 ± 5 nm on day 0 (blue), 58 ± 5 nm on day 3 (red); (b) 44 ± 4 nm on day 0 (blue),40 ± 4 nm on day 3 (red); (c) 24 ± 3 nm in size on day 0, 20 ± 2 nm on day 3.

Section no	Composition	Synthesis method	Crystal phase	Base used	Size (day 0) nm	Size (day 3) nm
3.4	$NaYF_4:Yb^{3+}/Er^{3+}$	Thermal decomposition	cubic	KOH	61 ± 5	58 ± 5
3.4	$NaYF_4:Yb^{3+}/Er^{3+}$	Thermal decomposition	cubic	KOH	44 ± 4	40 ± 3
3.4	$NaYF_4:Yb^{3+}/Er^{3+}$	Thermal decomposition	cubic	KOH	24 ± 3	20 ± 2

Table 4. 4. Shows the mean particle size of the cubic phase nanoparticles with different sizes on day 0 and day 3 with KOH in the presence of AL238B ligand.

4.4.2 Effects on the photophysical properties of nanoparticles with AL238B in presence of different bases

Throughout the previously discussed studies, a slight decrease was seen in the size of the nanoparticles when NaOH, and KOH was used as a base, to fully monitor the effect of group 1A base we incorporated RbOH later on in this study. It is very well documented in the literature that lanthanide-doped nanoparticles can undergo dissolution in aqueous media.[68] Thus, it was postulated that while growth was not occurring, perhaps dissolution was. In order to assess if a correlation exists between the decreasing size of nanoparticles with base in presence of AL238B and EDTMP, two approaches were used. Firstly, the upconversion luminescence was recorded in the presence of different bases as a function of time. Secondly, ICP-MS studies were conducted on nanoparticles after 0, 5 and 10 days of incubation to quantify possible changes in ion concentrations in the nanoparticles and solvent that could be indicative of nanoparticle dissolution.

4.4.2.1 Cubic phase $NaYF_4:Yb^{3+}/Er^{3+}$

Cubic phase nanoparticles synthesized by thermal decomposition with a size of 24 ± 3 nm were subjected to different bases: NaOH, KOH and RbOH, during ligand exchange using AL238B as outlined in section 2.3. Transmission electron microscopy analysis of the all the samples were conducted for determining the static size of these nanoparticles, and to observe if the particles underwent any morphological changes or growth. The static size of the nanoparticles with the bases, are shown in table 4.5. As expected, a reduction in nanoparticle size was observed in all cases.

Section no	Composition	Synthesis method	Crystal phase	Base used	Size (day 0) nm	Size (day 3) nm
3.4	$NaYF_4:Yb^{3+}/Er^{3+}$	Thermal decomposition	cubic	NaOH	24 ± 3	19 ± 2
3.4	$NaYF_4:Yb^{3+}/Er^{3+}$	Thermal decomposition	cubic	KOH	24 ± 3	20 ± 2
3.4	$NaYF_4:Yb^{3+}/Er^{3+}$	Thermal decomposition	cubic	RbOH	24 ± 3	21 ± 2

Table 4. 5. Shows the particle size of cubic phase nanoparticles with different bases used to modulate the pH.

Upon examining the TEM images on day 3, we observed a slight decrease in the size of nanoparticles, which were later on examined via spectroscopy. Since it is well-known that the luminescence properties of upconverting nanoparticles vary drastically with size and ion concentration, upconversion emission spectroscopy upon 980 nm excitation was performed to assess if a change in luminescence could be observed that might aid in explaining the observed changes in size. The colloidal solution of the nanoparticles were directly probed using 980 nm excitation, and the upconversion luminescence was measured for all three samples, without any

changes in parameters or existing conditions. The upconversion emission spectra are shown in Figure 4.13. In all cases, the overall emission intensities for all transitions decreased as a function of time, and were undetectable after 5 days. The decrease in the $^{2}H_{11/2}$, $^{4}S_{3/2} \rightarrow {}^{4}I_{15/2}$ and $^{4}F_{9/2} \rightarrow {}^{4}I_{15/2}$ emissions likely stems from the accumulation of surface defects. The surface defects, in combination with the presence of OH^- ions and water, enhance the rate of non-radiative relaxation of Er^{3+} and Yb^{3+} by bridging the energy gaps separating the various transitions.[69]

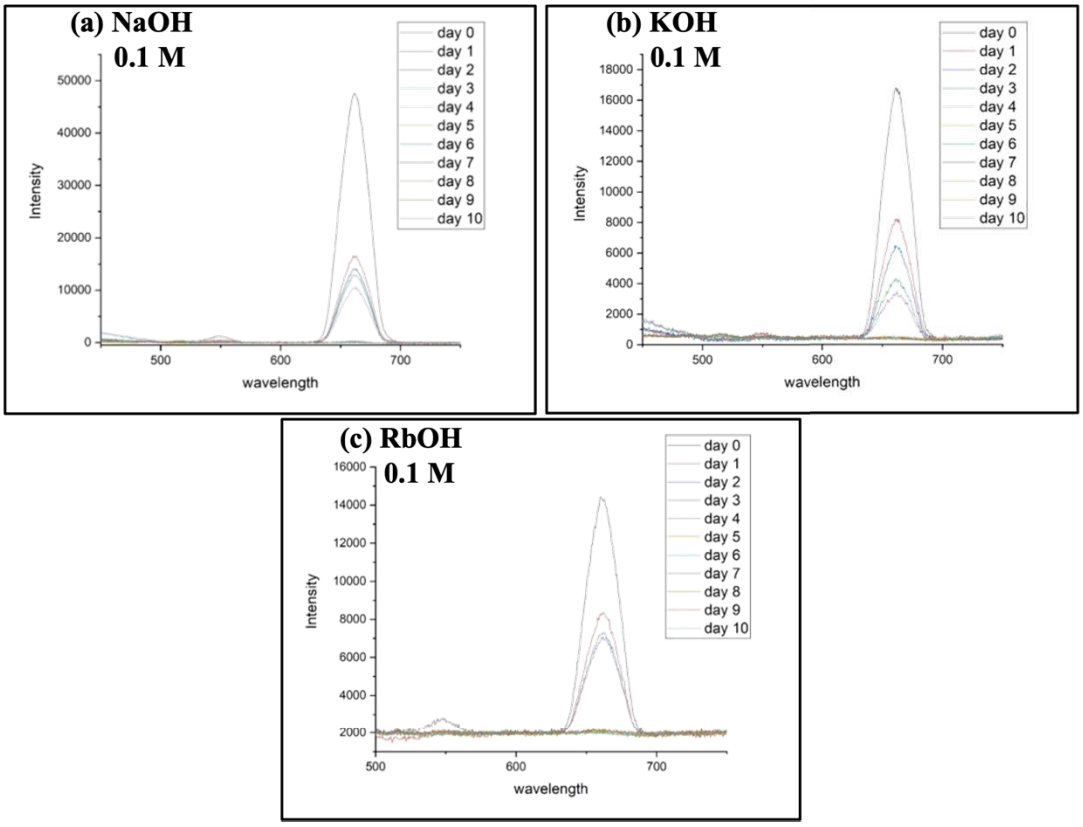

Figure 4. 13. Shows the emission intensity of the cubic phase $NaYF_4:Yb^{3+}/Er^{3+}$ nanoparticles with increasing number of days; (a) NaOH, (b) KOH, and (c) RbOH.

The sudden decrease in the emission intensity from the nanoparticles from day 5 to day 6, suggests that the nanoparticles are undergoing dissolution, which hinders the energy transfer process from the activator to the sensitizer ion. Further analysis of ICP-MS data reveals the

the disintegration of the nanoparticles in the solution, which can be very well reflected back to decrease in the emission intensity of the nanoparticles.

4.4.2.2 Hexagonal phase $NaYF_4:Yb^{3+}/Er^{3+}$and $NaGdF_4:Yb^{3+}/Er^{3+}$

To investigate if the decrease in the emission intensity with different bases is a crystal phase dependence phenomenon, we conducted a similar set of experiments with hexagonal phase $NaYF_4:Yb^{3+}/Er^{3+}$ and $NaGdF_4:Yb^{3+}/Er^{3+}$ nanoparticles. Both the nanocomposites were investigated with different bases: NaOH, KOH, and RbOH. TEM analysis were performed on the particles on day 10 to calculate the static size of the nanoparticles, and to investigate if the particles have gone through size or morphological change. Upon evaluation of TEM images on day 10 no change in the morphology was observed; nevertheless, the same observation was observed as we have reported with cubic phase nanoparticles, the particle size showed a very minimal decrease which is shown in table 4.6 for both the nanoparticles.

Section no	composition	Synthesis method	Crystal phase	Base used	Size (day 0) nm	Size (day 3) nm
3.2	$NaYF_4:Yb^{3+}/Er^{3+}$	Thermal decomposition	hexagonal	NaOH	27 ± 2	25 ± 3
3.2	$NaYF_4:Yb^{3+}/Er^{3+}$	Thermal decomposition	hexagonal	KOH	27 ± 2	24 ± 2
3.2	$NaYF_4:Yb^{3+}/Er^{3+}$	Thermal decomposition	hexagonal	RbOH	27 ± 2	26 ± 2
3.4	$NaGdF_4:Yb^{3+}/Er^{3+}$	Thermal decomposition	hexagonal	NaOH	10 ± 2	9 ± 2
3.4	$NaGdF_4:Yb^{3+}/Er^{3+}$	Thermal decomposition	hexagonal	KOH	10 ± 2	8 ± 3
3.4	$NaGdF_4:Yb^{3+}/Er^{3+}$	Thermal decomposition	hexagonal	RbOH	10 ± 2	10 ± 3

Table 4. 6. Shows the mean particle size of $NaYF_4:Yb^{3+}/Er^{3+}$ and of $NaGdF_4:Yb^{3+}/Er^{3+}$ synthesized by thermal decomposition subjected to ligand exchange with AL238B in the presence of NaOH, KOH, and RbOH.

The upconversion luminescence spectra were recorded for both hexagonal phase $NaYF_4$: Yb^{3+}/Er^{3+} and $NaGdF_4$: Yb^{3+}/Er^{3+} nanoparticles. The upconversion emission spectra are shown in figure 4.14 and 4.15. $NaYF_4$:Yb^{3+}/Er^{3+} and $NaGdF_4$:Yb^{3+}/Er^{3+} nanoparticles exhibited a decrease in the $^2H_{11/2}$, $^4S_{3/2} \rightarrow {}^4I_{15/2}$ and $^4F_{9/2} \rightarrow {}^4I_{15/2}$ emission intensity with progressing number of days, but unlike the cubic phase, the overall emission intensity was still detectable after 10 days. These results provide strong evidence towards the stability of the hexagonal crystal phase over the cubic crystal phase of lanthanide doped nanoparticles.

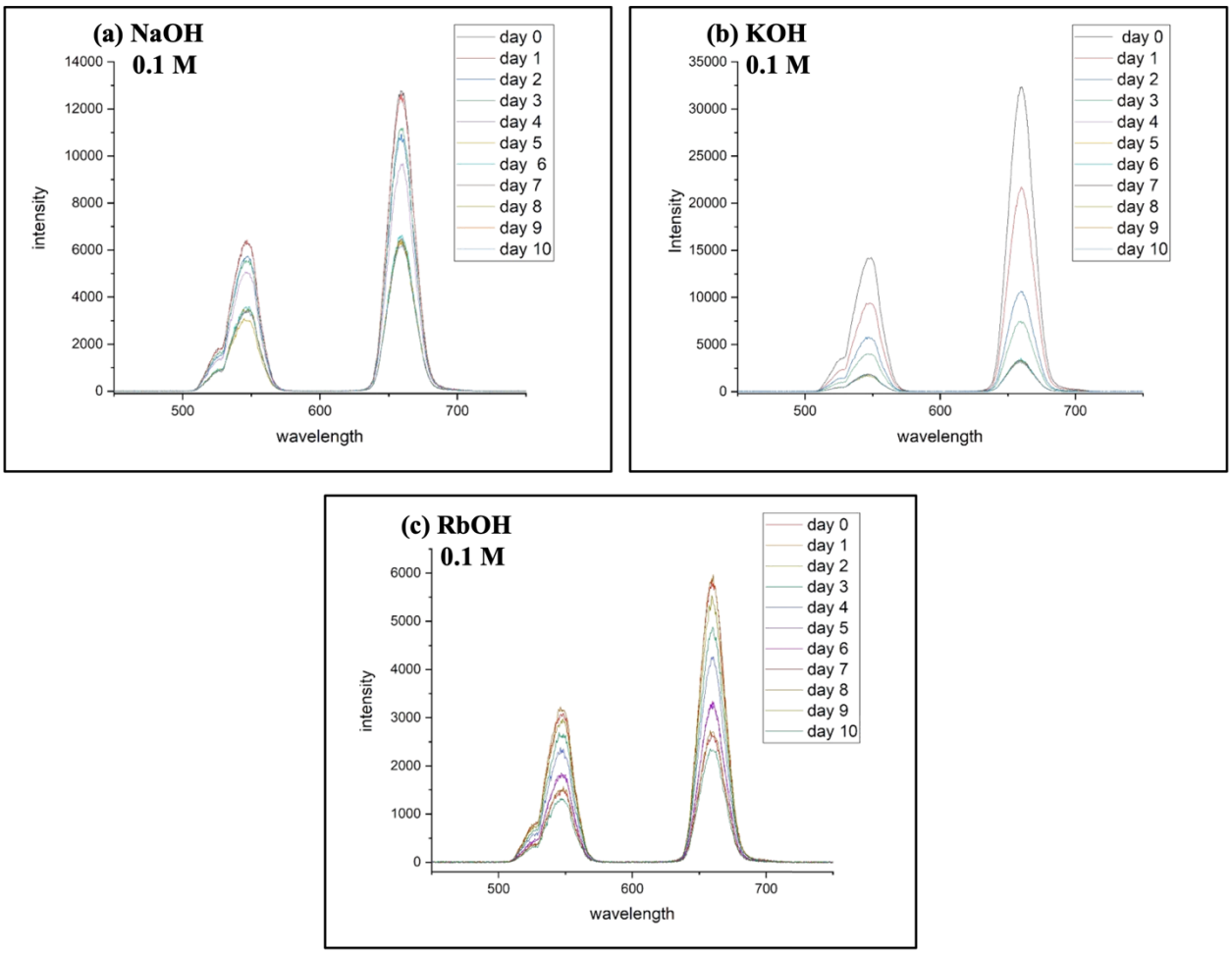

Figure 4. 14. Shows the emission intensity of hexagonal phase $NaYF_4$:Yb^{3+}/Er^{3+} synthesized via thermal decomposition nanoparticles with increasing number of days; (a) NaOH, (b) KOH, and (c) RbOH.

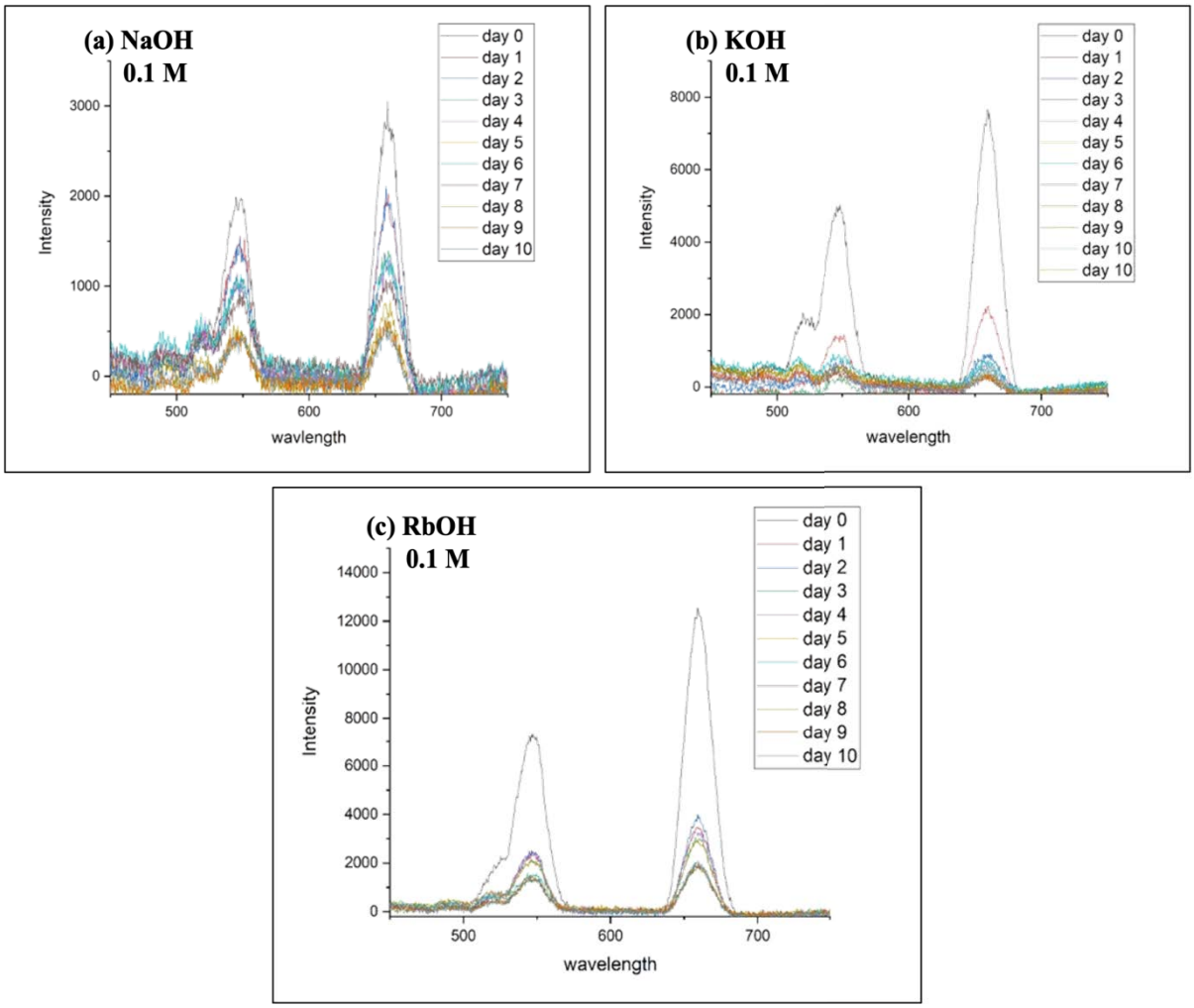

Figure 4. 15. Shows the emission intensity of hexagonal phase $NaGdF_4:Yb^{3+}/Er^{3+}$ synthesized via thermal decomposition nanoparticles with increasing number of days; (a) NaOH, (b) KOH, and (c) RbOH.

4.4.2.3 Time-dependent ICP-MS studies of $NaYF_4:Yb^{3+}/Er^{3+}$ and $NaGdF_4:Yb^{3+}/Er^{3}$ nanoparticles

ICP-MS was carried out in tandem with the luminescence studies to try and corroborate the observed luminescence changes with changes in ion concentrations in the solution and the nanoparticles. To carry out this analysis, aliquots of the nanoparticle dispersion were collected at various time points, and the dispersion was centrifuged multiple times to ensure the separation of the nanoparticles from the supernatant. A portion of the supernatant and pellet were then prepared for ICP-MS analysis as outlined in section 2.4.5 and the difference in total lanthanide ion concentrations (Y^{3+} or Gd^{3+}, Yb^{3+}, Er^{3+}) in the pellets and supernatant were analyzed as a function of time. The data shows a gradual increase in the overall lanthanide concentration in the supernatant, and a concurrent gradual decrease in the lanthanide concentration in the nanoparticle pellet in all the cases. Thus, can be concluded that in the case of the cubic phase nanoparticles, dissolution occurred and, despite this, subsequent growth was not observed. These results are in good agreement with the literature studies where ligands that are able to form complexes with ligands, can facilitate the disintegration of the nanoparticles.[46] A summary of lanthanide concentrations with different bases in nanoparticles and supernatant is shown in table 4.7.

Cubic phase $NaYF_4:Yb^{3+}/Er^{3+}$ with NaOH	**Day 0**	**Day 5**	**Day 10**
% lanthanides in Pellet	90.7	81.0	63.3
% lanthanide in supernatant	9.3	19.0	36.7

Cubic phase $NaYF_4:Yb^{3+}/Er^{3+}$ with KOH	**Day 0**	**Day 5**	**Day 10**
% lanthanides in Pellet	89.5	81.3	66.5
% lanthanide in supernatant	10.5	18.7	33.5

Cubic phase $NaYF_4:Yb^{3+}/Er^{3+}$ with RbOH	Day 0	Day 5	Day 10
% lanthanides in Pellet	89.7	79.9	67.9
% lanthanide in supernatant	10.3	20.1	32.1

Table 4. 7. Illustrate the ICP-MS data of % lanthanide composition of cubic phase $NaYF_4:Yb^{3+}/Er^{3+}$ nanoparticles in pellet and supernatant on day 0, 5 and 10

Further analysis of ICP-MS data for hexagonal phase nanoparticles reveals the disintegration of the nanoparticles in the solution is shown in table 4.8 (a and b). The data shows a similar trend as observed with the cubic phase nanoparticles; although, the increase in lanthanide concentration in the supernatant was not as pronounced as was seen in the case of cubic phase nanoparticles. This finding is in agreement with the known increased stability of the hexagonal phase nanoparticles.

Hexagonal phase $NaYF_4:Yb^{3+}/Er^{3+}$ with NaOH	Day 0	Day 5	Day 10
% lanthanides in Pellet	90.5	85.0	80.0
% lanthanide in supernatant	9.4	15.0	20.0

Hexagonal phase $NaYF_4:Yb^{3+}/Er^{3+}$ with KOH	Day 0	Day 5	Day 10
% lanthanides in Pellet	89.6	86.6	81.3
% lanthanide in supernatant	10.4	13.4	18.7

Hexagonal phase $NaYF_4:Yb^{3+}/Er^{3+}$ with RbOH	Day 0	Day 5	Day 10
% lanthanides in Pellet	90.0	88.5	83.0
% lanthanide in supernatant	10.0	11.5	17.0

(a)

Hexagonal phase $NaGdF_4$:Yb^{3+}/Er^{3+} NP with NaOH	**Day 0**	**Day 5**	**Day 10**
% lanthanides in Pellet	97.6	94.4	90.8
% lanthanide in supernatant	2.3	5.6	9.2

Hexagonal phase $NaGdF_4$:Yb^{3+}/Er^{3+} NP with KOH	**Day 0**	**Day 5**	**Day 10**
% lanthanides in Pellet	96.7	81.3	93.7
% lanthanide in supernatant	3.2	18.7	6.28

Hexagonal phase $NaGdF_4$:Yb^{3+}/Er^{3+} NP with RbOH	**Day 0**	**Day 5**	**Day 10**
% lanthanides in Pellet	96.2	94.9	93.4
% lanthanide in supernatant	3.82	5.1	6.6

(b)

Table 4. 8. Illustrate the ICP-MS data of % lanthanide composition of Hexagonal phase (a) $NaYF_4$:Yb^{3+}/Er^{3+} and (b) $NaGdF_4$:Yb^{3+}/Er^{3+}nanoparticles in pellet and supernatant on day 0, 5 and 10.

Chapter 5- Conclusion

The interest towards the surface of the lanthanide doped nanoparticles is of great curiosity because of the potential it holds. The combined use of the difference in the surface energy of defined crystal planes and the affinity of the ligands towards the surface, have led the path for modulating the morphology and size along specific direction for scientific and industrial applications. However, there is a lot to be investigated towards the stability of the nanoparticles, once they have been synthesized and subjected to ligand exchange, and incubated in various media.

The thermal decomposition was used to prepare hexagonal and cubic phase $NaYF_4:Yb^{3+}/Er^{3+}$, and hexagonal phase $NaGdF_4:Yb^{3+}/Er^{3+}$. In addition to that, the coprecipitation technique was used to synthesize hexagonal $NaYF_4:Yb^{3+}/Er^{3+}$. Both the synthesizes method produced monodispersed, pure phase nanoparticles with sizes ranging between 10-40nm. The as-synthesized nanoparticles possessed a hydrophobic coating of oleic acid, consequently surface modification was carried out to remove the hydrophobic ligand, by using EDTMP or AL238B which show higher affinity towards the positively charged surface of lanthanide doped nanoparticles, and thus making them disperse in aqueous media.

The synthesis of ligand AL238B, was achieved through a 5 step synthetic route with the highest purity, which was isolated and characterized using techniques such as NMR, and LC-MS, and has been used in understanding the post synthesis growth of the lanthanide based upconverting nanoparticles.

The use of multidentate phosphonate type ligand for inducing post synthesis growth of the lanthanide doped nanoparticles was investigated for the first time. The strategy used in this work focuses on using multidentate phosphonate ligands, due to their peculiar affinity towards the surface of the nanoparticles. The findings suggest that the factors such as the synthesis method, and crystal phases have a crucial role in monitoring the growth of the nanoparticles. Despite the fact that there were cases where we saw the growth and necking of nanoparticles suggesting Ostwald ripening, and oriented attachment, we were not able to reproduce those results. However, our research has demonstrated that irrespective of the synthesis method, nanoparticle composition, crystal phase and the base used for modulating the pH we observed a decrease in the size of the nanoparticles. The luminescence intensity of the nanoparticles over a period of 10 days showed a gradual decrease in all the cases, with about more than 50% decrease in the emission intensity, within the period of 5 days. Furthermore, the increase in the lanthanide concentration in the supernatant corroborates the dissolution of the nanoparticles.

These findings add to a growing body of literature on understanding the surface chemistry of the lanthanide doped nanoparticles with phosphonate type ligands. Sequentially, this may bring us one step closer in order to understanding the surface of these fascinating nanoparticles.

Chapter 6- Future work

This research has raised many questions regarding the stability of nanoparticles with multidentate phosphonate type ligands in basic media, which needs further investigation. More in-depth studies on the current topic of post synthesis growth or the disintegration of the nanoparticles need to be carried out in order to understand the fundamentals of the surface dynamics governing the disintegration or growth of the lanthanide doped nanoparticles.

Future work should seek to establish whether the size of the nanoparticles plays a crucial role in observing post synthesis growth. The synthesis of ultra-small nanoparticles in the size range of 5-10 nm, and using them to study the post synthesis growth with multidentate phosphonate type ligand would be a good starting point. As mentioned previously, as size decreases, the surface energy of the nanoparticles increases, thus having nanoparticles in the ultra-small size range will be fundamental for future work. Moreover, the relation between leaching of lanthanides from the host material ($NaYF_4$, and $NaGdF_4$) with respect to the size of the nanoparticles can lead to the understanding of the fundamentals of surface chemistry in lanthanide doped nanoparticles.

Furthermore, while this work was only focused upon using multidentate phosphonate based ligand, the inclusion of bidentate, and tridentate phosphonate type ligands and their effect either on the growth or the disintegration of the nanoparticles will be an important step in the right direction, to postulate a relationship between the chelating arms of the ligands and the surface of the lanthanide doped nanoparticles, which has never been reported before.

It would be also important to perform core-shell studies with different shell thicknesses on these nanoparticles. The use of an inert shell will protect the core of the nanoparticles from the external environment, and the use of different shell thicknesses can provide insight regarding the disintegration of the nanoparticles. The work would be carried by recording upconversion intensity every day, and to record changes on each day with particles having varying shell thickness. Our results have shown that the nanoparticles emission goes through a substantial decrease, and in order to understand the possible reasons for this decrease, a systematic study needs to be carried out.

References

(1) Wu, A. R.; Yu, L. There's Plenty of Room at the Bottom of a Cell. *Chem. Eng. Prog.* **2017**, *113* (10).

(2) Hunt, W. H. Nanomaterials : Nomenclature , Novelty , and Necessity. 13–18.

(3) Drexler, K. E. *Engines of Creation: The Coming Era of Nanotechnology*; Doubleday, 1986.

(4) Whatmore, R. W. Nanotechnology - What Is It? Should We Be Worried? *Occup. Med. (Chic. Ill).* **2006**, *56* (5), 295–299. https://doi.org/10.1093/occmed/kql050.

(5) ISO/TS 80004-2:2015(en) Nanotechnologies — Vocabulary — Part 2: Nano-objects https://www.iso.org/obp/ui/#iso:std:iso:ts:80004:-2:ed-1:v1:en (accessed Jul 28, 2020).

(6) Gnach, A.; Lipinski, T.; Bednarkiewicz, A.; Rybka, J.; Capobianco, J. A. Upconverting Nanoparticles: Assessing the Toxicity. *Chem. Soc. Rev.* **2015**, *44* (6), 1561–1584. https://doi.org/10.1039/c4cs00177j.

(7) Naccache, R.; Yu, Q.; Capobianco, J. A. The Fluoride Host: Nucleation, Growth, and Upconversion of Lanthanide-Doped Nanoparticles. *Adv. Opt. Mater.* **2015**, *3* (4), 482–509. https://doi.org/10.1002/adom.201400628.

(8) Iqbal, P.; Preece, J. A.; Mendes, P. M. Nanotechnology: The "Top-Down" and "Bottom-Up" Approaches. *Supramol. Chem.* **2012**. https://doi.org/10.1002/9780470661345.smc195.

(9) Fang, F. Z.; Zhang, X. D.; Gao, W.; Guo, Y. B.; Byrne, G.; Hansen, H. N. CIRP Annals - Manufacturing Technology Nanomanufacturing — Perspective and Applications. *CIRP Ann. - Manuf. Technol.* **2017**, *66* (2), 683–705. https://doi.org/10.1016/j.cirp.2017.05.004.

(10) Mijatovic, D.; Eijkel, J. C. T.; Van Den Berg, A. Technologies for Nanofluidic Systems:

Top-down vs. Bottom-up - A Review. *Lab Chip* **2005**, *5* (5), 492–500. https://doi.org/10.1039/b416951d.

(11) Ashley, J. F.; Cramer, N. B.; Davis, R. H.; Bowman, C. N. Soft-Lithography Fabrication of Microfluidic Features Using Thiol-Ene Formulations. *Lab Chip* **2011**, *11* (16), 2772–2778. https://doi.org/10.1039/c1lc20189a.

(12) Gates, B. D.; Xu, Q.; Stewart, M.; Ryan, D.; Willson, C. G.; Whitesides, G. M. New Approaches to Nanofabrication: Molding, Printing, and Other Techniques. *Chem. Rev.* **2005**, *105* (4), 1171–1196. https://doi.org/10.1021/cr030076o.

(13) Yu, H. D.; Regulacio, M. D.; Ye, E.; Han, M. Y. Chemical Routes to Top-down Nanofabrication. *Chem. Soc. Rev.* **2013**, *42* (14), 6006–6018. https://doi.org/10.1039/c3cs60113g.

(14) Zhang, J.; Chaker, M.; Ma, D. Pulsed Laser Ablation Based Synthesis of Colloidal Metal Nanoparticles for Catalytic Applications. *J. Colloid Interface Sci.* **2017**, *489*, 138–149. https://doi.org/10.1016/j.jcis.2016.07.050.

(15) El-Khatib, A. M.; Badawi, M. S.; Ghatass, Z. F.; Mohamed, M. M.; Elkhatib, M. Synthesize of Silver Nanoparticles by Arc Discharge Method Using Two Different Rotational Electrode Shapes. *J. Clust. Sci.* **2018**, *29* (6), 1169–1175. https://doi.org/10.1007/s10876-018-1430-2.

(16) Huie, J. C. Guided Molecular Self-Assembly: A Review of Recent Efforts. *Smart Mater. Struct.* **2003**, *12* (2), 264–271. https://doi.org/10.1088/0964-1726/12/2/315.

(17) Grzelczak, M.; Vermant, J.; Furst, E. M.; Liz-Marzán, L. M. Directed Self-Assembly of Nanoparticles. *ACS Nano* **2010**, *4* (7), 3591–3605. https://doi.org/10.1021/nn100869j.

(18) Wells, W. H.; Wells, V. L. The Lanthanides, Rare Earth Elements. *Patty's Toxicol.* **2012**,

1, 817–840. https://doi.org/10.1002/0471435139.tox043.pub2.

(19) Whynne-Hammond, C. *Elements of Human Geography*, 2nd Ed.; Unwin Hyman: London, 1985.

(20) Hüfner, S. *Optical Spectra of Transparent Rare Earth Compounds*; Academic Press: New York, 1978.

(21) Pekka Hänninen, H. H. *Lanthanide Luminescence: Photophysical, Analytical and Biological Aspects*; Springer: Heidelberg, Germany, 2010. https://doi.org/10.1007/4243_2010_3.

(22) Auzel, F. Upconversion and Anti-Stokes Processes with f and d Ions in Solids. *Chem. Rev.* **2004**, *104* (1), 139–173. https://doi.org/10.1021/cr020357g.

(23) Ding, M.; Chen, D. *Lanthanide Ions Doped Upconversion Nanomaterials: Synthesis, Surface Engineering, and Application in Drug Delivery*; Elsevier Inc., 2016. https://doi.org/10.1016/B978-0-323-47347-7.00009-4.

(24) Ovsyakin, V. V., and P. P. F. Cooperative Sensitization of Luminescence in Crystals Activated with Rare Earth Ions. *Phys. JETPL lett* **1966**, *4*, 317.

(25) Dong, H.; Sun, L. D.; Yan, C. H. Energy Transfer in Lanthanide Upconversion Studies for Extended Optical Applications. *Chem. Soc. Rev.* **2015**, *44* (6), 1608–1634. https://doi.org/10.1039/c4cs00188e.

(26) Menyuk, N.; Dwight, K.; Pierce, J. W. NaYF4: Yb,Er - An Efficient Upconversion Phosphor. *Appl. Phys. Lett.* **1972**, *21* (4), 159–161. https://doi.org/10.1063/1.1654325.

(27) Haase, M.; Schäfer, H. Upconverting Nanoparticles. *Angew. Chemie - Int. Ed.* **2011**, *50* (26), 5808–5829. https://doi.org/10.1002/anie.201005159.

(28) Wang, F.; Han, Y.; Lim, C. S.; Lu, Y.; Wang, J.; Xu, J.; Chen, H.; Zhang, C.; Hong, M.;

Liu, X. Simultaneous Phase and Size Control of Upconversion Nanocrystals through Lanthanide Doping. *Nature* **2010**, *463* (7284), 1061–1065. https://doi.org/10.1038/nature08777.

(29) Chen, G.; Liang, H.; Liu, H.; Somesfalean, G.; Zhang, Z. Near Vacuum Ultraviolet Luminescence of Gd^3+ and Er^3+ Ions Generated by Super Saturation Upconversion Processes. *Opt. Express* **2009**, *17* (19), 16366. https://doi.org/10.1364/oe.17.016366.

(30) Thanh, N. T. K.; Maclean, N.; Mahiddine, S. Mechanisms of Nucleation and Growth of Nanoparticles in Solution. *Chem. Rev.* **2014**, *114* (15), 7610–7630. https://doi.org/10.1021/cr400544s.

(31) LAMER, V. K.; DINEGAR, R. H. Theory, Production and Mechanism of Formation of Monodispersed Hydrosols. *J. Am. Chem. Soc.* **1950**, *72* (11), 4847–4854.

(32) Lee, J.; Yang, J.; Kwon, S. G.; Hyeon, T. Nonclassical Nucleation and Growth of Inorganic Nanoparticles. *Nat. Rev. Mater.* **2016**, *1* (8). https://doi.org/10.1038/natrevmats.2016.34.

(33) You, H.; Fang, J. Particle-Mediated Nucleation and Growth of Solution-Synthesized Metal Nanocrystals: A New Story beyond the LaMer Curve. *Nano Today* **2016**, *11* (2), 145–167. https://doi.org/10.1016/j.nantod.2016.04.003.

(34) Noorduin, W. L.; Vlieg, E.; Kellogg, R. M.; Kaptein, B. From Ostwald Ripening to Single Chirality. *Angew. Chemie - Int. Ed.* **2009**, *48* (51), 9600–9606. https://doi.org/10.1002/anie.200905215.

(35) Mixtures, T. TWO-PHASE MIXTURES. **1992**, 197–215.

(36) Salzmann, B. B. V.; Van Der Sluijs, M. M.; Soligno, G.; Vanmaekelbergh, D. Oriented Attachment: From Natural Crystal Growth to a Materials Engineering Tool. *Acc. Chem.*

Res. **2021**, *54* (4), 787–797. https://doi.org/10.1021/acs.accounts.0c00739.

(37) Liu, D.; Xu, X.; Du, Y.; Qin, X.; Zhang, Y.; Ma, C.; Wen, S.; Ren, W.; Goldys, E. M.; Piper, J. A.; Dou, S.; Liu, X.; Jin, D. Three-Dimensional Controlled Growth of Monodisperse Sub-50 Nm Heterogeneous Nanocrystals. *Nat. Commun.* **2016**, *7*, 1–8. https://doi.org/10.1038/ncomms10254.

(38) Ma, Fei, X. K. Using Dangling Bond Density to Characterize the Surfaceenergy of Nanomaterials. *Surf. Interface Anal.* **2007**, *39* (c), 611–614. https://doi.org/10.1002/sia.2562.

(39) Bogdan, N.; Vetrone, F.; Ozin, G. A.; Capobianco, J. A. Synthesis of Ligand-Free Colloidally Stable Water Dispersible Brightly Luminescent Lanthanide-Doped Upconverting Nanoparticles. *Nano Lett.* **2011**, *11* (2), 835–840. https://doi.org/10.1021/nl1041929.

(40) Dong, A.; Ye, X.; Chen, J.; Kang, Y.; Gordon, T.; Kikkawa, J. M.; Murray, C. B. A Generalized Ligand-Exchange Strategy Enabling Sequential Surface Functionalization of Colloidal Nanocrystals. *J. Am. Chem. Soc.* **2011**, *133* (4), 998–1006. https://doi.org/10.1021/jal08948z.

(41) Heuer-Jungemann, A.; Feliu, N.; Bakaimi, I.; Hamaly, M.; Alkilany, A.; Chakraborty, I.; Masood, A.; Casula, M. F.; Kostopoulou, A.; Oh, E.; Susumu, K.; Stewart, M. H.; Medintz, I. L.; Stratakis, E.; Parak, W. J.; Kanaras, A. G. The Role of Ligands in the Chemical Synthesis and Applications of Inorganic Nanoparticles. *Chem. Rev.* **2019**, *119* (8), 4819–4880. https://doi.org/10.1021/acs.chemrev.8b00733.

(42) Duong, H. T. T.; Chen, Y.; Tawfik, S. A.; Wen, S.; Parviz, M.; Shimoni, O.; Ab, D. J. Systematic Investigation of Functional Ligands for Colloidal Stable Upconversion

Nanoparticles†. *RSC Adv.* **2018**, *8* (9), 4842–4849. https://doi.org/10.1039/c7ra13765f.

(43) Chiang, Y.-M.; Birnie, D. P.; Kingery, W. D. *Physical Ceramics: Principles for Ceramic Science and Engineering*; Choice Reviews Online, 1996.

(44) Borm, P.; Klaessig, F. C.; Landry, T. D.; Moudgil, B.; Pauluhn, J.; Thomas, K.; Trottier, R.; Wood, S. Research Strategies for Safety Evaluation of Nanomaterials, Part V: Role of Dissolution in Biological Fate and Effects of Nanoscale Particles. *Toxicol. Sci.* **2006**, *90* (1), 23–32. https://doi.org/10.1093/toxsci/kfj084.

(45) Wu, D.; Wu, X.; Lv, Y.; Wang, H. Influence of Solubility on the Particle Size of Fluorides Crystalline Precipitated from Aqueous Solutions. *Mater. Lett.* **2008**, *62* (17–18), 3003–3006. https://doi.org/10.1016/j.matlet.2008.01.095.

(46) Mioduski, T.; Gumiński, C.; Zeng, D. IUPAC-NIST Solubility Data Series. 100. Rare Earth Metal Fluorides in Water and Aqueous Systems. Part 1. Scandium Group (Sc, Y, La). *J. Phys. Chem. Ref. Data* **2014**, *43* (1). https://doi.org/10.1063/1.4866773.

(47) Lisjak, D.; Plohl, O.; Ponikvar-Svet, M.; Majaron, B. Dissolution of Upconverting Fluoride Nanoparticles in Aqueous Suspensions. *RSC Adv.* **2015**, *5* (35), 27393–27397. https://doi.org/10.1039/c5ra00902b.

(48) Xue, X.; Uechi, S.; Tiwari, R. N.; Duan, Z.; Liao, M.; Yoshimura, M.; Suzuki, T.; Ohishi, Y. Size-Dependent Upconversion Luminescence and Quenching Mechanism of LiYF_4: Er^3+/Yb^3+ Nanocrystals with Oleate Ligand Adsorbed. *Opt. Mater. Express* **2013**, *3* (7), 989. https://doi.org/10.1364/ome.3.000989.

(49) Wang, F.; Wang, J.; Liu, X. Direct Evidence of a Surface Quenching Effect on Size-Dependent Luminescence of Upconversion Nanoparticles. *Angew. Chemie - Int. Ed.* **2010**, *49* (41), 7456–7460. https://doi.org/10.1002/anie.201003959.

(50) Feng, Y.; Li, Z.; Li, Q.; Yuan, J.; Tu, L.; Ning, L.; Zhang, H. Internal OH− Induced Cascade Quenching of Upconversion Luminescence in NaYF4:Yb/Er Nanocrystals. *Light Sci. Appl.* **2021**, *10* (1). https://doi.org/10.1038/s41377-021-00550-5.

(51) Bae, Y.; Lim, K.; Kim, S.; Kang, D.; Kim, B. H.; Kim, J.; Kang, S.; Jeon, S.; Cho, J.; Lee, W. B.; Lee, W. C.; Park, J. Ligand-Dependent Coalescence Behaviors of Gold Nanoparticles Studied by Multichamber Graphene Liquid Cell Transmission Electron Microscopy. *Nano Lett.* **2020**, *20* (12), 8704–8710. https://doi.org/10.1021/acs.nanolett.0c03517.

(52) Wang, Y. Q.; Liang, W. S.; Geng, C. Y. Shape Evolution of Gold Nanoparticles. *J. Nanoparticle Res.* **2010**, *12* (2), 655–661. https://doi.org/10.1007/s11051-009-9612-3.

(53) Arcidiacono, S.; Bieri, N. R.; Poulikakos, D.; Grigoropoulos, C. P. On the Coalescence of Gold Nanoparticles. *Int. J. Multiph. Flow* **2004**, *30* (7-8 SPEC. ISS.), 979–994. https://doi.org/10.1016/j.ijmultiphaseflow.2004.03.006.

(54) José-Yacamán, M.; Gutierrez-Wing, C.; Miki, M.; Yang, D. Q.; Piyakis, K. N.; Sacher, E. Surface Diffusion and Coalescence of Mobile Metal Nanoparticles. *J. Phys. Chem. B* **2005**, *109* (19), 9703–9711. https://doi.org/10.1021/jp0509459.

(55) Guo, P.; Gao, Y. Coalescence of Au Nanoparticles without Ligand Detachment. *Phys. Rev. Lett.* **2020**, *124* (6), 66101. https://doi.org/10.1103/PhysRevLett.124.066101.

(56) Lin, M.; Zhao, Y.; Wang, S. Q.; Liu, M.; Duan, Z. F.; Chen, Y. M.; Li, F.; Xu, F.; Lu, T. J. Recent Advances in Synthesis and Surface Modification of Lanthanide-Doped Upconversion Nanoparticles for Biomedical Applications. *Biotechnol. Adv.* **2012**, *30* (6), 1551–1561. https://doi.org/10.1016/j.biotechadv.2012.04.009.

(57) Loussouarn, A.; Duflos, M.; Benoist, E.; Baut, G. Le. Synthesis of New Bifunctional

Chelating Agents : (1R *, 2R *, 4S *) -4- Ethanephosphonic Acid (4-ICEP) Anthony Loussouarn , a , b Muriel Duflos , b Eric Benoist , a Jean-François Chatal , A. *Synthesis (Stuttg).* **1998**, 237–241.

(58) Abada, S.; Lecointre, A.; Elhabiri, M.; Charbonnière, L. J. Formation of Very Stable and Selective Cu(II) Complexes with a Non-Macrocyclic Ligand: Can Basicity Rival Pre-Organization? *Dalt. Trans.* **2010**, *39* (38), 9055–9062. https://doi.org/10.1039/c0dt00453g.

(59) Liu, C.; Lei, H.; Zhang, Z.; Chen, F.; Cao, R. Oxygen Reduction Catalyzed by a Water-Soluble Binuclear Copper(Ii) Complex from a Neutral Aqueous Solution. *Chem. Commun.* **2017**, *53* (22), 3189–3192. https://doi.org/10.1039/c6cc09206c.

(60) Mu, X. J.; Lei, M. Y.; Zou, J. P.; Zhang, W. Microwave-Assisted Solvent-Free and Catalyst-Free Kabachnik-Fields Reactions for α-Amino Phosphonates. *Tetrahedron Lett.* **2006**, *47* (7), 1125–1127. https://doi.org/10.1016/j.tetlet.2005.12.027.

(61) Abada, S.; Lecointre, A.; Elhabiri, M.; Esteban-Gómez, D.; Platas-Iglesias, C.; Tallec, G.; Mazzanti, M.; Charbonnière, L. J. Highly Relaxing Gadolinium Based MRI Contrast Agents Responsive to Mg2+ Sensing. *Chem. Commun.* **2012**, *48* (34), 4085–4087. https://doi.org/10.1039/c2cc30757j.

(62) Princz, E.; Szilágyi, I.; Mogyorósi, K.; Labádi, I. Lanthanide Complexes of Ethylenediaminotetramethylene-Phosphonic Acid. *J. Therm. Anal. Calorim.* **2002**, *69* (2), 427–439. https://doi.org/10.1023/A:1019943319341.

(63) Jia, F.; Li, G.; Yang, B.; Yu, B.; Shen, Y.; Cong, H. Investigation of Rare Earth Upconversion Fluorescent Nanoparticles in Biomedical Field. *Nanotechnol. Rev.* **2019**, *8* (1), 1–17. https://doi.org/10.1515/ntrev-2019-0001.

(64) Han, S.; Qin, X.; An, Z.; Zhu, Y.; Liang, L.; Han, Y.; Huang, W.; Liu, X. Multicolour Synthesis in Lanthanide-Doped Nanocrystals through Cation Exchange in Water. *Nat. Commun.* **2016**, *7*, 1–7. https://doi.org/10.1038/ncomms13059.

(65) Gentry, S. T.; Kendra, S. F.; Bezpalko, M. W. Ostwald Ripening in Metallic Nanoparticles: Stochastic Kinetics. *J. Phys. Chem. C* **2011**, *115* (26), 12736–12741. https://doi.org/10.1021/jp2009786.

(66) Wang, F.; Han, Y.; Lim, C. S.; Lu, Y.; Wang, J.; Xu, J.; Chen, H.; Zhang, C.; Hong, M.; Liu, X. Simultaneous Phase and Size Control of Upconversion Nanocrystals through Lanthanide Doping. *Nature* **2010**, *463* (7284), 1061–1065. https://doi.org/10.1038/nature08777.

(67) Mai, H. X.; Zhang, Y. W.; Si, R.; Yan, Z. G.; Sun, L. D.; You, L. P.; Yan, C. H. High-Quality Sodium Rare-Earth Fluoride Nanocrystals: Controlled Synthesis and Optical Properties. *J. Am. Chem. Soc.* **2006**, *128* (19), 6426–6436. https://doi.org/10.1021/ja060212h.

(68) Vozlič, M.; Černič, T.; Gyergyek, S.; Majaron, B.; Ponikvar-Svet, M.; Kostiv, U.; Horák, D.; Lisjak, D. Formation of Phosphonate Coatings for Improved Chemical Stability of Upconverting Nanoparticles under Physiological Conditions. *Dalt. Trans.* **2021**, *50* (19), 6588–6597. https://doi.org/10.1039/d1dt00304f.

(69) Tessitore, G.; Mandl, G. A.; Brik, M. G.; Park, W.; Capobianco, J. A. Recent Insights into Upconverting Nanoparticles: Spectroscopy, Modeling, and Routes to Improved Luminescence. *Nanoscale* **2019**, *11* (25), 12015–12029. https://doi.org/10.1039/c9nr02291k.

Appendix I: Supporting information for Chapter 3

Contents **Page**

Supporting figures and schemes:

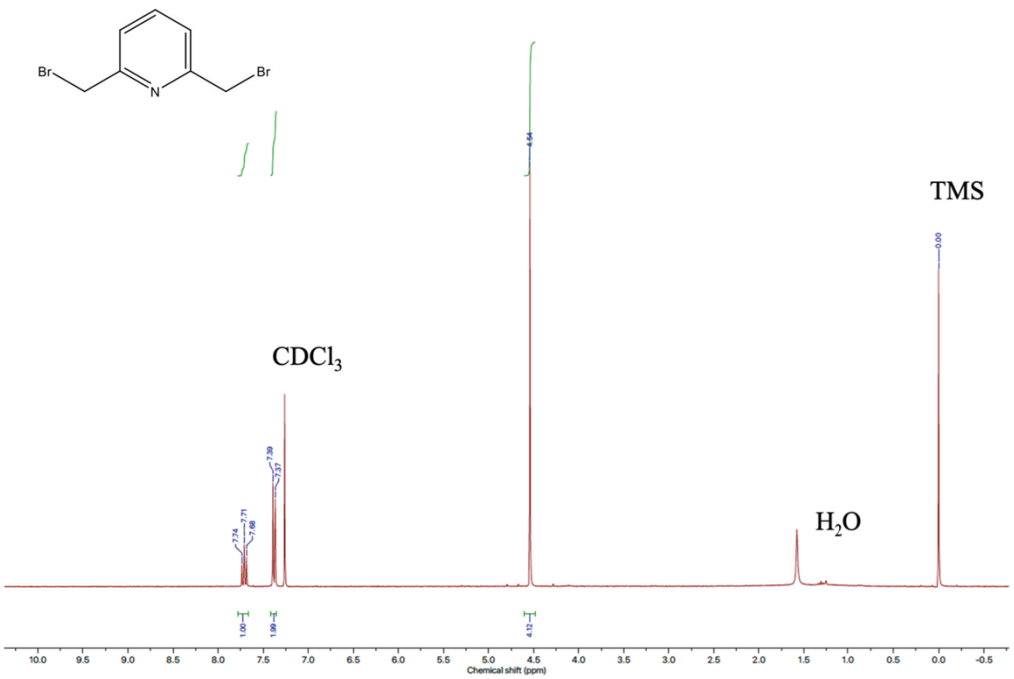

Figure A3.1. 500 MHz 1H NMR spectrum of compound **2** (in $CDCl_3$).

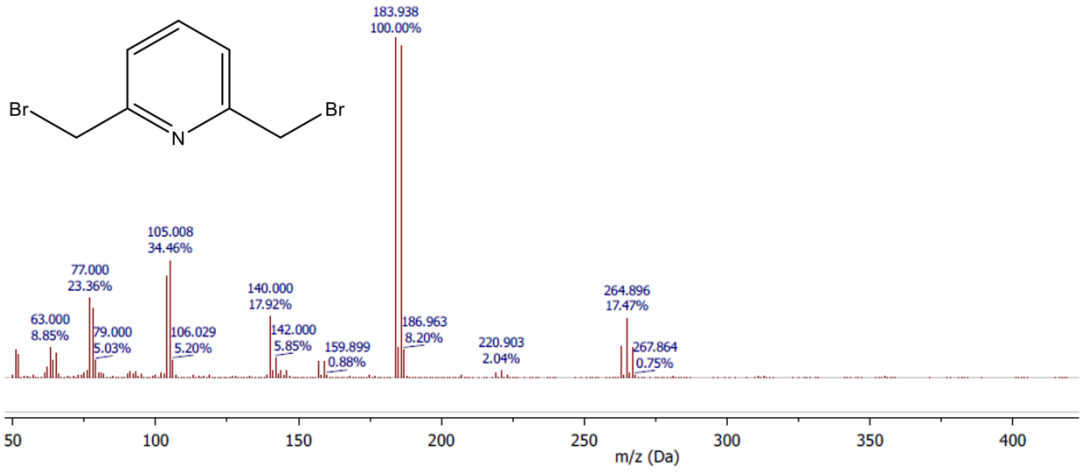

Figure A3.2. GC-MS Spectrum of compound **2** (expected mass: 264.9).

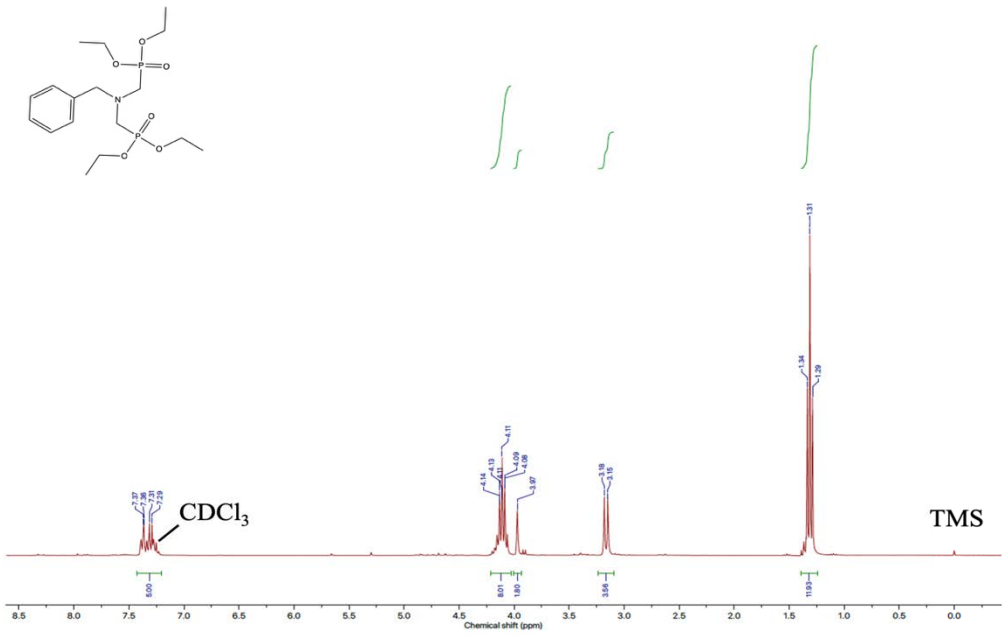

Figure A3.3. 500 MHz 1H NMR spectrum of compound **4** (in $CDCl_3$).

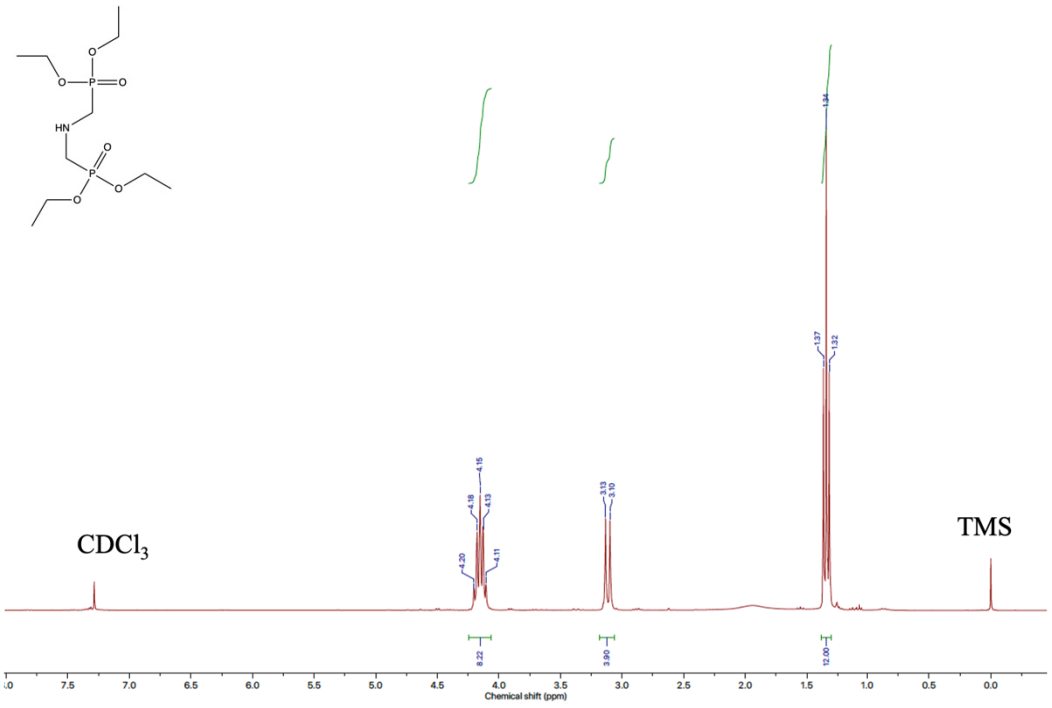

Figure A3.4. 500 MHz ^{1}H NMR spectrum of compound **5** (in CDCl3).

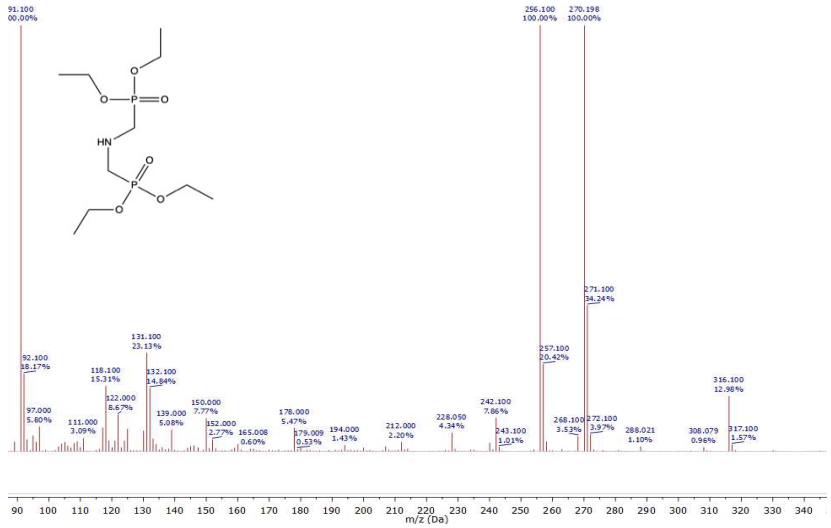

Figure A.3.5. GC-MS Spectrum of compound **5** (expected mass: 317.1)

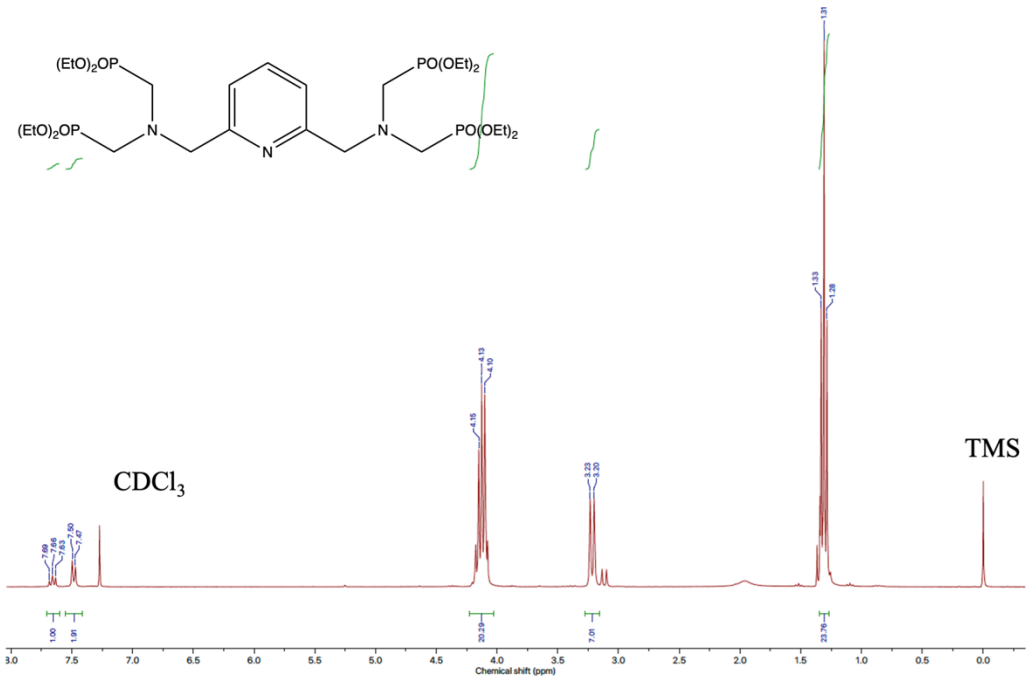

Figure A3.6. 500 MHz ^{1}H NMR spectrum of compound **6** (in $CDCl_3$).

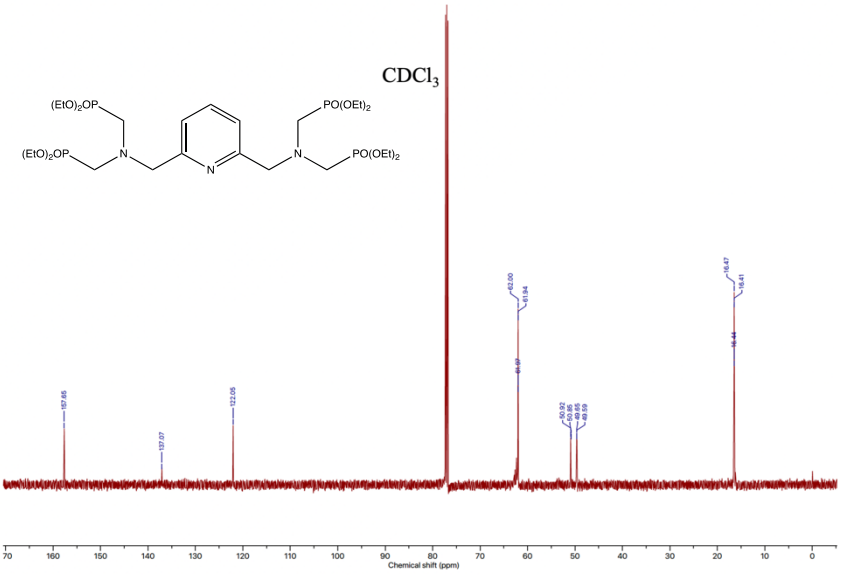

Figure A3.7. 126 MHz ^{13}C NMR spectrum of compound **6** (in $CDCl_3$).

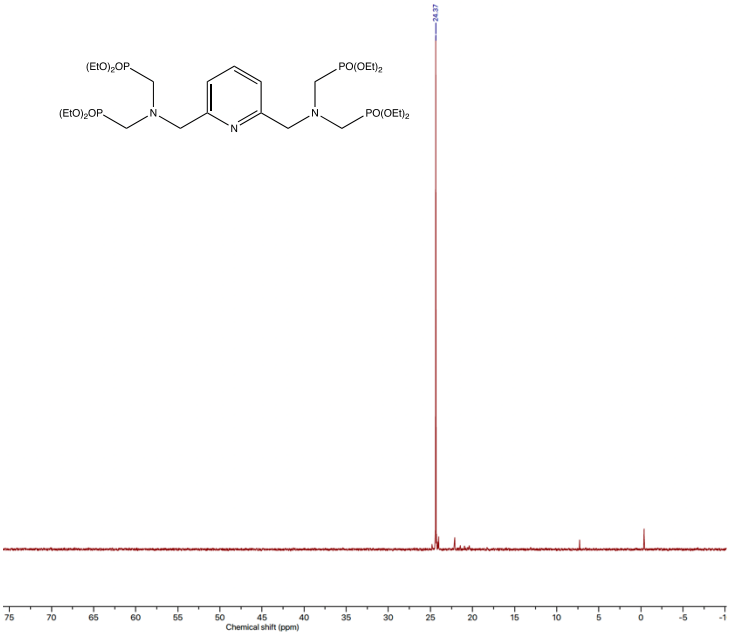

Figure A3.8. 202 MHz ^{31}P NMR spectrum of compound 6 (in $CDCl_3$).

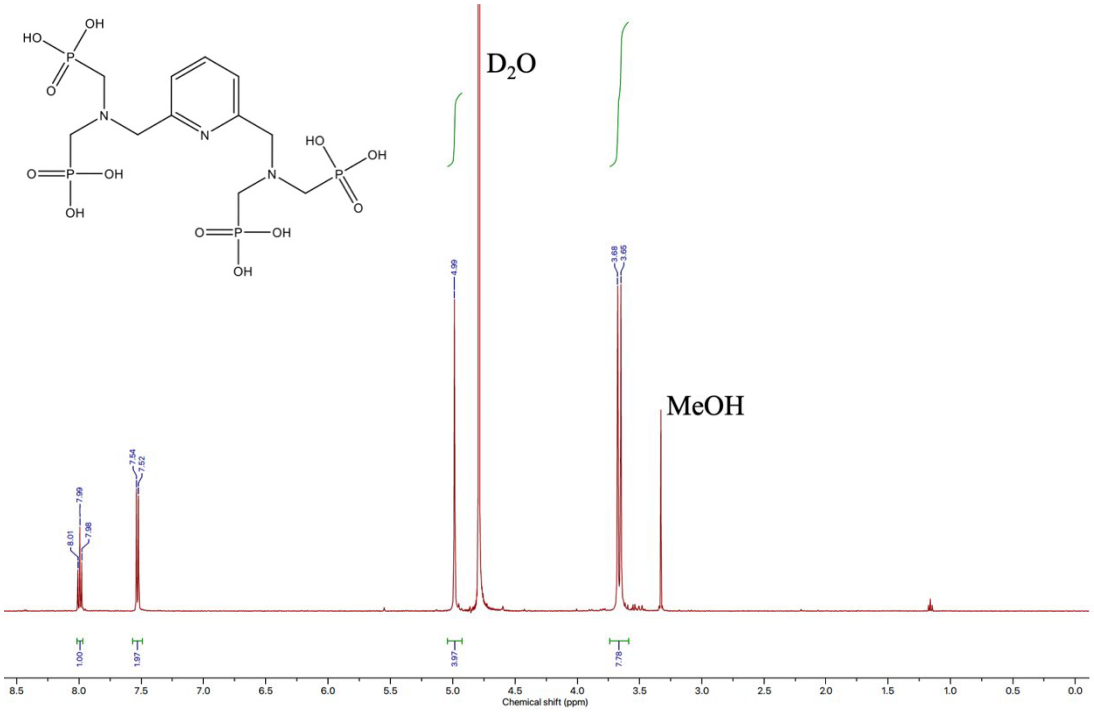

Figure A3.9. 500 MHz ^{1}H NMR spectrum of compound **AL238B** (in D_2O).

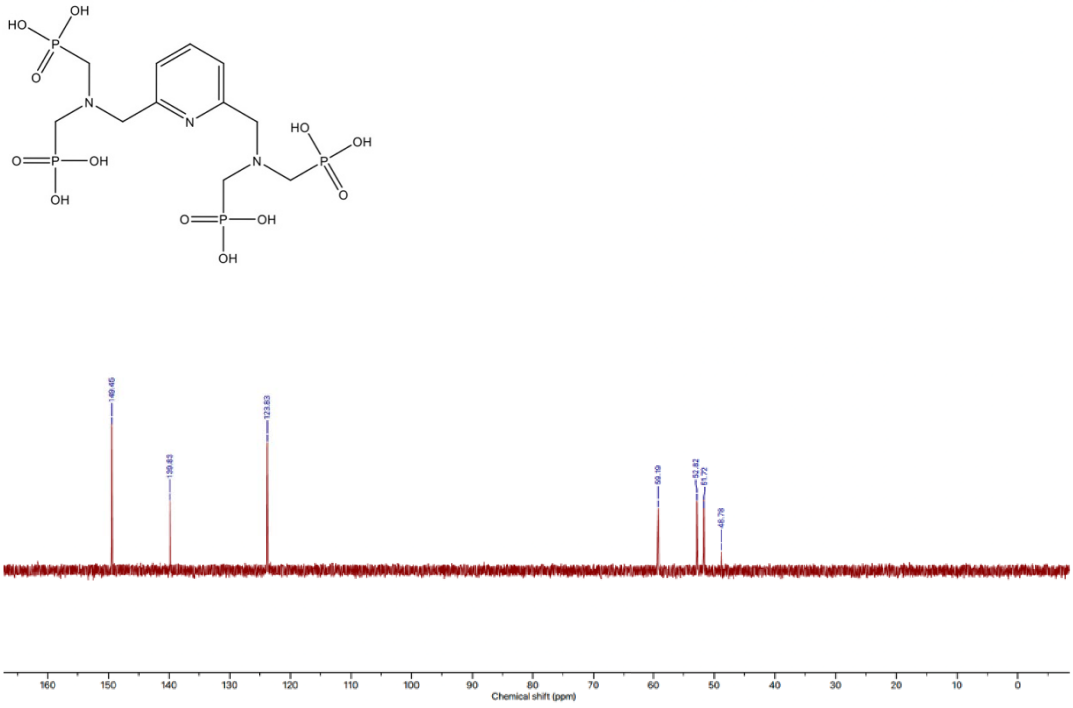

Figure A3.10. 126 MHz ^{13}C NMR spectrum of compound **AL238B** (in D_2O).

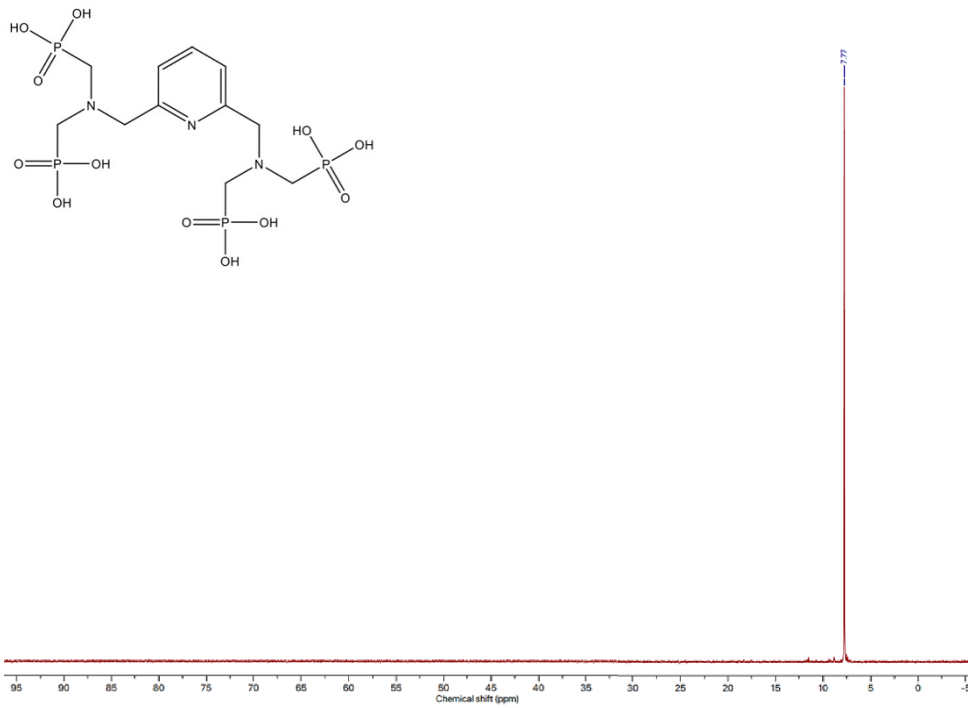

Figure A3.11. 202 MHz ^{31}P NMR spectrum of compound **AL238B** (in D_2O).

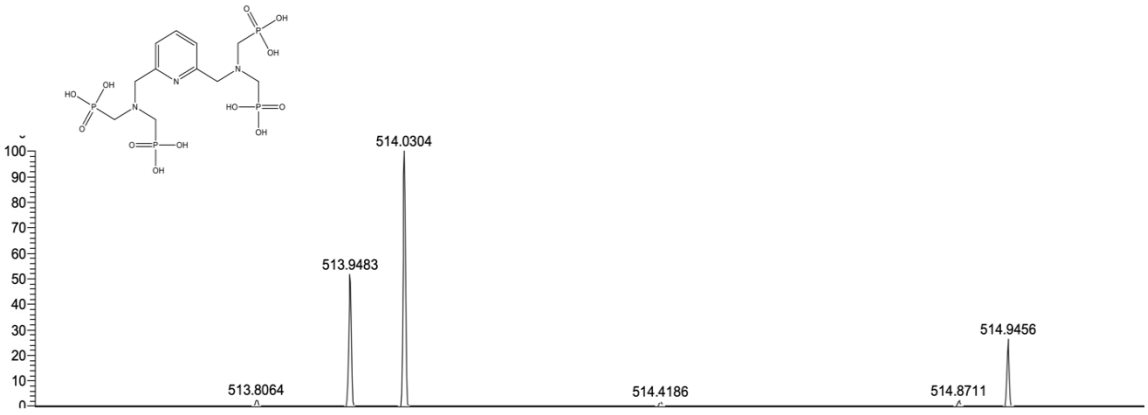

Figure A3.12. ESI-MS spectrum of compound **AL238B** (expected mass: 514.2).